DENSITY FLUCTUATION MEASUREMENTS

WITH LASER SCATTERING

by

Alain C. Côté

Keble College

This thesis is submitted for the degree
of Doctor of Philosophy
in the University of Oxford.

Department of Engineering Science

February 1989

A ma famille,

Abstract

Density fluctuation measurements with laser scattering

Alain C. Côté , Keble College
A thesis submitted for the degree of Doctor of Philosophy
in the University of Oxford, Hilary term 1989.

This thesis describes the development and application of a new, non-invasive, diagnostic based on far forward scattering(FFS) of electromagnetic radiation for investigating density fluctuations in fusion research plasmas.

The spatial distribution and phase of the oscillations induced on the profile of a Gaussian laser beam transmitted through a disturbed refractive medium can be predicted in terms of the characteristics of the disturbance, which can in turn be deduced from them. The theory of these interactions is presented with various models of perturbations to account for differing experimental conditions including one developed by the author which takes into account the effect of broadening in the K spectrum of the fluctuations.

Two sets of experiments are discussed in this thesis, both using a FFS apparatus based around a CO_2 laser and an array of 12 photoconductive detectors. The first successfully tested the prediction of FFS theory under controlled conditions using a transducer to generate ultrasonic waves in air, and an air jet to produce turbulence. Numerical reconstruction of the scattering structure was achieved under these ideal conditions.

In the second set of experiments, FFS was performed on plasma in the small tokamak TOSCA. Results are presented for density fluctuations with wavenumbers around 2 cm^{-1}, a bandwidth of several kHz and a relative fluctuation level of 6%. This level is roughly independent of the variation in the mean density and is close to the mixing length level, indicating strong turbulence. The fluctuations are found to be mainly poloidal and follow a ν^{-2} power law. The average phase velocities are around 4.5 km/sec and are slightly larger than the electron diamagnetic drift velocity. The waves are tentatively identified with the electron drift mode. Coherent signals due to long wavelength MHD modes are detected. Results from a Langmuir probe corroborate most of these data.

ACKNOWLEDGEMENTS

I am deeply indebted to both my supervisors Dr. D.E. Evans(Culham) and Dr. N.St.J. Braithwaite (Oxford) for their guidance and collaboration throughout the course of this work.

I am grateful to Dr. D.C. Robinson for allowing me to complete my measurements on TOSCA by extending its operating life and to Dr. H.A.B. Bodin and Dr. N.J. Peacock for support in the production of this thesis. I would also like to thank the following for helpful discussions: Drs. B. Alper, W. Arter, E.J. Doyle, A.H. Howling, A.W. Morris, Y. Sonoda and H.Y.W. Tsui. I could not have done the experimental work without the help of J. Bosley, P. Doyle, J. Dunsmore, K. Goodenough, R. Harris, J. Hill, A.H. Jones, G. Lee, J. Lynch, P. Marks, W.A. Morris, R. Peacock, J. Ryley, D.L. Trotman and P.D. Wilcock. Special thanks must also go to Y. Austin, N. Clarke, E.R.M. Lea, S. Puppin, C. Sborchia, M.J. Walsh and F. Watkins for helping me in the preparation of this thesis.

I must thank the Culham Laboratory for the use of their experimental facilities, and financial support for the last year. Finally, thanks should also go to *Le Conseil de Recherche en Science Naturelle et Génie du Canada* for providing me with financial support at the beginning of this research and *Les fonds FCAR* for contributing towards payment of my University fees.

My time in Oxford would not have been so enjoyable without many new friends (Canadian, English, French, Greek, Italian, Irish, Japanese, Scottish, Welsh ...). I thank you all.

Contents

List of Tables

List of Figures

List of symbols

a_l	Tokamak limiter radius
a	Amplitude ratio for FFS two wave model
$A_{\pm}$	$\equiv u \pm v/2$
B_ϕ/B_θ	magnetic field in the toroidal/poloidal direction
C_s	sound speed in air (330 m/sec)
D	normalised damping factor
$D_\perp$	perpendicular diffusion coefficient
f	focal length of lens
$\mathcal{G}_{xx}(\nu)$	Auto-power spectra
$\mathcal{G}_{xy}(\nu)$	Cross-power spectra
$I(u)$	laser beam intensity profile
I_{dc}	time–independent intensity component
I_{ac}	time–dependent intensity component
$I_{ac,e}$	envelope of I_{ac}
${I^2}_{ac}(\nu)$	spectral density associated with I_{ac}
$[I_{ac}(t)]_u$	time–dependent intensity measured at slit position u
$[{I^2}_{ac}(\nu)]_u$	spectral power density associated with $[I_{ac}(t)]_u$
$[I_{ac,e}(u)]_\nu$	envelope of fluctuating beam profile for frequency ν
j	$\sqrt{-1}$
k_l	wavenumber of light beam
K	wavevector of fluctuation
L	interaction length
L_{n_e}	density gradient scale length $L_{n_e} \equiv \left(\frac{1}{n_e}\frac{dn_e}{dr}\right)^{-1}$

n_e	electron density (m^{-3})
n_{eo}	spatial profile peak electron density (m^{-3})
$\tilde{n}_e$	electron density fluctuation (m^{-3})
P_o	power of incident laser beam at its centre
q	Tokamak safety factor
Q	$\equiv K^2L/k_l$, volume effect parameter
r	radius
R	major radius
r_e	classical electron radius
R_1	intensity ratio of the through to the peak of I_{ac}
R_2	intensity ratio of the two peaks of I_{ac}
S_o	slope of phase profile evaluated at $u = 0$.
$S_\pm$	slope of phase profile evaluated at $u \rightarrow \pm\infty$
S_∞	$\equiv (S_+ + S_-)/2$; average slope of phase profile evaluated at $u \rightarrow \pm\infty$
t	time
T_e/T_i	electron/ion temperature
T_{eo}	peak T_e radial profile
u	$\equiv x_i/W_i$,transverse position normalised to waist at detector
u_{pk}	peak position in intensity profile
v	$\equiv KW_o$; wavenumber normalised to the waist
v_{de}	electron drift velocity
v_p	phase velocity
w	Gaussian beam width parameter,defined at e^{-1} point in intensity
W	Gaussian beam width parameter,defined at e^{-1} point in intensity
W_o/W_i	Gaussian beam width parameter on the phase object/image side
x	transverse position relative to laser beam axis at detector plane
z	axial position relative to beam waist W_o
z_r	$\equiv k_l W_0{}^2$, Raleigh zone corresponding to object focal plane

List of Greek symbols

$\Delta\phi$	phase shift; for plasma induced phase shift ($\Delta\phi = r_e \lambda L \tilde{n}_e$)
ΔS_∞	$\equiv (S_+ - S_-)/2$; difference in slope of phase profile at $u \rightarrow \pm\infty$
Δv	$\equiv \Delta K W_o$; Normalised spectral width
ϵ	$\equiv r/R$, inverse aspect ratio
ζ	$\equiv z/z_r$,axial position normalised to Rayleigh zone
λ	laser wavelength
Λ	fluctuation wavelength
ν	spatial or temporal frequency
ν_{ei}	electron-ion collision rate
ρ_s	gyroradius (v_{te}/Ω_{ci})
τ_E	energy confinenement time
$\Phi(u)$	Phase profile in function of u
ω_{*e}	electron drift wave frequency
ω_{pe}	plasma electron frequency
Ω	fluctuation angular frequency
Ω_{ce}/Ω_{ci}	electron/ion cyclotronic frequency

Miscellaneous and Abbreviations

$\perp$	perpendicular to magnetic field
$\|\|$	parallel to magnetic field
ADC	Analog to Digital Converter
DFT	Discrete Fourier Transform
FFS	Far Forward Scattering
FFT	Fast Fourier Transform
SNR	Signal to Noise Ratio

Chapter 1

Introduction

There is considerable interest in the study of high temperature plasmas. Most of this interest is driven by the goal of achieving controlled thermonuclear fusion which involves the release of net nuclear energy from the fusion of light nuclei. To achieve fusion requires that the plasma temperature be greater than 10 keV and that the product of the plasma density and energy containment time($n\tau_E$) be greater than 1.0×10^{20}sec m^{-3}(Lawson,1957). One of the most promising approaches is the tokamak which uses a magnetic field to confine a hot plasma in a toroid. Tokamak plasmas exhibit anomalously high fluxes of energy and particles across the magnetic field in comparison to those expected from "neo-classical"[1] coulomb collisions of the charged plasma particles(Furth, 1975). This enhanced transport of energy out of the plasma reduces the energy containment time and still remains unexplained. Naturally occurring micro-turbulence driven by plasma inhomogeneities($\nabla n, \nabla T, \nabla \eta$) may give rise to this anomalous transport(Liewer, 1985).

The study of these plasmas requires diagnostics which ideally should be non-invasive and non-perturbative so as to minimise effects upon the plasma. Among the many types of diagnostics systems available those provided by lasers form a

[1]classical theory with correction for toroidal effects

very powerful class. Some advantages of the laser as a diagnostic tool are the following: it is sufficiently bright and monochromatic to compete favorably with the self-emission of the plasma in its narrow band of emission, it is remote and does not perturb.

This dissertation is concerned with a laser scattering diagnostic designed to study the nature of the turbulence and its possible link with transport. The broad background to the method completes this introduction.

Light can produce various types of interaction with the plasma (Magyar, 1981): scattering, absorption, reflection, refraction and transmission. Laser light scattering(called Thomson scattering) is perhaps the most versatile. It permits spatially and temporally resolved measurements of electron temperature and density, ion temperature, magnetic field direction and electron density fluctuation spectra. Every charged particle in the plasma is capable of scattering light but since the cross section is inversely proportional to the square of the particle mass, the contribution from the ions is negligible compared with that from the electrons.

In order to determine the scattering regime under investigation it is useful to define the Salpeter parameter(Salpeter, 1960):

$$\alpha = \frac{1}{K\lambda_d} \tag{1.1}$$

where K is the wavenumber in the plasma and λ_d the Debye length($\sqrt{\epsilon_o T/nq^2}$). All the electromagnetic equations have been written in MKS units and elsewhere SI units have been used apart from the temperature which is defined in eV. When $\alpha \ll 1$, the motion of individual electrons is observed and incoherent scattering results from thermal fluctuations whereas if $\alpha \gg 1$ plasma waves and thermal ion fluctuations may be studied.

The magnitude of the scattered vector k_s is obtained by applying momentum conservation. Consider the situation shown in figure 1.1 with an incident photon(k_l) being scattered from an electron moving with wavevector K at an angle θ with the

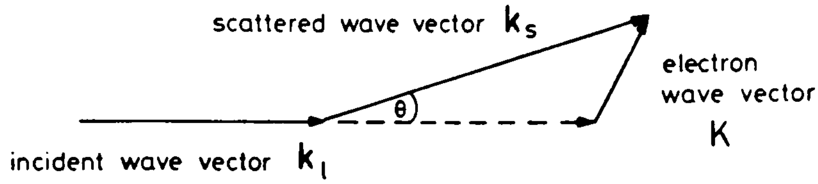

Figure 1.1: *Schematic of scattering arrangement.*

incident photon. Then by vectorial addition $\mathbf{K} = \mathbf{k}_s - \mathbf{k}_l$ which is

$$K^2 = k_l^2 + k_s^2 - 2k_l k_s \cos(\theta).$$

Since for non-relativistic electrons $|k_l| \simeq |k_s|$, then

$$\begin{aligned} K^2 &= 2k_l^2(1 - \cos\theta), \\ K &= 2k_l \sin(\theta/2) \end{aligned} \tag{1.2}$$

which is a Bragg angle relationship.

By combining 1.1 and 1.2, we obtain

$$\alpha = \frac{\lambda_l}{4\pi\lambda_d \sin(\theta/2)}. \tag{1.3}$$

This shows the two possible ways to look at coherent fluctuations($\alpha \gg 1$): we can either have a long wavelength radiation(λ_l) or a small scattering angle(θ). The conventional collective Thomson scattering arrangement [2] selects the wavenumber by the choice of the scattering angle. The scattered signal is heterodyned with a local oscillator, the latter being a portion of the incident beam which has not been through the plasma. Many experiments have been done using this technique for different wavelengths of radiation: microwave(TFR team, 1983; Mazzucato, 1978), 10 μm laser radiation(Slusher and Surko, 1978) and far infrared laser(FIR) (Semet *et al.*,1980; Brower *et al.*, 1985).

For a given wavelength of the laser, the study of long plasma wavelengths (Λ) will correspond to small scattering angles, but the scattering angle has to

[2] Also called finite angle scattering in this thesis.

be larger than the divergence of the beam so as to avoid any beating with the unscattered main beam. This introduces an upper limit at the plasma wavelength which corresponds to $\Lambda \approx 1$ cm for a CO_2 laser. Since tokamak plasma and especially the new generation of larger fusion device are subject to larger scale fluctuations an alternative to the above heterodyne technique is desirable.

Different techniques have been proposed and tested to look at long fluctuation wavelength(1–10 cm). The simplest one is to use a radiation with longer wavelength such as FIR laser or microwave(*op. cit.*). The main problem with this method is that a maximum detectable wavelength will still exist since as the wavelength is increased the beam is more refracted to the limit of being completely reflected at $\lambda_l = \lambda_c = 2\pi c/\omega_{pe}$. The second method proposed by Slusher and Surko(1980) uses correlation of the forward scattering from two intersecting laser beams in the plasma. Any correlation between the two signals will be due to fluctuations in the scattering volume common to the two beams. The technique has given good results but the necessity of four beams (two signals and two local oscillator) is a disadvantage. Jacobson *et al.*(1984) also used similar measurement by correlating neighbouring path of a multi-chord interferometer on ZT–40.

Another group of diagnostics circumvents the problem of beam divergence and stray light by using the unscattered beam as the local oscillator. Philipona (1987) developed a technique in which the local oscillator reference beam for the homodyne mixing is produced by diffraction from a thin tungsten wire which lies in the main probe beam near the scattering center. The diffraction wire produces a diffraction pattern covering the scattering plane and each diffraction order correspond to different K.

Weisen(1985) adapted the principle of phase contrast(Zernike,1935) to create an imaging system on TCA which behaves as an interferometer for K larger than a critical value. He measured wavenumber by correlating the intensity of neighbouring detectors in a way similar to Jacobson *et al.*(1984). Sharp (1983) measured large scale fluctuation density from a probing electromagnetic field using phase scintillation. If the observer plasma distance is well within the Fresnel distance of the irregularities($\ell \ll k_l b^2$), a direct relationship exists between the density and phase spectra.

The selected method which has been developed by Evans *et al.*(1982) allows measurement of long wavelength with only a single beam and has been named far forward scattering(FFS). Instead of being based on scattering theory, it considers the plasma in terms of its refractive index. Each wave in the plasma could then be represented by a phase grating which interacts with the main beam to produce different orders of diffraction. In practice, a gaussian beam profile is used which beats with the first diffracting order of the scattered light to produce the homodyne signal. This signal is sensitive to frequency, wavelength and location of the disturbance in the medium. Some test of FFS has been performed on plasma machines with excited waves and the results showed close agreement with the theory(von Hellermann and Holzhauer,1984; Brodeur *et al.*,1988; Sonoda *et al.*,1983). Experiments have been carried out on tokamak(Evans *et al.*,1983) and have revealed fluctuations probably arising from drift waves.

This thesis describes two sets of experiments. The first was designed to test the prediction of FFS theory under controlled conditions using a transducer to generate monochromatic ultrasonic waves in air, and an air jet to produce turbulence. In the second set of experiments, FFS was performed on the small tokamak TOSCA and observations were interpreted using FFS theory and were compared with results from other diagnostics.

This dissertation is organised in 7 chapters. The theory of FFS is developed in detail for the simplest case of a single phase wave in Chapter 2. A survey of FFS theory with different models is also presented, including one which takes into account the K broadening developed by the author.

A detailed description of the scattering apparatus based around an array of detectors with the relevant signal processing is presented in Chapter 3. Tests of the validity of FFS theory with ultrasonic waves and air-jet are described in Chapter 4. The practical limitations are also addressed and image reconstruction of the scattering medium is discussed.

Chapter 5 described the plasma machine(TOSCA) and some of its diagnostics. Relevant turbulence theory is also reviewed in the same chapter with special emphasis on drift wave. Chapter 6 sets out the main result of the plasma experiment including statistical analysis, dispersion relations, total fluctuation level and comparison with other diagnostics.

A summary of the experimental results and final discussion concerning their implication are presented in Chapter 7. The direction future measurements might take is also indicated.

Chapter 2

Theory of far forward scattering

2.1 Introduction

The aim of the chapter is to derive an analytical expression for the intensity of light scattered from plasma fluctuations. Different methods for analysing small angle scattering already exist and we will briefly discuss some of them before concentrating on our preferred fourier optic approach.

All approaches are based on electromagnetic scattering theory which has been reviewed in many articles (Evans and Katzenstein, 1969; Zhukovskii and Rtishchev, 1988) and textbooks (Sheffield, 1975). The scattered field is calculated by summing up the field generated by all the individual charged particles which are accelerated by the incoming electromagnetic wave. Since the plasma behaves as a weakly refractive medium towards the laser light, similar to the air with respect to acoustic disturbance, the theory of acousto-optics is applicable to our analysis. The most common approach is to solve the wave equation inside the medium by using the refractive index as a bulk dielectric property (Klein and Cook, 1967; Korpel, 1981). Born and Wolf (1980) have described in their book other methods of analysis such as the calculation of the scattered field from the volume polarisation of the medium.

Although all the previous methods are relevant, we adopt the scalar diffraction approach with its fourier optic extension. The advantage of using this theory is that the optical system can be considered entirely in terms of diffraction, refraction and reflection. A brief review of the scalar diffraction approach is presented in the next section. This is followed by a detailed calculation of the scattered field due to an ideal thin wave. In our context, waves can be produced in any medium (plasma, gas, crystal) where their effect only changes the refractive index. Extension of these calculations to more realistic situations such as scattering by a wave involving oblique incidence, finite width, damping, finite spread of wavenumber and to the case in which there are two waves will be carried out in the last part of the chapter. Each of these non-ideal conditions will be treated separately.

2.2 Scalar diffraction theory

The propagation of a beam of radiation can be described by the scalar diffraction theory. This amounts to ignoring coupling of the various field components through Maxwell's equations which is acceptable provided the following conditions are met (Goodman, 1968): the diffraction aperture must be large compared with the wavelength and the point of observation must not be too close to the aperture (*i.e.* not in the wave zone). The interaction of a dielectric material with radiation is described in terms of a refractive index.

The basic theory is that of Huygens principle which states that the light at a point P is due to the superposition of secondary waves that proceed from a surface situated between this point and the light source. Let radiation travel in the $+z$ direction and its amplitude distribution in any plane normal to the z axis be $U(x,y,z,t)$; U can be written in complex notation as

$$U(x,y,z,t) = \Re e\left\{U(x,y)e^{-j(\omega t - k_l z)}\right\}$$

Considering the optical geometry illustrated in figure 2.1, the complex amplitude

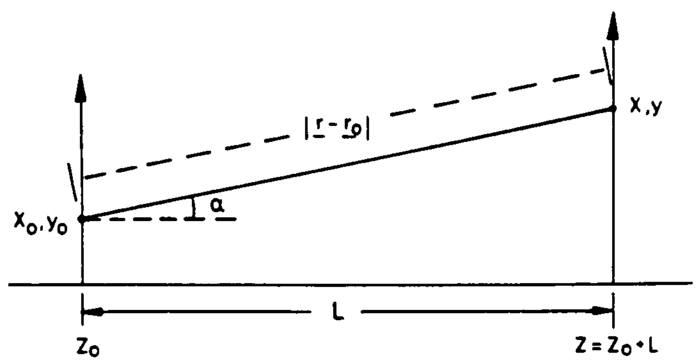

Figure 2.1: *Basic geometry for analysing diffraction.*

at the output plane $U(x_s, y_s)$,will be given in terms of the input wave amplitude $U_0(x_0, y_0)$ (Born and Wolfe, 1980) by integrating all contributions from points in the input plane:

$$U(x,y) = \frac{j}{\lambda}\iint_{\substack{input\\plane}} U_o(x_o,y_o)\frac{1+\cos(\alpha)}{2}\frac{e^{-jk_l|\mathbf{r}-\mathbf{r_0}|}}{|\mathbf{r}-\mathbf{r_0}|}dx_o dy_o. \tag{2.1}$$

Since laser beams are employed, a paraxial approximation may be used. This considers only small angles ($\alpha \ll 1$) and distances of propagation much larger than the transverse dimension, that is to replace $|\mathbf{r}-\mathbf{r_0}|$ by $z - z_0 \equiv L$ in the denominator of equation 2.1 . This latter approximation cannot be used in the exponential term of equation 2.1 because it could generate phase errors much greater than 2π radians. However, further simplification can be accomplished by approximating the quantity $|\mathbf{r}-\mathbf{r_0}|$ in the exponent by a truncation of its binomial expansion:

$$|\mathbf{r}-\mathbf{r_0}| \approx L\left\{1+\frac{(x-x_o)^2}{2L^2}+\frac{(y-y_o)^2}{2L^2}\right\} \text{ for } |x-x_o|,|y-y_o| \ll L.$$

This leads to the Fresnel-Huygens diffraction integral

$$U(x,y) = \frac{j}{L\lambda}\iint_{\substack{input\\plane}} U_o(x_o,y_o)\exp\left\{\frac{-jk_l}{2L}\left((x-x_o)^2+(y-y_o)^2\right)\right\}dx_o dy_o. \tag{2.2}$$

This last equation can be expressed in either of two equivalent forms.

1. First $U(x,y)$ may be regarded as a convolution of $U(x_0, y_0)$ with the Fresnel

Kernel h_z; that is (Goodman, 1968)

$$U(x,y) = h_z(x,y) * U_o(x_o, y_o) \tag{2.3}$$

where

$$h_z(x,y) = \frac{j}{\lambda z} e^{-jk_l z} \exp\left\{\frac{jk_l}{2z}(x^2+y^2)\right\}. \tag{2.4}$$

2. Alternatively the quadratic terms in the exponents of (2.2) may be expanded to yield

$$U(x,y) = h_z(x,y) \cdot \mathcal{F}\left\{U_o(x_o,y_o)\exp\left(\frac{jk_l}{2z}({x_o}^2+{y_o}^2)\right)\right\} \tag{2.5}$$

where $\mathcal{F}$ signifies a Fourier transform evaluated at spatial frequencies $\nu_x = x/\lambda z$ and $\nu_y = y/\lambda z$. So, the Fresnel-Huygens diffraction integral may be viewed in terms of a convolution or the Fourier transform of a product.

Diffraction pattern calculation can be further simplified if we adopt the Fraunhofer assumption

$$z \gg k_l(x_o^2 + y_o^2)/2.$$

The quadratic phase factor $\exp(jk_l({x^2}_0 + {y^2}_0)/2z)$ is then unity over the entire aperture, and the observed field distribution is given by the Fourier transform of the aperture distribution

$$U(x_s, y_s) = h_z(x,y) \cdot \mathcal{F}\{U_o(x_o,y_o)\}.$$

This simplification in the field calculation is desirable but the Fraunhofer condition is too severe for our own practical application ($z \gg 120$m for $x_1 = 1$cm and for CO_2 laser). Fortunately, the introduction of a lens or a converging mirror also yield a pure Fourier transform between the two focal planes (Gaskill, 1978).

To represent the interaction between a lens or any dielectric objects and the optical beam, we make use of the transmission function. These functions are defined as (Goodman, 1968)

$$t(x,y) = \frac{U(x,y)}{U_0(x,y)} \tag{2.6}$$

where $U(x,y)$ is the field with the object in the system and $U_0(x,y)$ is the field at the same position but without it. The effect of spherical mirrors or lens is to introduce a phase shift of the field which depends on its position with respect to the mirror axis. So, for example, the transmission function of spherical mirror with the approximations of paraxial rays is then:

$$t_l(x,y) = \exp\{jk_l(\Delta_0 - (x^2+y^2)/2f)\} \tag{2.7}$$

where f is the focal length of the mirror and Δ_0 its width.

2.3 Transmission function of a phase wave

As stated earlier, the interaction between the medium and the radiation is expressed by the dielectric coefficient (ε). The latter for a cold plasma is given by the Appleton-Hartree equation(Clemmow and Dougherty, 1969) when the frequency of the electromagnetic wave (ω_l) is above the plasma frequency ($\omega_{pe} = \sqrt{ne^2/m\varepsilon_0}$). For $\omega_l \gg \omega_{pe} + \Omega_{ce}$, where Ω_{ce} is the electron cyclotron frequency, the refractive index ($\mu_p = \sqrt{\varepsilon}$) is given by

$$\mu_p = \sqrt{1 - \frac{\omega_{pe}^2}{\omega_l^2}} \approx 1 - \frac{\omega_{pe}^2}{2\omega_l^2}. \tag{2.8}$$

For a neutral gas, the refractive index is given by the Dale-Gladstone equation(Born and Wolfe, 1980)

$$\mu = 1 + C\rho \tag{2.9}$$

where C is a constant of the medium and ρ the mass density of the gas. As pointed out by Doyle and Evans(1985,b), the refractive index for the plasma depends on the density of the material in the same general form as for others dielectric materials such as air, crystal ... This shows that the scattering of radiation by plasma is similar to the acousto-optic case.

The total phase shift imposed on the laser beam in traversing the plasma is then

$$\phi = \int_0^L k_l(1-\mu_p)dz \simeq k_l L(1-\mu_p)$$

where L is the length over which the plasma and laser interact. By substituting the plasma refractive index of equation 2.8 into the above equation, we obtain

$$\phi = r_e \lambda L n_e \tag{2.10}$$

where r_e is the classical electron radius(2.82×10^{-15} m) and n_e the electron density.

Let us consider a monochromatic plasma oscillation of wavelength K and frequency Ω,varying only in the x direction normal to the light axis of propagation.To distinguish between plasma and light wavenumbers; we will employ K and k_l respectively. This wave will produce a phase modulation on the radiation given by:

$$\Delta\phi \sin(\Omega t - K x_p)$$

where the phase shift $\Delta\phi = r_e \lambda L \tilde{n}_e$.

The total transmission function due to the main plasma and the disturbance is given by

$$t_p(x_p, y_p) = e^{j\phi_o} \exp\left\{\Delta\phi \sin(\Omega t - K x_p)\right\}. \tag{2.11}$$

The time independent phase shift(ϕ_o) is caused by the bulk of the plasma and can be measured with an interferometer. For a small fluctuating phase shift ($\Delta\phi \ll 1$), a binomial expansion of the time dependent term of equation 2.11 yields

$$t_p(x_p, y_p) \simeq 1 + \frac{1}{2}\Delta\phi \left[e^{j(\Omega t - K x_p)} - e^{-j(\Omega t - K x_p)}\right] + \ldots \tag{2.12}$$

The truncation of the expansion up to the first order constitutes the familiar Born approximation (Born and Wolf, 1980) which neglects multiple scattering by the wave. The previous assumption of a moving phase grating implies that Raman-Nath rather than Bragg diffraction will occur. In the Raman-Nath regime, different orders of diffractions occur whereas in Bragg regime only one is produced at the Bragg angle. The parameter Q, which has been defined by Klein and Cook (1967), delimits the two regimes:

$$Q = \frac{K^2 L}{k_l}. \tag{2.13}$$

If $Q \ll 1$ then Ramath Nath scattering is obtained whereas for $Q \gg 1$ Bragg scattering dominates. The effect of finite length of interaction will be considered later (Section 2.8).

2.4 Intensity distribution for one wave

We now consider a general arrangement illustrated in figure 2.2 where D_1 and D_2 are arbitrary distances measured from the lens to the phase wave and detector plane respectively. The lens is included because of its Fourier transform properties for an observation plane which is not situated at infinity and also because it has the additional advantage of focusing the light. The free propagation case leading to the Fraunhofer approximation was treated by Sonoda *et al.*(1983) but it is not well suited for near infrared radiation since the Fraunhofer distance is too long (100m!) for our application.

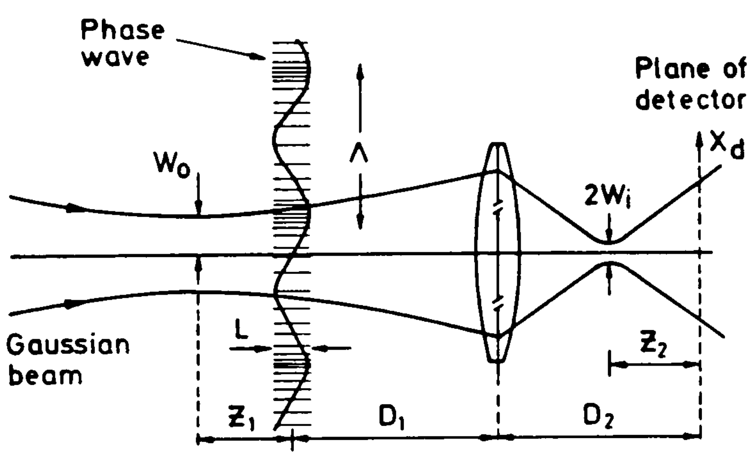

Figure 2.2: *Configuration of phase wave, lens and detector plane under analysis.*

A Gaussian beam of radiation proceeds from left to right and its waist (W_o) is at a distance $(D_1 + Z_1)$ from a lens of focal length f. It encounters a monochromatic phase wave with width L and wavelength Λ at a distance Z_1 to the right of the beam waist. We wish to calculate the field due to the disturbance in a detector plane (x_d) situated at a distance D_2 in front of the lens.

With the help of the mathematics assembled in the previous section, the field distribution in the detector plane (x_d) can be calculated by successive application of the Fresnel diffraction integral. Using the convolution representation of the integral (equation 2.3), this leads to

$$U(x_i, y_i) = ((U_p * h_{D_1}) \cdot t_l) * h_{D_2} \tag{2.14}$$

where the amplitude distribution U_p is a Gaussian beam modified by the plasma wave, t_l the transmission function of the lens and h_D the Fresnel kernel. Calling U_g the Gaussian beam amplitude distribution just before the wave and t_p the transmission function of the plasma (equation 2.12), U_p could be expressed as

$$U_p = U_g \cdot t_p$$

The Gaussian amplitude distribution which is the main mode of radiation for most lasers could be represented by (Siegman,1971)

$$U(x_p, y_p) = \left(\frac{P_o}{\pi w_p^2}\right)^{1/2} \exp\{-j(k_l z - \psi(z))\} \exp\left\{\frac{k}{2}\frac{(x_p^2 + y_p^2)}{q_p}\right\}. \tag{2.15}$$

Here q_p is the complex radius of curvature($z + jz_R$) and w_p is the beam width parameter at z defined as the half-width at $1/e$ height of the intensity profile. The term P_0 is the total power of the beam and the parameter $z_R = k_l W_o^2$, the Rayleigh zone, is defined as the distance from the beam waist to the position where the beam radius has grown to $\sqrt{2}\ W_o$. A brief account of Gaussian optics is given in Appendix–A.

The electric and magnetic field of the light cannot be measured instantaneously because of its too high frequency. The quantity which is measured is the intensity, I, defined as the time average of the energy which crosses a unit area containing the electric and magnetic vector per unit of time(Born and Wolfe, 1980)

$$I = \frac{1}{2}| < \mathbf{E} \times \mathbf{H} > |.$$

Fortunately, the intensity may be calculated with the complex scalar function U (Goodman,1968) using

$$I = U \cdot U^{*}. \tag{2.16}$$

After combining the previous equation and defining the following dimensionless parameters

$$\begin{aligned} u_x &= \frac{x_d}{w_i} & u_y &= \frac{y_d}{w_i} & \zeta &= \frac{z_1}{z_{r1}} + k_l w_p \frac{(D_1 - D)}{D_1^2} \\ v &= \frac{K w_p}{\sqrt{1+\zeta^2}} & \theta_\pm &= v\zeta_1 A_\pm & D &= \left(\frac{1}{D_1} + \frac{1}{D_2} - \frac{1}{f}\right)^{-1}. \end{aligned}$$

where w_i and w_p are the waist at the image(detector) and phase wave plane respectively, we obtain the intensity profile in the detection plane

$$I(u_x, u_y, t) = \frac{P_o}{\pi w_i^2} e^{-u_x^2 - u_y^2} + \frac{P_o}{\pi w_i^2} \frac{(\tilde{n}_e r_e \lambda L)}{2} e^{-u_x^2} e^{-\frac{v^2}{2}} \cdot$$

$$\left\{ \sin(\Omega t) \underbrace{\{e^{uv}\cos(\theta_-) - e^{-uv}\cos(\theta_+)\}}_{h} + \cos(\Omega t) \underbrace{\{e^{-uv}\sin(\theta_+) - e^{uv}\sin(\theta_-)\}}_{g} \right\} \tag{2.17}$$

$$I(u_x) = I_{dc} + I_{ac} \tag{2.18}$$

The first terms represents the unperturbed Gaussian beam, while the second one, proportional to $\Delta\phi$, consists of two Gaussians centered at $u \pm v/2$ and oscillating at the frequency Ω of the wave but out of phase with each other. The latter phase difference is a function of the plasma wavelength (v) and its position with respect to the back focal plane(ζ). The second term could be identified as a Schlieren phenomenon because of its antisymmetric and oscillatory character as well as its dependence on the first power of $\Delta\phi$ (Evans, von Hellermann and Holzhauer; 1982). It should be noted that all terms in $\Delta\phi^2$ have been neglected in this development. Inclusion of these terms in the expansion of t_p(equation 2.12) and in the calculation of I_{ac} (equation 2.17) would lead to an intensity distribution similar to the one obtained in Evans *et al.*(1982). The difference between equation 2.17 and their results lies in the addition of two terms directly proportional to $\Delta\phi^2$. These additions have been identified as (i) the signal in the heterodyne technique and (ii) the shadowgraph technique.

If the lens is absent, James and Yu(1985) showed that the expression of I_{ac} is of the same form as above with a new definition of ζ:

$$\zeta = \frac{z_1}{z_r} + \frac{k_l {w_1}^2}{R}$$

where $R = (D_1 + D_2)$, is the distance between the wave and the detector. The near field observation of the laser beam can then be obtained by taking the limit $\zeta \gg 1$. This reduces I_{ac} in equation 2.17 to a form similar to the phase scintillation result of Sharp(1983) obtained without the diffraction theory. The other limit ($\zeta \ll 1$) which corresponds to the far field, yields the Fraunhofer diffraction theory of Sonoda(1983).

With the lens present all values of ζ are accessible by varying the geometry and the focal length of the lens. This demonstrates that the theory of far forward scattering (FFS) as developed by Evans *et al.*(1982) is more general and encompasses all the other cases. In the remaining of this thesis, we have chosen the simpler configuration in which the back focal plane of the lens correspond to the waist and detector plane($D_2 = f, z_2 = 0$). This implies that the dimensionless parameters simplifies to

$$\zeta = \frac{z_1}{z_r} \qquad \text{and} \qquad v = KW_o.$$

The more general equation is nevertheless still useful in assessing the effects of position errors on the profile shape.

2.5 Phase and intensity profile

The I_{ac} term in equation 2.17 contains $\Delta\phi$ which includes the information about the level of fluctuation. Because of its oscillatory character, I_{ac} could be easily obtained by filtering in temporal frequency the total intensity. Estimation of $\Delta\phi$ would then require curve fitting of I_{ac}. Since I_{ac} is time dependent, this task turns out to be quite difficult.

An alternative method is to consider a time independent expression of I_{ac} which can be constructed by first rewriting I_{ac} as:

$$I_{ac}(u_x, t) = I_{ac,e}(u_x)\sin(\Omega t - \Phi(u_x)). \tag{2.19}$$

The intensity envelope ($I_{ac,e}$) and the relative temporal phase across the profile (Φ) are the expressions desired and are given by:

$$I_{ac,e}(u_x) = I_{dc}\Delta\phi\sqrt{2}e^{-\frac{v^2}{2}}\left[\cosh(2uv) - \cos\zeta v^2\right]^{1/2} \tag{2.20}$$

$$\Phi(u_x) = \arctan\left\{\frac{e^{uv}\cos(\zeta v A_-) - e^{-uv}\cos(\zeta v A_+)}{e^{-uv}\sin(\zeta v A_+) - e^{uv}\sin(\zeta v A_-)}\right\} \tag{2.21}$$

These ideal profiles depend on the intensity, wavelength and position with respect to the waist of the wave through the three dimensionless parameters: $\Delta\phi, v$ and ζ. Their dependence on u and v for $\zeta = 1$ is shown in figure 2.3 on a contour plot for constant intensity and phase. Both profiles are symmetric with respect to the center of the gaussian beam ($u = 0$) as can be seen in figure 2.4 for the specific case of $\zeta = 1$ and $v = 1$.

For one particular ζ the decrease in the signal with v is due to the increase of the angle between the zeroth and the first order of diffraction. This impedes their overlapping and therefore their homodyning . For small v, the signal decreases also because of the decrease of the area from which the light is scattered. This is equivalent to the concept of directivity of an antenna in communication theory where a decrease in the antenna area decreases the directivity (Doyle, 1982).

At this stage some dimensionless parameters will be defined to facilitate the future comparison between different models of fluctuations. Figure 2.4 illustrates the definition of the average peak position (u_{pk}) and trough (u_0) as well as the ratio of the highest peak to the lowest peak (R_2) which for the ideal case is unity. The ratio of the trough I_0 to the peak intensity (I_{pk}) is defined as R_1 and is plotted versus v in figure 2.5(a) for 3 different ζ. The ratio R_1 reaches a maximum around

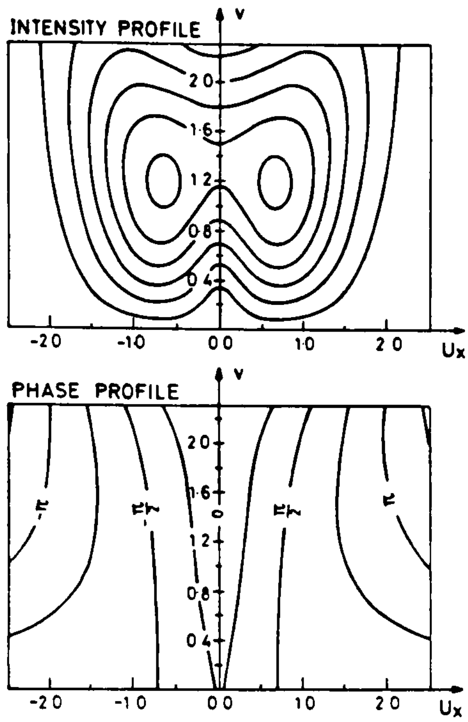

Figure 2.3: *Intensity and phase profile for ζ=1.*

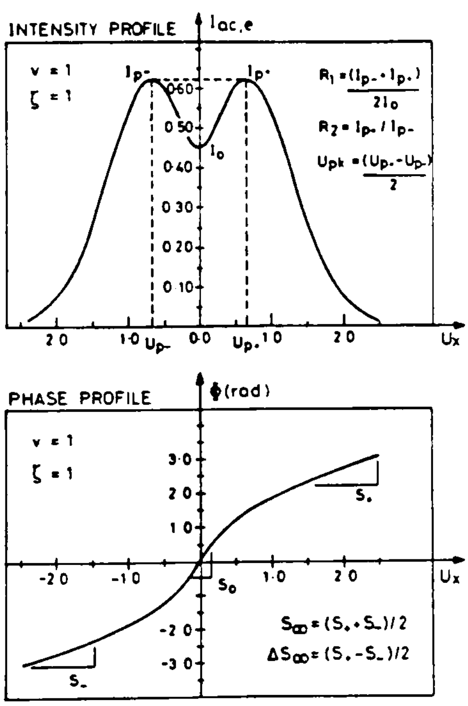

Figure 2.4: *Section of fig. 2.3 profiles at v=1 with definitions of shape parameters.*

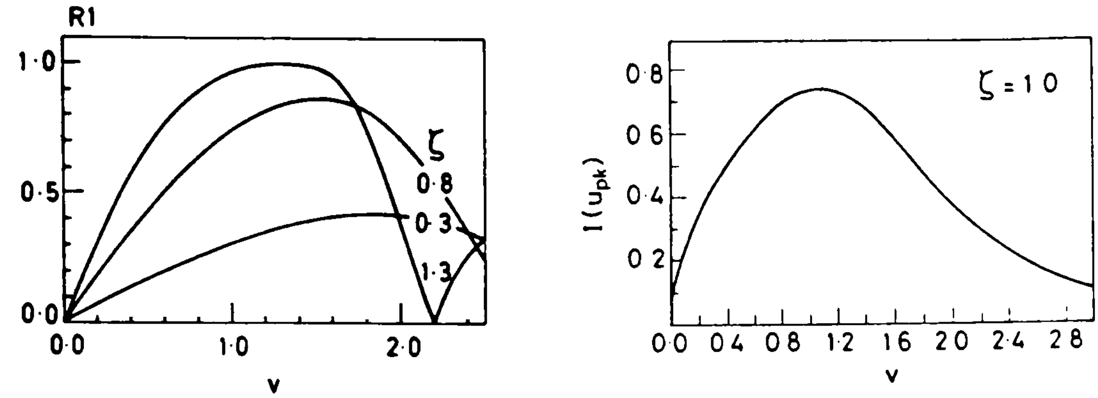

Figure 2.5: *Plot of (a)ratio R_1 and (b)peak intensity($I(u_{pk})$) in function of v.*

($v \sim 1$) in a fashion similar to $I(u_{pk})$ which is displayed in figure 2.5(b). For small v ($v < 0.8$), the slope of the phase profile at the position of the trough in intensity (S_0) is inversely proportional to the ratio R_1, this allows an easy cross check of the two profiles obtained. The expression for S_0 is given by:

$$S_0 = \zeta v + v \cot\left(\frac{\zeta v^2}{2}\right) \tag{2.22}$$

As well as S_0, we characterise the phase profile by two other parameters (S_∞ and ΔS_∞) related to the slope at the edge of the beam ($u \gg 1$). They are defined by

$$S_\infty = (S_+ + S_-)/2 \qquad \text{and} \qquad \Delta S_\infty = (S_+ - S_-)/2$$

where $S_+ = \left.\frac{\partial\Phi}{\partial u}\right|_{u \gg 1}$ and $S_- = \left.\frac{\partial\Phi}{\partial u}\right|_{u \ll -1}$. For the present case, this yields:

$$S_\infty = \zeta v \qquad \text{and} \qquad \Delta S_\infty = 0.$$

If the optical geometry is arranged is such a way that the fluctuation to be investigated can only occur either in the range $\zeta > 0$ or in the range $\zeta < 0$, the slope of the phase Φ unambiguously determines the sign of v and hence the direction of propagation.

2.6 Scattering by two waves

The model as developed so far always generates symmetric profiles whereas early measurements in plasmas exhibited asymmetric peaks and these have proved to be as common as symmetric ones. Modifications of the model were attempted to try to find a better description of the wave configuration actually encountered in the plasma that would give rise to asymmetric profiles. This section and the three following will describe more realistic situations which alter the profile.

The first model to cater for these anomalies was the two plasma waves case by Evans and Doyle(1983) and we will follow their development. They applied the method of FFS to measurement in Tokamaks and had to consider a probing electromagnetic wave crossing poloidal plasma waves twice (because of cylindrical geometry) once on the way in and once on the way out.

The optical arrangement specific for this case is illustrated in figure 2.6. The laser radiation is scattered by the wave in positions 1 and 2 which are situated respectively at Z_1, and Z_2 from the beam waist. The amplitude of the wave in 2 is "a" times larger than in 1. The two waves oscillate at the same frequency(Ω) but they are out of phase by θ. Their wave vectors are equal in amplitude but opposite in direction. With this information, the transmission function of the two waves can be written as

$$t_{p_1}(x,t) = \exp\{-j\ \Delta\phi_1 \sin(\omega t - K_1 x)\} \qquad = \exp\{-j\ \Delta\phi \sin(\omega t - Kx)\}\,,$$
$$t_{p_2}(x,t) = \exp\{-j\ \Delta\phi_2 \sin(\omega t + K_2 x + \theta)\} = \exp\{-ja\ \Delta\phi \sin(\omega t + Kx + \theta)\}\,.$$

In this configuration $D_2 = f$ and the detector is situated at the focal plane of the lens. The scattering regime is assumed to be Raman-Nath which corresponds to a small interaction length. Scattered radiation is presumed to arise only from an interaction with one of either wave, but not both simultaneously. A second diffraction due to the other wave would give an amplitude proportional to $\Delta\phi^2$ which is negligible.

Following the last assumption, we can write the scattered intensity distribution as the sum of the two independent (I_{ac}) terms as defined in equation 2.17 such that

$$I_{ac}(u_x, u_y, t) = \overbrace{\frac{P_o}{\pi W_i}\frac{(\bar{n}_e r_e \lambda L)}{2} e^{-u^2} e^{-\frac{v^2}{2}}}^{C}$$
$$\cdot \left\{ \cos(\Omega t) \underbrace{(S_- e^{uv} - S_+ e^{-uv})}_{g} + \sin(\Omega t) \underbrace{(C_- e^{uv} - C_+ e^{-uv})}_{h} \right\} \qquad (2.23)$$

where

$$\zeta_1 = \left(\frac{z_1}{z_r}\right) \qquad C_\pm = \cos(v\zeta_1 A_\pm) - a\cos(v\zeta_2 A_\pm + \theta)$$
$$\zeta_2 = \left(\frac{z_2}{z_r}\right) \qquad S_\pm = \sin(v\zeta_1 A_\pm) - a\sin(v\zeta_2 A_\pm + \theta)$$

Using another trigonometric relation, the last expression could be expressed as before by:

$$I_{ac,e} = C\sqrt{g^2 + h^2} \qquad \Phi = \arctan\left(\frac{h}{g}\right). \qquad (2.24)$$

Figure 2.7 shows an example of intensity and phase profile exhibiting the 3 humps characteristics of scattering by two waves.

2.7 Damping Wave

The introduction of damped wave theory into the theoretical analysis of FFS was first carried out by Yu *et al.*(1988). Their scattering geometry is identical to the thin wave case (figure 2.2), but the transmission function of the damped wave is taken to be

$$t_p(x,t) = \exp\left\{ j\ \Delta\phi_0\ e^{-\alpha x}\ \sin(\Omega t - Kx)\right\}. \qquad (2.25)$$

Here $\Delta\phi_0$ and α are respectively the phase shift amplitude ($r_e\lambda_0 L\bar{n}_e$)and damping rate of the wave on the beam axis.

After expanding t_p for small $\Delta\phi$ in equation 2.25 and combining it with equation

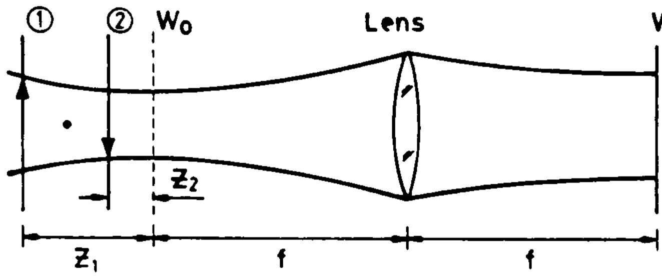

Figure 2.6: *Configuration for scattering by two waves.*

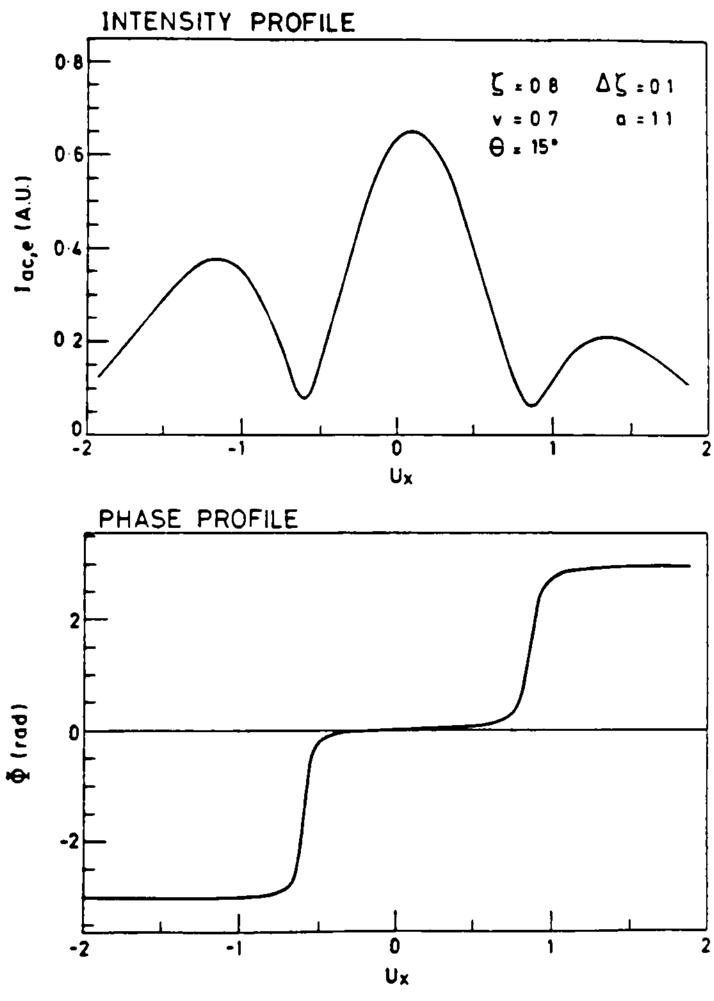

Figure 2.7: *Intensity and phase profile for scattering by two waves.*

2.14, the time dependant intensity profiles at the plane of detection is given by:

$$I_{ac}(u_x,u_y,t) = \overbrace{\frac{P_o}{\pi\omega_s{}^2}(\tilde{n}_e r_e \lambda L)\exp\left\{-(u_x^2+u_y^2)+\frac{D^2-v^2}{2}-\zeta D u_x\right\}}^{C} \tag{2.26}$$

$$\left\{\sin(\Omega t)\underbrace{\{e^{B}\cos(\Theta_-)-e^{-B}\cos(\Theta_+)\}}_{h}+\cos(\Omega t)\underbrace{\{e^{-B}\sin(\Theta_+)-e^{B}\sin(\Theta_-)\}}_{g}\right\}$$

where
$$\begin{aligned} B &= u_x v + \zeta D v, \\ \Theta_\pm &= v\zeta_1\left(u_x \pm \frac{v}{2}\right) + D(v \pm u_x) \pm \frac{\zeta D^2}{2}. \end{aligned}$$

In the last expression, the only new normalised parameter (D) is defined as : $D \equiv \alpha W_o/\sqrt{1+\zeta^2}$ which represents the damping of the wave. The intensity and phase profile will be given by equation 2.24.

It can be demonstrated that if the wave damping is absent or the beam radius at the plasma wave is small enough, D will tend towards zero and the equation 2.26 will reduce to the ideal case of section 2.4.

The profiles obtained from equation 2.26 are shown in figure 2.8 for $\zeta = 1$, $v = .5$ and for four values of D. In the absence of damping, the intensity and phase profile are symmetric about the beam axis ($u_x = 0$) while for ($D \neq 0$) asymmetry appears. The ratio of the smaller to the larger peak value (R_2) is dependant on D for a wide range of v as shown on figure 2.9. The ratio R_1 is only sensitive to D for $v > 1$. The peak position (u_p) is weakly dependent on the damping factor D and as the same functional dependency on v as for the single wave case.

The slope of the phase profile in the wings of the Gaussian profile far away from the center of the beam ($|u| \gg 1$) can be approximated to

$$S_+ = \left.\frac{\partial\Phi}{\partial u}\right|_{u\gg 1} = \zeta v + D \qquad \text{and} \qquad S_- = \left.\frac{\partial\Phi}{\partial u}\right|_{u\ll -1} = \zeta v - D.$$

The average of the slope (S_∞) will give ζv while their difference (ΔS_∞) will yield

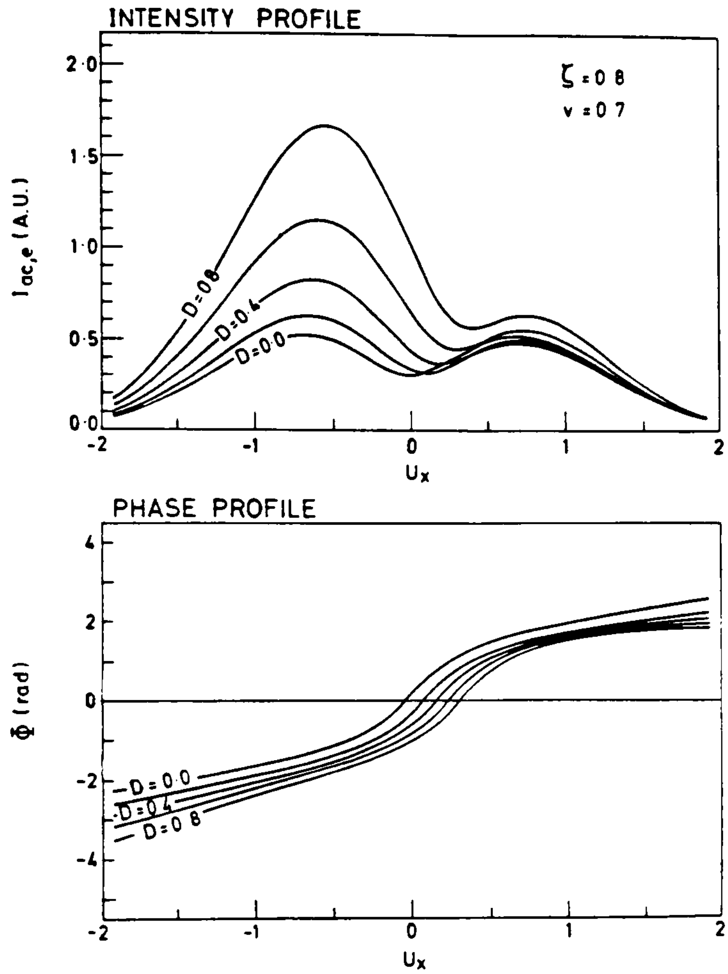

Figure 2.8: *Intensity and phase profile from a damped wave.*

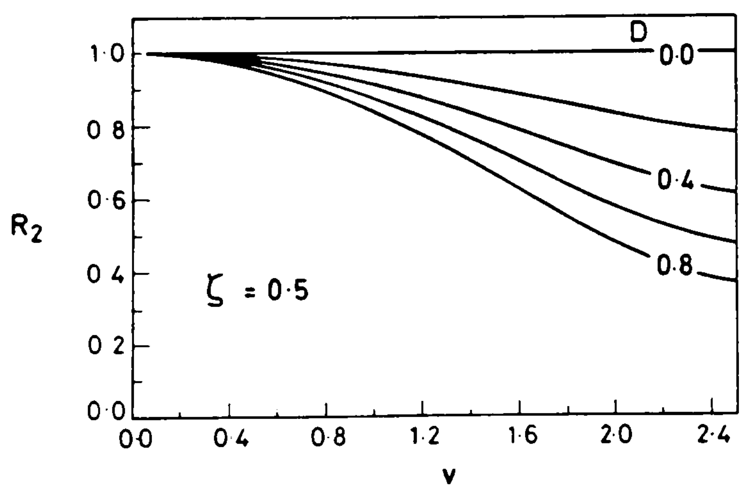

Figure 2.9: *Ratio R_2 for a damped wave.*

the damping factor. The maximum slope of the phase profile(S_o) is independent of D, but its position follows the trough of the intensity profile.

2.8 Volume effect

This section contains an extension of the previous 2–dimensional calculation to allow for fluctuation of arbitrary interaction length. The reasoning will follow Doyle and Evans(1985,c), but the scattering geometry will be slightly different due to the inclusion of a lens.

In the case of $D_1 + Z_1 = D_2 = f$ and $Z_2 = 0$, the field at the detector plane can be calculated as:

$$U_d = \mathcal{F}\left\{(U_g \cdot t_p) * h_{z1}\right\} = (\tilde{U}_g * \tilde{t}_p) \cdot \tilde{h}_{z1} \tag{2.27}$$

which involves only one convolution. The effect of a thin wave is as before:

$$t_p = e^{-j\Delta\phi} \simeq 1 - j\Delta\phi = 1 - r_e\lambda n_e(x,y,t)\delta(z) \tag{2.28}$$

and its Fourier transform is

$$\tilde{t}_p = \delta(\mathbf{K})\delta(\omega) - r_e\lambda e^{-jK_zZ} n_e(\mathbf{K},\omega). \tag{2.29}$$

The total field of the whole plasma is then the sum (integral at the limit) of the light scattered by all the planes comprising it. In his development, Doyle used a constant distribution along the axial direction Z (top hat) which produces large side lobes in the intensity field. A more physical distribution which possesses a continuous derivative would be a Hanning window. These types of distribution are frequently used in temporal sampling to reduce side lobes (Bendat and Piersol,1971). The total field will then be

$$U_d = \int_{z_a}^{z_b} (\tilde{U}_g * \tilde{t}_p)\tilde{h}_{z1} \cdot \left(1 - \cos(2\pi\frac{z - z_c}{L})\right) dz$$

where $L = z_b - z_a$ and $z_c = (z_a + z_b)/2$.

The plasma wave can be represented when it crosses obliquely the incident light beam at an angle $\pi/2 + \theta$ by

$$\tilde{n}_e(r,t) = \tilde{n}_{eo}(r,t)\sin(K_x x + K_z z - \Omega t). \tag{2.30}$$

where $K_x = K\cos\theta$ and $K_z = K\sin\theta$.

The total intensity can then be found after performing the integration of the field along the z direction (for small θ) to yield

$$\begin{aligned} I_{ac}(u_x,u_y,t) = {} & \overbrace{\frac{P_0}{\pi W_i^2}\frac{(\tilde{n}_e r_e \lambda L)}{2}\exp\left\{-(u_x^2+u_y^2)-\frac{v^2}{2}\right\}}^{C} \\ & \cdot\left\{\cos(\omega t)\underbrace{(S_- e^{u_x v} - S_+ e^{-u_x v})}_{g} + \sin(\omega t)\underbrace{(C_- e^{u_x v} - C_+ e^{-u_x v})}_{h}\right\} \end{aligned} \tag{2.31}$$

where

$$\begin{aligned} Q &= \frac{K_x^2 L}{k_l} = \frac{l v^2}{z_r} \qquad\qquad \xi = \frac{K_z k_l}{K_x^2} = \frac{K_z z_r}{v^2} \\ C_\pm &= \cos(v\zeta_1 A_\pm)\left(\mathrm{sinc}(\Theta_\pm) + \frac{1}{2}\mathrm{sinc}(\Theta_\pm + \pi) + \frac{1}{2}\mathrm{sinc}(\Theta_\pm - \pi)\right) \\ S_\pm &= \sin(v\zeta_1 A_\pm)\left(\mathrm{sinc}(\Theta_\pm) + \frac{1}{2}\mathrm{sinc}(\Theta_\pm + \pi) + \frac{1}{2}\mathrm{sinc}(\Theta_\pm - \pi)\right) \\ \Theta_\pm &= \frac{Q}{2}\left(\frac{1}{2} \mp \frac{u}{v} - \xi\right). \end{aligned}$$

The intensity and phase profile will be obtained in the usual way by using equation 2.24. Profiles are shown in figure 2.10 for the specific case of $\zeta = 1$.

As pointed out in section (2.3), Q is the parameter which determines the type of scattering prevailing and has arisen naturally from the theory. If $Q \ll 1$ the $sinc(x)$ tends toward 1, so that I_{ac} becomes symmetric and equal to the ideal thin wave case, which is the Raman-Nath limit. For $Q \gg 1$, the intensity at the detector plane is negligible apart from the position where the argument of the $sinc$ function equals zero *i.e.*

$$\frac{1}{2} - \frac{u}{v} - \xi = 0$$

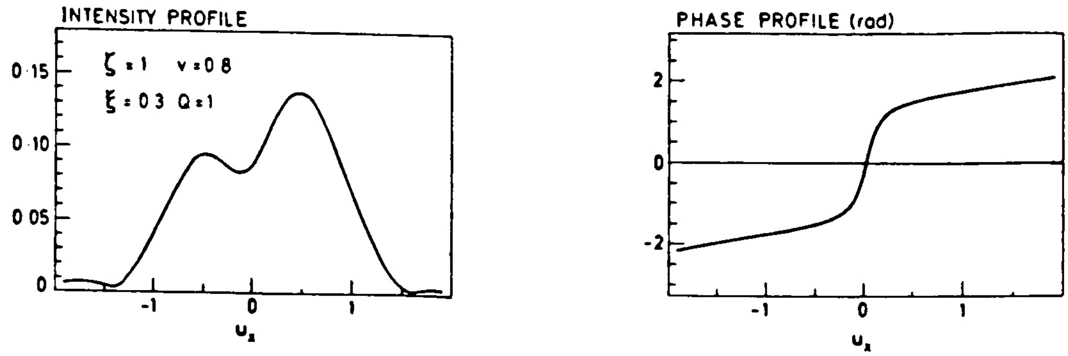

Figure 2.10: *Intensity and phase profile due to the volume effect.*

At the first order of diffraction ($u/v = 1$), the above equation reduces to the familiar Bragg condition

$$K = 2k_l \sin(\theta)$$

The profiles are asymmetric only when θ is different from zero.

2.9 Effect of the K-spectrum width(ΔK effect)

Criticism of the Far-Forward Scattering theory often lies with its simplified treatment of turbulence as a finite sum of monochromatic waves. Results from conventionnal "finite angle" scattering (Mazzucato, 1978; Slusher and Surko,1980) indicate that the density fluctuation has a finite width in the wavenumber spectrum at a given temporal frequency.

To account for this broadening, we will employ the following model of turbulence to calculate the scattering intensity:

$$n_e(K,\Omega) = \frac{\delta(K_y)}{2\Delta K\sqrt{\pi}}\left\{\delta(\omega-\Omega)e^{-\left(\frac{K-K_0}{\Delta K}\right)^2} - \delta(\omega+\Omega)e^{-\left(\frac{K+K_0}{\Delta K}\right)^2}\right\} \tag{2.32}$$

where ΔK is the width of the K spectrum around the central wavenumber K_0. The representation of the spectrum by a Gaussian distribution allows the scattered field to be calculated analytically; it reverts to the ideal thin wave case in the limit

$\Delta K \rightarrow 0$. The inverse Fourier transform of $n_\epsilon(K,\Omega)$ gives:

$$n_\epsilon(x,t) = \cos(K_0 x - \Omega t)\exp - \left(\frac{\Delta K\ x}{2}\right)^2 \tag{2.33}$$

This equation represents a wave packet of finite extent (ΔK^{-1}) along its direction of propagation which is fixed in space around the probing beam ($x = 0$). The packet broadens when ΔK gets smaller as expected from the theory of Fourier transform (Bracewell, 1986).

The scattered field is obtained as for the previous section, by replacing $n_\epsilon(K,\Omega)$ of equation 2.32 into the integral equation 2.27 via equation 2.29. We obtain after integrating over y:

$$I_{ac}(u_x,t) = \overbrace{\frac{P_0}{\sqrt{\pi}\omega_s}\frac{(\bar{n}_\epsilon r_e \lambda L)}{2\delta_v{}^{1/4}}\exp\left\{-\frac{u^2}{2}(1+\varepsilon_r)\right\}\exp\left\{-\frac{v^2\varepsilon_r}{2}\right\}}^{C}\cdot \tag{2.34}$$
$$\left\{\sin(\Omega t)\underbrace{\{e^q\sin(\theta_-) - e^{-q}\sin(\theta_+)\}}_{h} + \cos(\Omega t)\underbrace{\{e^{-q}\cos(\theta_+) - e^q\cos(\theta_-)\}}_{g}\right\}$$

where

$$\begin{aligned} \theta_\pm &= \frac{v\zeta_1}{\delta_v}\left(u \pm \frac{v}{2}\right) \mp f(u_x) \pm \theta_\epsilon & \theta_\epsilon &= \frac{1}{2}\arctan\left(\frac{\zeta_1\ \Delta v^2}{2+\Delta v^2}\right) \\ \delta_v &= [(2+\Delta v^2)^2 + (\zeta_1\ \Delta v^2)^2]/4 & \varepsilon_r &= [(1+\zeta_1{}^2)\Delta v^2 + 2]/2\delta_v \\ f(u_x) &= u_x{}^2\zeta_1(\delta_v - 1)/2\delta_v & q &= uv\varepsilon_r. \end{aligned}$$

The new dimensionless parameter which describes the ΔK effect is Δv defined as $\Delta v = \Delta K\, W_o$.

The intensity and phase profile can then be calculated using equation 2.24 and they are shown in figure 2.11 for the typical case of $\zeta = 0.8, v = 0.8$ and with 5 values of Δv. Both profiles are symmetric and the general effect of the spectral width Δv is to smear out the curve. The intensity profile decreases as Δv gets larger which arises from the $1/\zeta_v^{1/4}$ factor in eqn. 2.34. At the limit of $\Delta v \rightarrow \infty$, the latter factor becomes Δv^{-1} which means that the intensity is proportional to the physical width of the wave packet. The ΔK effect can lead to an underestimation of the actual fluctuation level if the ideal thin wave model is used.

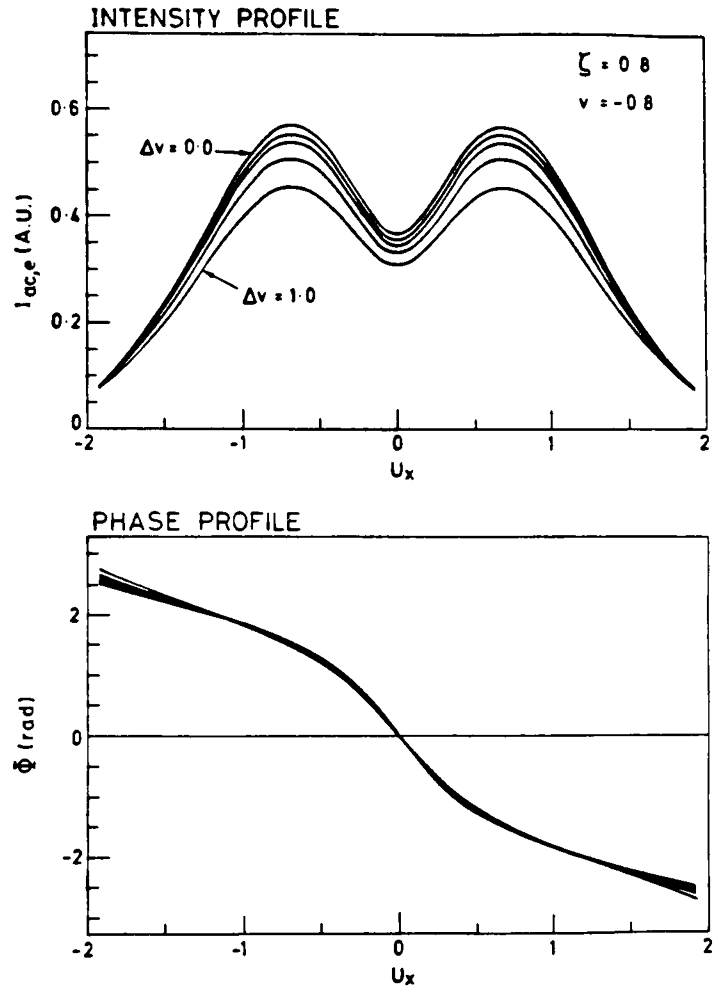

Figure 2.11: *Intensity and phase profile for different Δv.*

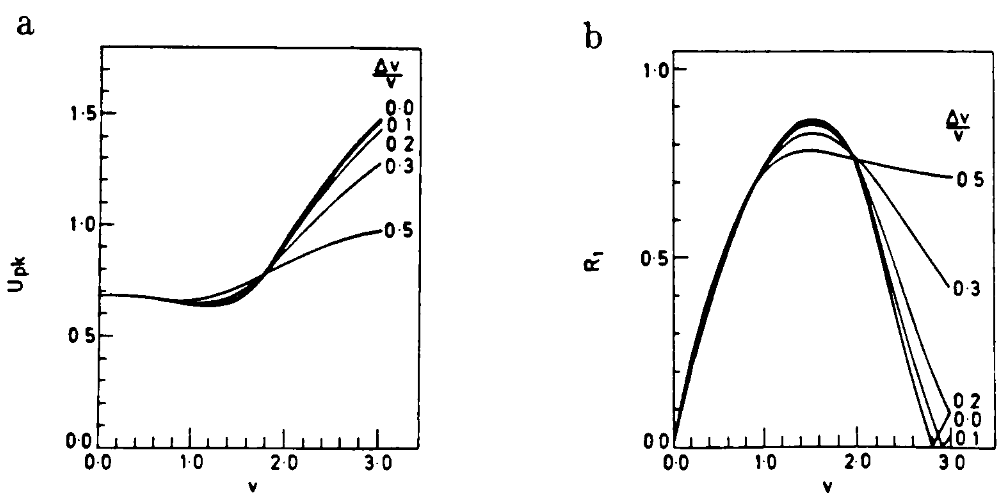

Figure 2.12: *Plot of (a)peak position and (b)ratio R_1 in function of Δv and v for the ΔK model.*

The ratio of the peak to the trough in the intensity profile (R_1) and the position of the peak (u_{pk}) are weakly dependent on ΔK for v smaller than 1 as can be seen on figure 2.12 . For large value of v which is the domain of traditional finite angle scattering, the ΔK effect is more important.

The phase profile is rather insensitive to changes in ΔK for small u ($|u| < 2$). At very large u ($|u| >> 1$), the slope of the phase profile is given by:

$$S_{\infty} = \frac{\zeta v}{\delta_v} + \frac{\zeta u}{\delta_v}(\delta_v - 1), \tag{2.35}$$

while the slope at the origin is

$$S_0 = \zeta v + \varepsilon_r v \cot\left\{\frac{\zeta v^2}{2} + \theta_\epsilon\right\}. \tag{2.36}$$

The profile equations of the ideal thin wave case are easily retrieved by taking the limit ($\Delta K \rightarrow 0$). The results of this section are for the particular case of a Gaussian shape $n_e(K, \Omega)$ with a specific phase spectrum. In practice however, the form of $n_e(K, \Omega)$ might be different, but the main smearing out effect of the spectrum width will remain.

2.10 Summary

The calculations of the scattering field due to different phase wave configurations have been performed in this chapter. The main characteristics of the various FFS models are listed in table 2-1. Most of the models are asymmetric and they all have in common the variables A(amplitude), v(dimensionless wavenumber) and ζ(normalised axial position). Under certain conditions, all the models reduce to the single wave model.

To quantify the differences between the profiles of the models, we defined 7 shape parameters. Table 2-2 summarises their dependencies for each model using an equation or a figure. The volume effect has not been included since it is found to be negligible for all our experiments.

Model	Symmetric	Nb. of humps	Extra variables
1 wave	yes	2	—
2 wave	no	2–3	$\theta, a, \zeta_1, \zeta_2$
Damping	no	2	D
ΔK	yes	2	Δv
Volume effect	no	many	Q, ξ

Table 2.1: *Summary of various FFS models.*

Model	u_o	u_{pk}	R_1	R_2	S_o	S_∞	ΔS_∞
1 wave	0	fig. 2.5	fig. 2.5	1	eqn. 2.22	ζv	0
2 waves	–	–	–	–	–	–	–
Damping				fig. 2.9	–	ζv	D
ΔK	0	fig. 2.12	fig. 2.12	1	eqn. 2.36	eqn. 2.35	0

Table 2.2: *Summary of shape parameters for intensity and phase profile.*

Chapter 3

Optical system

The apparatus built for these far forward scattering (FFS) experiments is described in this chapter. We will discuss every part of this system from the laser source up to the signal processing stage at the computer end. The description will be kept general insofar as all the parameters of the three main experiments(ultrasonic waves, air jet and plasma turbulence) will be included. A discussion on the resolution of the amplitude level($\Delta\phi$) and of the wave number(K) will also be given.

3.1 Laser

A radio-frequency (60 MHz) excited waveguide laser CO_2 laser made by Edinburgh Instruments (model WL4) was used in this FFS experiments. It emits radiation at 10.6 μm and can deliver up to 4W of power in the TEM_{00} Gaussian mode. The intensity profile of the laser beam has to be very close to a pure Gaussian to fulfill one of the main assumptions in the theory. Figure 3.1 illustrates the profile quality of our laser by plotting a measured profile (data points) with the best Gaussian fit (solid line). The beam waist of the laser (W_l) defined as the radius at e^{-1} in intensity was measured to be 4mm ($\theta_{div.}$ = 4 mrad) in both vertical and horizontal directions and is situated at its output coupling minor. The laser is kept at constant temperature (12 °C) by a water cooling unit to stabilise the output power and the peak wavelength.

The choice of the wavelength is dictated by the availability of good quality laser, detectors and optics at 10μm and also by the limited access to the plasma machine. For longer wavelength lasers such as deuterated methyl fluoride(CD_3F), and for the plasma wavelength of interest, the Bragg angle (equation 1.2) is too large for the size of the access window (d=2.5cm).

3.2 Optical System

The determination of the optical parameters (waists, focal length, position of the waists) requires a rough knowledge of the fluctuation to be studied. The influence of these free parameters on the scattering signal manifests itself through the dimensionless variables ζ, v, u ...In the following, the ideal thin wave model with Z_2=0(experimental layout) was used to find the optimum parameters.

Figure 2.5(b) shows the intensity of the peak scattering signal (I_{ac}) as a function of v. To maximise our signal, the waist in the front focal plane (W_o) is chosen to make the normalised wave number (v) around unity since the curve peaks for that value. From drift wave theory of plasma turbulence (Liewer,1985), we expect $K_p\rho_s \lesssim 0.5$, where $\rho_s = v_{th,e}/\Omega_i$; therefore the optimum waist should be around $W_o \simeq 2\rho_s \simeq 2.5$ mm. In the ultrasonic experiment, the range of K generated varied from 0.2 mm^{-1} to 1.2 mm^{-1}(10-65 kHz) and a beam waist(W_o)of 1 mm was selected. The air jet K-spectrum was less well known and since we wanted to look primarily at larger K, the waist $W_o = 0.4$ mm was chosen.

The position of the beam waist with respect to the centre of the disturbance (Z_1) was chosen so as to facilitate data analysis. The position of the peak of the intensity profiles (u_{pk}) is plotted in figure 3.2 as a function of the intensity

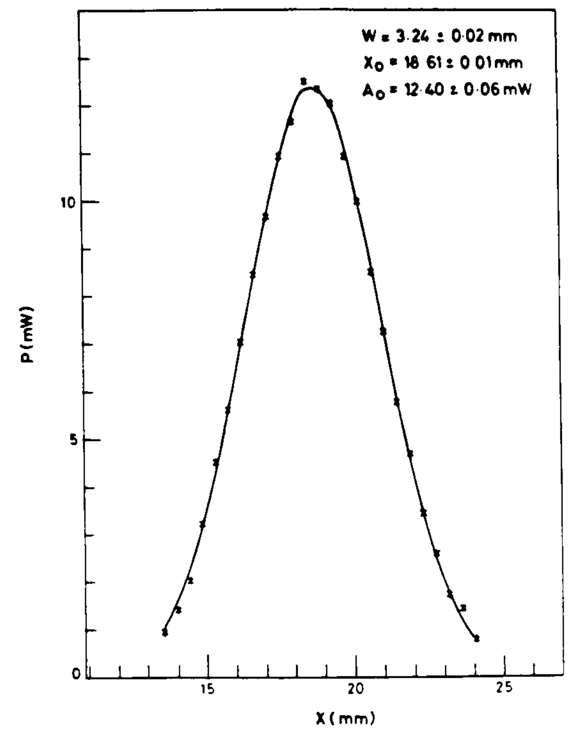

Figure 3.1: *Profile of laser beam with best-fit to Gaussian curve.*

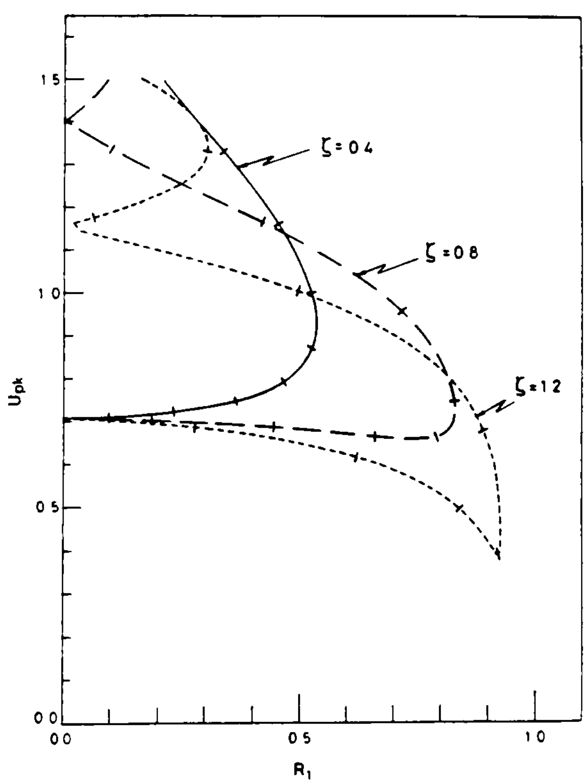

Figure 3.2: *Plot of peak position in function of R_1 and ζ with v as a marker.*

ratio between the through and the peak of the profile (R_1) for three values of the normalised distance $\zeta = Z_1/Z_r$. These two factors (u_{pk} and R_1) are good indicators of the envelope shape. The parameters of the curve (v) varies from 0 to 3 and the marker indicates the values i/3 for i=1,9. For low value of $\zeta(< 0.3)$, the ratio R_1 does not vary much with v and the error on the fitted parameters would be larger. At large values of $\zeta(> 1.5)$, the ratio R_1 saturates for large portion of v making it indiscernible for fitting purposes. The optimum position seems to be around $\zeta \approx 0.8$ where a good excursion of the ratio R_1 is obtained (0-0.8) without any saturation. At this position (ζ=1) moreover, the curvature of the Gaussian beam is maximum which is consistent with the notion that the curvature influences the scattering signal. This value was chosen for the ultrasonic and air jet experiment but due to a lack of time (dismantling of the machine) the experimental value for the plasma scattering was $\zeta = 0.3$.

The waist at the image plane (W_i) is chosen as a function of the detector size and its total lateral excursion. In this experiment, an array of twelve detectors (d_w = 0.5mm) spaced by 0.8mm has been used. To include most of the changes in the profiles ($I_{ac,e}, \Phi$), the distance between the extreme detectors should be larger than $3W_i$ or conversely the waist $W_i <$ 3mm for our array.

The detector width (d_w) creates a lower limit to the waist. If the ratio $\delta = d_w/W_i$ is too large the detector will smear out changes in the profile and it is obviously preferable to use either smaller detectors or a larger waist. Calculations of this effect were carried out by integrating the AC Intensity (I_{ac}) weighted by a shifted Gaussian profile having a half width at e^{-1} of d_w to represent each detector. The new I_{ac} obtained differs from equation 2.17 by factors of $1/(1 + \delta^2/4)$ for each $A_\pm$. If we consider this factor to be negligible when it is bigger than 0.9, then δ has to be smaller than 0.2 or equivalently $W_i >$ 2.5mm for the detector size.

All the previous arguments are only valid for the ideal thin wave model and for other models, especially the 2 waves model with its rapid profile changes, the minimum waist size (W_i) can be expected to be larger.

		Ultrasonic	Air jet	Plasma
$< K >$	[cm^{-1}]	10.	>10.	2.0
W_o	[mm]	1.0	0.4	2.6
Z_r	[m]	0.6	.01	4.1
ζ	[—]	0.8	0.8	0.3
W_i	[mm]	2.78	2.1	2.7
f	[m]	1.65	0.5	4.0

Table 3.1: *Optical parameters.*

As demonstrated, the size of the detector and the total excursions produce opposite constraint on the waist size W_i. A compromise was reached by selecting a waist of around 2.8 mm so that most of the profile can be recorded.

The focal length (f) of the lens can now be calculated from the knowledge of the two waists (W_o, W_i) by using

$$k_l W_o W_i = f. \tag{3.1}$$

From our limited supply of lenses, we adjusted the waists around their optimum values to fit our lenses inventory. Table 3-1 summarises the chosen optical parameter for the different experiments carried out in this investigation.

The laser beam was directed along its optical path by gold coated mirrors to reduce power losses. The access window for the torus were made of Zinc Selenide (ZnSe) which is transparent to both infrared radiation (10.6 μm) and visible light, facilitating alignment.

Most of the focusing elements were concave spherical mirrors with their focal length (f) equals to half of the radius of curvature. Due to the criticality of f, precise measurement of the radius of curvature was made using a 3 axis coordinate measuring machine which yields an uncertainty of few percents($< 3\%$) on the value of the focal length. The main disadvantage of using reflective optics is the production of astigmatism when the beam is off axis. This aberration can be neglected when the angle between the incident and reflected light on the mirror is smaller than 0.05 radians. For that reason, focusing elements of focal length below 1m (as for the air jet) were not mirrors but instead refractive plano-convex Germanium lenses.

The alignment of the laser beam through the optical arrangement was made using the Gaussian optic formalism (Siegman, 1971) and these equations are summarised in Appendix A. In order to apply them, a knowledge of the intensity profile before and after each optical element was necessary. Measurements were performed initially by translating a slit and a power meter manually across the laser beam. Subsequently, a beam profiler made by Delta Development (Mark 4) was acquired to perform this task. The profiler consisted of a linear array of 60 pyroelectric elements together with amplifiers and a display unit. The signal from each detectors was sampled with an A to D converter and subtraction of the background radiation was done automatically by the beam profiler. Software was written to transfer the sampled power of each element to a computer and a least squares fit of the data to a Gaussian profile $P_o \exp -((x - x_o)/W)^2$ was performed to extract the three beam parameters: Waist, peak power and position of the peak. Figure 3.1 is the result of such treatment.

By measuring the width (w_i) at different positions (z_i) along the optical path, we can infer the position (Z_o) and value of the beam waist (W_o) by using the equation (appendix A):

$$w_i = W_o \left[1 + \left(\frac{z_i - Z_o}{k_l {W_o}^2} \right)^2 \right]^{1/2} .$$

Again a least squares routine was used to fit the data points with the last equation and figure 3.4 shows the predicted beam waist (W_o) determined from widths of the Gaussian beam at various locations along its path.

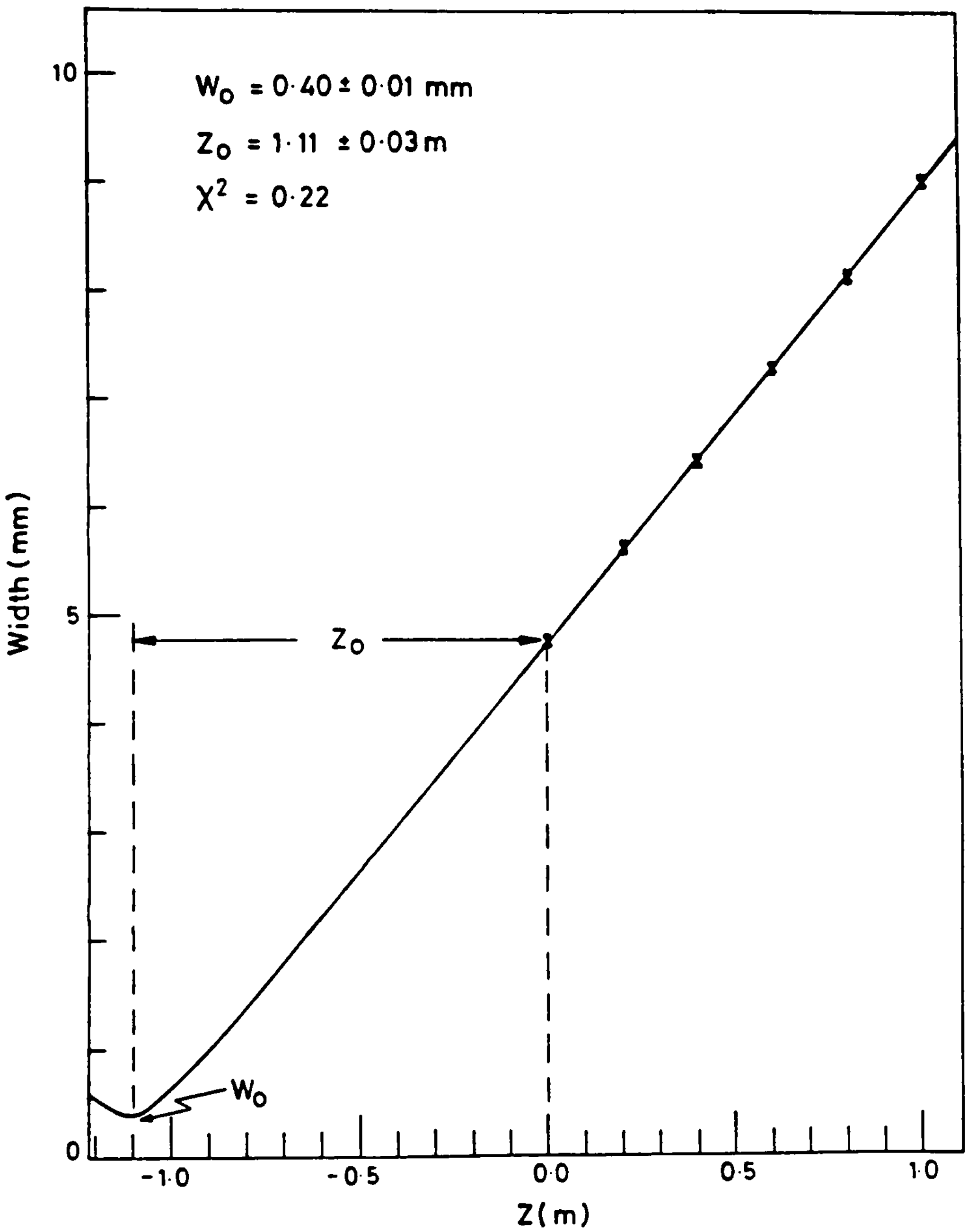

Figure 3.3: *Experimental determination of spot size variation with distance for a Gaussian beam and comparison with theory.*

3.3 Detector

A linear array of 12 photoconductive detectors made of Mercury-doped Germanium (Ge:Hg) and built by Santa Barbara Research Company (SBRC) was used in our experiments. Incident radiation modifies the conductivity of the detector by generating holes in the semiconductors in proportion to the power of the incident light. Their spectral response covers the band from 2 to 12 μm with the peak wavelength being 10.6 μm. Each detector has a sensitive area of 0.5 mm^2 (1mm $\times$ 0.5mm) and they were separated from each other by 0.8mm.

The operating temperature of the detectors was usually around 10K and this was achieved by means of a liquid Helium cooling unit. Due to the limited cooling capacity of the cryo-cooler at this temperature (<.2W), two radiation shields were designed and built to reduce the heating by the surroundings. One shield was at 77K while the other one was at 10K and both were gold coated to increase their reflectivity.

The linear array and the radiation shield were inside a vacuum shroud (10^{-4} Torr) to eliminate heat conduction and convection. Figure 3.5 shows all the elements of the detector assembly. To avoid burning the detector or its connector due to an increase of laser power or failure of the cryo-cooling unit, a shutter was controlled to block the light beam when the temperature of the detector exceeded 12K.

A static calibration of each detector was performed in two stages to measure the variation of the detector responsivity ($\alpha(v)$) with the bias voltage. This was necessary to ensure that the measured scattered envelopes are unaltered by the relative responsivity of each detector.

The first step was an absolute calibration for a fixed inverse bias voltage of 20V. By varying the illuminating power (P) of a focused beam (W_{det}=0.05mm), a linear relation was obtained between the power P and the conductance of the detector G

Figure 3.4: *Detector assembly.*

and was given by:

$$G(P,V) = P\alpha(V) + G_d(V) \tag{3.2}$$

where V_b is the bias voltage across detector, G_d the dark conductance and $\alpha(v)$ the responsivity of the detector [Siemens/Watt].

The dark conductance was around 0.2×10^{-6}S for all detectors and rather insensitive to changes in bias voltage from 0 to 50V. Unfortunately some detectors showed optical cross talk which was traced to reflection from the slit of the radiation shield due to the comparatively large divergence angle of the laser beam (0.06 rad).

For this reason, a different approach to the absolute calibration was adopted. The method is based on the verified assumption that our laser beams are indeed Gaussian. By shining a beam of known waist (W) and power (P) on the array, it is possible to deduce the power onto each detector by calculating

$$P_{det}(u) = \frac{P_o}{2} \operatorname{erf}\left(\frac{0.5}{W}\right) \cdot \left[\operatorname{erf}\left(|u_1| + \frac{d_w}{W}\right) - \operatorname{erf}\left(|u_1| - \frac{d_w}{W}\right)\right] \tag{3.3}$$

where erf( ) is the error function, $u_1 = x_1/W_d$ the normalised position of the detector and d_w =0.5mm is the width of the detector. A simultaneous measurement of the current and voltage of the detector yields the conductance and the responsivity can then be calculated using equation 3.2.

This process was carried out for different powers and peak position of the beam to eliminate any spurious effects. Figure 3.5 shows the responsivity obtained this way (0) compared to the data given by SBRC(x) with the error bars indicating the spread of the measured points.

Since it was found that the responsivity varied with bias voltage, we performed a relative calibration of the detectors. It consisted of taking the ratio of the conductance for two different optical powers but at the same voltage; so that

$$\frac{(G - G_d)_1}{(G - G_d)_2} = \frac{\alpha(V)P_1}{\alpha(V)P_2} = \frac{P_1}{P_2}. \tag{3.4}$$

By repeating this process for different combinations of voltage and powers it is possible to determine the proportionality between each of the powers without

Det.	G_{dark}	α_0	α_1	α_2	χ^2
	S	SW^{-1}	$SW^{-1}V^{-1}$	$SW^{-1}V^{-2}$	
A	0.113E-05	0.365E-01	-0.155E-03	-0.193E-05	0.194E+00
B	0.762E-06	0.303E-01	-0.179E-03	-0.542E-06	0.533E+00
C	0.139E-05	0.346E-01	-0.233E-03	-0.109E-06	0.126E+00
D	0.173E-05	0.264E-01	-0.821E-04	-0.125E-05	0.305E+00
E	0.122E-05	0.302E-01	0.218E-03	-0.943E-05	0.144E+01
F	0.121E-05	0.315E-01	-0.981E-04	-0.247E-05	0.565E+00
G	0.147E-05	0.305E-01	0.644E-04	-0.526E-05	0.107E+00
H	0.874E-06	0.315E-01	-0.322E-04	-0.355E-05	0.543E+00
J	0.103E-05	0.328E-01	-0.169E-03	-0.153E-05	0.131E+00
K	0.119E-05	0.317E-01	0.625E-04	-0.606E-05	0.989E+00
L	0.806E-06	0.400E-01	-0.159E-03	-0.249E-05	0.440E+00
M	0.889E-06	0.352E-01	-0.273E-03	0.863E-06	0.171E+00

Table 3.2: *Coeficients of detectors responsivity.*

knowing their exact values. An initial setting of power was chosen from those proportionality relations to calculate the responsivity $\alpha(v)$ which is the rate of change of the conductance for a change in irradiating power. A comparison between the value thus obtained and the absolute responsivity at a given voltage was then used to scale the power of the relative calibration. With this new setting of power, the responsivity was evaluated at all the voltages. Figure 3.6 shows the variation of the conductance versus power for different voltages and the variation of the inverse of the responsivity versus the voltage. The relation between the responsivity and the voltage was found by fitting numerically the results with this second degree polynomial

$$\alpha(V) = \alpha_0 + \alpha_1 V + \alpha_2 V^2. \tag{3.5}$$

Table 3.2 lists the coefficients α_0, α_1 and α_2 for each detector which gave the best fit for the responsivity curve. The power onto each detector can then be found by calculating $\alpha(v)$ from the above equation and using equation 3.2.

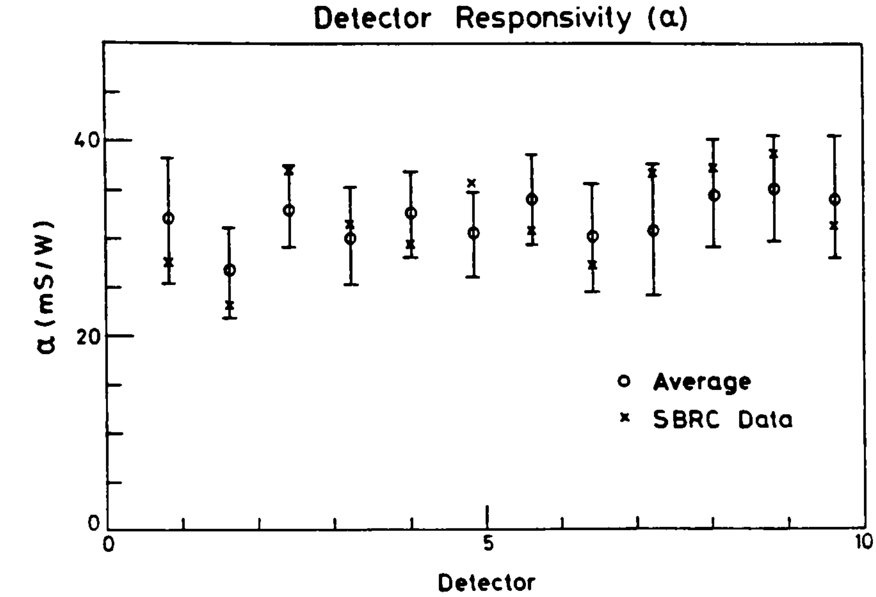

Figure 3.5: *Comparison of measured detector responsivity with the SBRC calibration.*

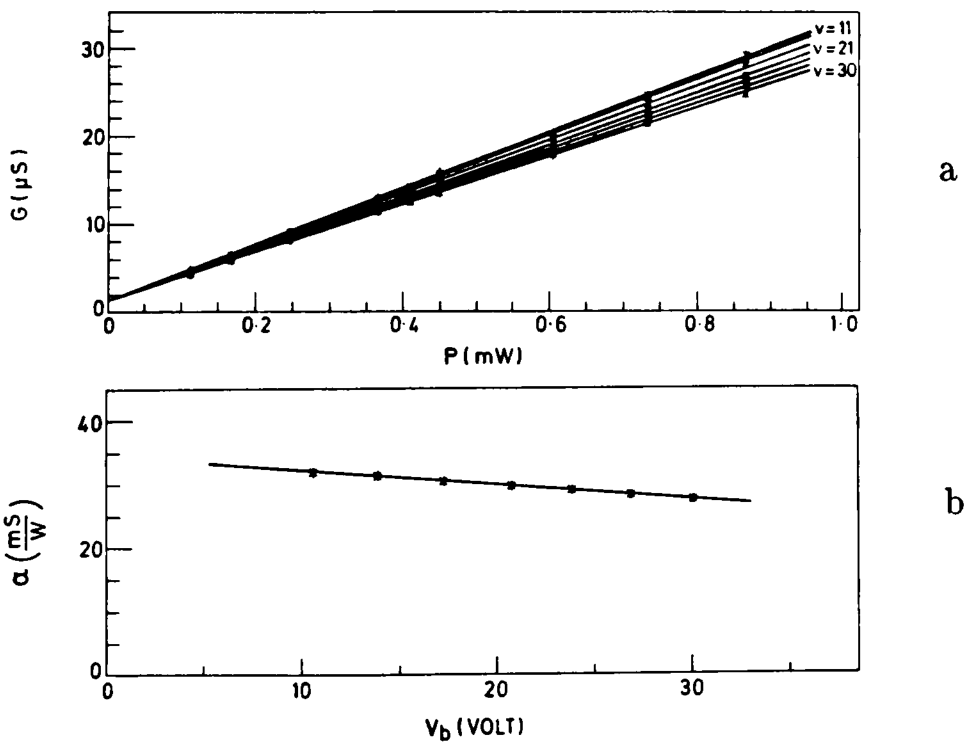

Figure 3.6: *(a)Conductance versus power; (b)responsivity versus voltage.*

3.4 Amplification Stage

Each detector is followed by an amplifier which discriminates between the fluctuation signal (I^{ac}) and the Gaussian beam (I^{dc}). Figure 3.7 illustrates the various components of the amplifier and the input capacitor (C_{in}) is the separating agent between the DC and AC amplifier. In the following, we will briefly describe both parts of the amplifier.

The aim of the DC amplifier is to extract the bias voltage (V_b) and the current going through the detector (I^{dc}) to allow us to calculate the DC-power falling onto the detector from a knowledge of its conductance via equation 3.2. The expected values for the current and the bias voltage are around 1mA and 20V respectively. Since the latter value (V_b) is too large to be stored directly by an ADC, we reduced the bias voltage by a resistive voltage divider (1/11) and isolated it from the circuit by a buffer amplifier (IC-1) to give V_v^{dc}. The current I^{dc} is monitored by the voltage difference it induces when passing though the resistance R_1(2.7kΩ). An instrumentation amplifier (IC-2=AD524D) with an internal gain of 10, detects this difference and produces V_i^{dc}. Both signals V_v^{dc} and V_i^{dc} are digitised on a LeCroy 8212 ADC (12 bits, 5kHz sampling rate) before being stored on an LSI-11 micro-computer. All the resistances in the voltage divider($R_2 - R_6$) and R_1 are of the wound type with high accuracy (0.25%) so as to minimise the errors on the measured value.

With this circuit, the conductance of the detector is given by:

$$G_{det} = \left(\frac{1.1V_i^{dc}}{2.7k\Omega}\right) \cdot \left(\frac{1}{11V_v^{dc}}\right) - \frac{1}{1.1M\Omega} \tag{3.6}$$

Each circuit was tested by biasing a known resistance (22.2kΩ) and measuring its resistance via V_i^{dc} and V_v^{dc}. The average measured value of each amplifier is 22.26kΩ which compares well with the expected one. Its standard deviation of 1.6% (340Ω) is in agreement with the 0.25% uncertainties of each of the 5 resistors.

The AC part of the amplifier transforms the fluctuating current of the detector

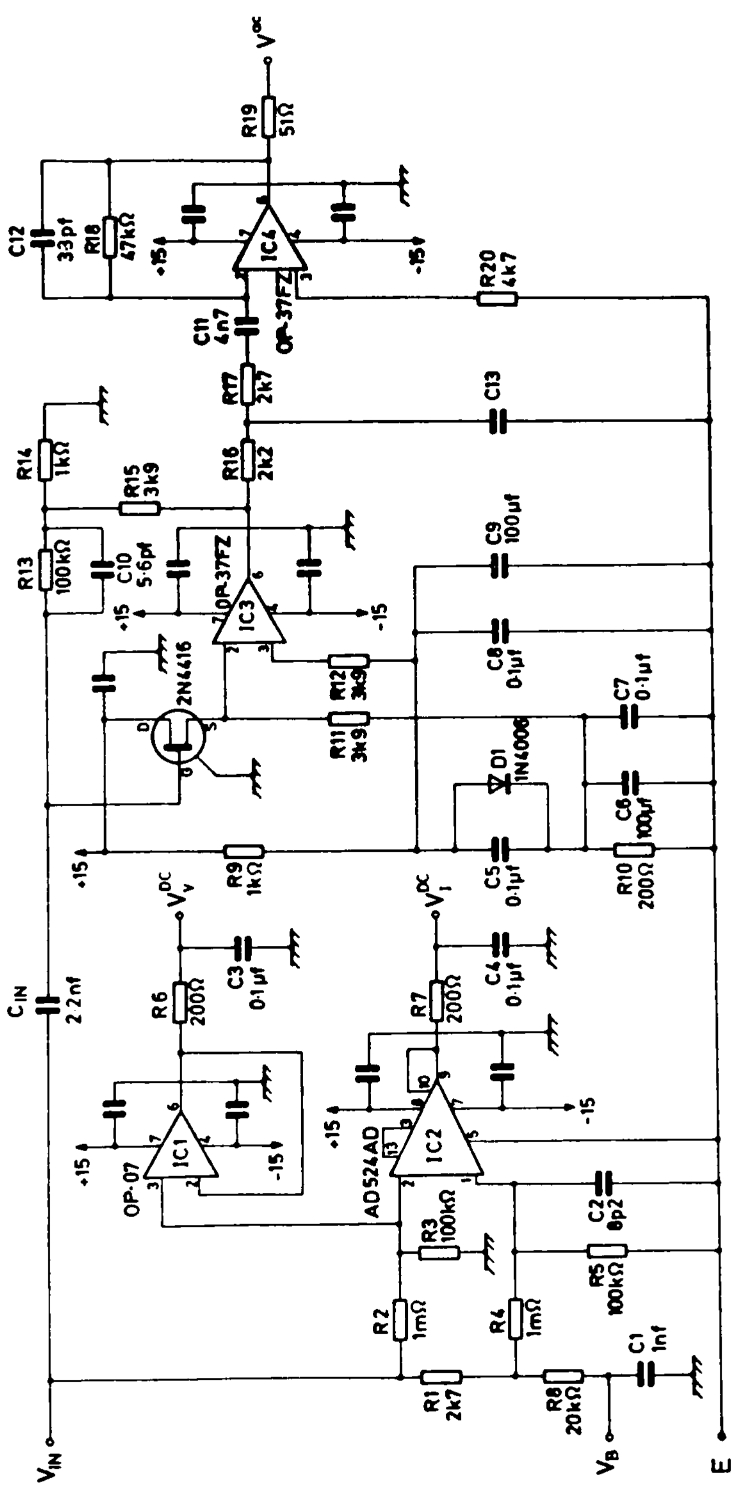

Figure 3.7: *Circuit diagram of FFS amplifier.*

into volts ready for digitising. A low noise amplifier with bandwidth from 30-600 kHz was designed for this purpose and we will briefly describe its circuitry.

As stated earlier, the capacitor C_{in} acts as a high pass filter and its value is chosen such that the cut-off frequency is around 30kHz. After passing through C_{in}, the signal is amplified by a transresistance amplifier of gain 5×10^6S for which a JFET was added at its input stage to reduce the noise level. The operational amplifier (IC-3) chosen was the OP-37 with its large gain bandwidth (63MHz) and low noise figure ($3\text{nV}/\sqrt{Hz}$ at 1kHz). To avoid oscillations, a voltage divider was included in the feedback loop to obtain a voltage gain of 5 which is the optimised value for the OP-37. The signal was then further amplified by a factor of 10 from IC-4 with its resistive network. The capacitors C_{11} and C_{12} limited the bandwidth of the last stage of amplification from 30 to 600 kHz.

All the amplifiers were shielded from one another so that ground loops and cross talk were minimised by carefully designing the PC-board and the shields of the connectors. The input cable from the detector head to the amplifier input(V_{in}) were made as short as possible to reduce their capacitive effect on the circuit. The bias of each detector came from independent batteries instead of power supply so as to avoid any mains pick-up and they were connected to the circuit by entry point V_b.

After leaving the amplifiers, the AC signal went through another adjustable amplifier (Culham Quad Amplifier) so as to occupy the 10V dynamic range of the LeCroy 8210 ADC (10 bits, 1MHz sampling rate). To avoid any aliasing of the lower frequency, a low pass filter made by Kemo filters (8 orders filters) with cut-off frequency of 400 kHz was used. The digitised data for the fluctuating signal was then stored on magnetic tapes for later processing in a LSI-11 microcomputer.

As for the photoconductive detectors, a full knowledge of the frequency response (amplitude and phase) of each amplifier is required to avoid any biasing in the fitting of the reconstructed envelope. The calibration of the whole amplification system from the detector input cables up to the anti-aliasing filters was carried out by using a white noise generator (Bruel and Kjær 1405) as input to the amplifiers through a 20 kΩ resistance. By sampling and storing simultaneously the input (X) and output (Y), we can infer the frequency response of our system ($H(f)$) by calculating (Bendat and Piersol, 1980):

$$H(f) = \frac{\mathcal{G}_{xy}(f)}{\mathcal{G}_{xx}(f)} = \frac{|\mathcal{G}_{xy}|}{|\mathcal{G}_{xx}|} e^{-j\Theta_{xy}} \tag{3.7}$$

where $\mathcal{G}_{xy}$ is the cross spectrum of the input and output $= \sum X^*(f)Y(f)$, $\mathcal{G}_{xx}$ is the auto-spectrum $= \sum X^*(f)X(f)$ and Θ_{xy} the phase spectrum. We will postpone to the next section, a fuller discussion of spectral analysis.

This estimate of H(f) is insensitive to uncorrelated noise at the output level of the amplifier to the contrary of the usual $(|\mathcal{G}_{yy}|/|\mathcal{G}_{xx}|)$. The errors of these estimates are given by (Bendat and Piersol, 1980).

$$\epsilon[|H(f)|] = \frac{|\Delta H|}{|H|} = \frac{(1-|\gamma_{xy}|)^{1/2}}{|\gamma_{xy}|\sqrt{2n_d}} \quad \text{and} \quad \sigma[\Theta_{xy}] = \sin^{-1}(\epsilon[|H(f)|]) \tag{3.8}$$

where γ_{xy} is the coherence and n_d is the number of averaging shots. As in any spectral measurement, averaging over many shots allows a reduction of the errors. In our calibration, 31 shots of 512 points (16msec) were used and this yield errors smaller than 3% for $\gamma_{xy} > 0.94$.

Figure 3.8 shows the output of such calibration for one amplifier. The top graph represents the amplitude frequency response and shows the band pass nature of the amplifier with a low frequency cut off at 40kHz and the higher cut off due to the anti-aliasing filter. The middle graph represents the phase spectrum and the bottom one represent the coherence of the signal (γ_{xy}). Above 400kHz, the coherence is too small and renders the phase spectrum useless in that neighbourhood.

Since the amplifier response is not constant over the frequency range of interest (30-300kHz), a least squares fitting of the amplitude response with the following polynomial

$$H(f) = \frac{A_o\, T_l\, f}{[(1+(fT_l)^2)(1+(fT_h)^2)^8]^{1/2}} \tag{3.9}$$

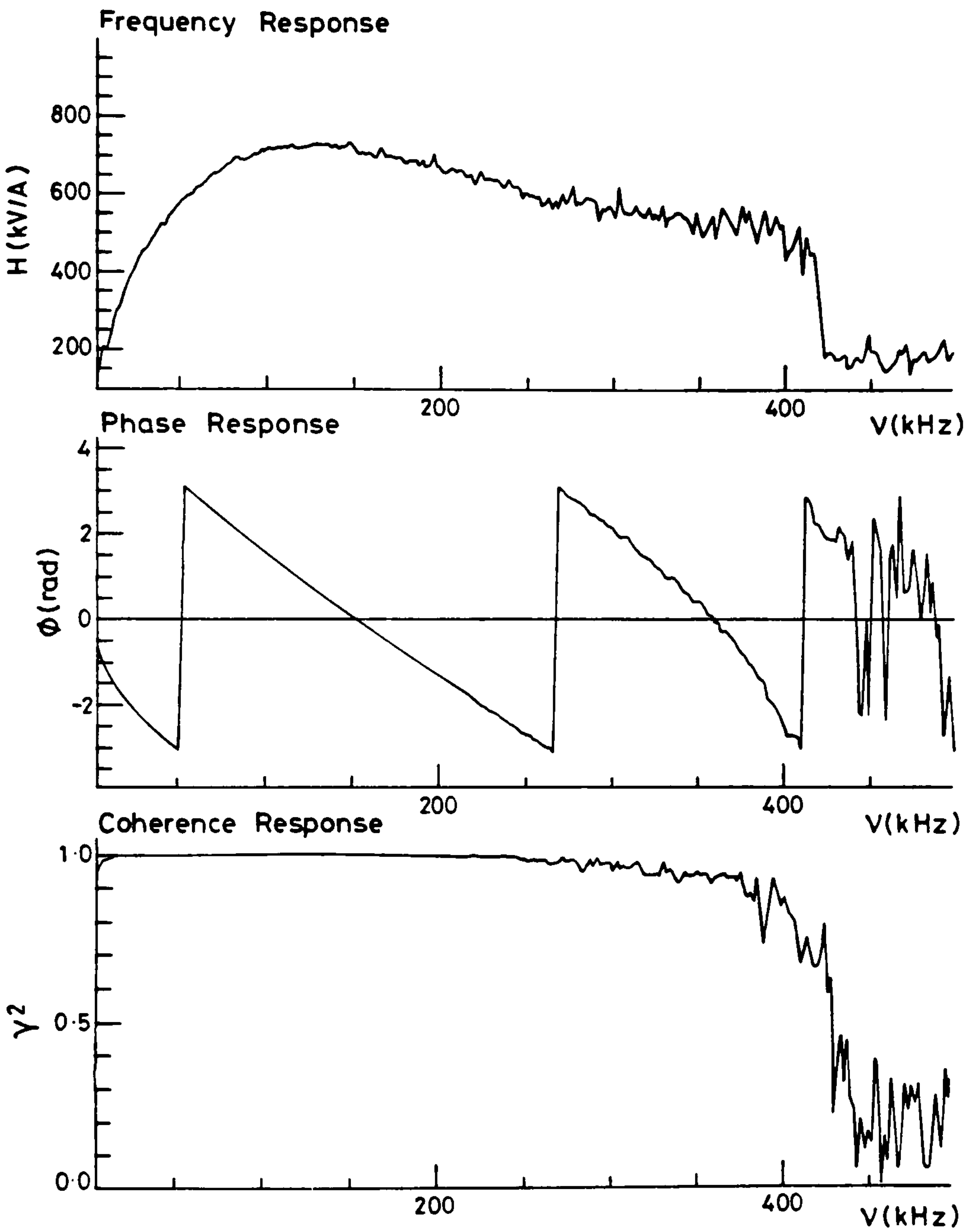

Figure 3.8: *Amplifier amplitude and phase frequency response with the signal coherence.*

Ampli.	A_0	T_l	T_h
	Ω	sec	sec
A	3.17E6	7.50E-6	2.00E-6
B	3.25E6	7.40E-6	2.05E-6
C	3.07E6	7.76E-6	2.00E-6
D	3.08E6	7.92E-6	1.97E-6
E	3.23E6	7.37E-6	2.03E-6
F	3.04E6	7.85E-6	1.92E-6
G	2.89E6	8.33E-6	1.83E-6
H	3.34E6	7.19E-6	2.12E-6
J	2.82E6	8.30E-6	1.79E-6
K	3.34E6	7.15E-6	2.10E-6
L	3.14E6	7.51E-6	2.01E-6
M	3.15E6	7.47E-6	2.02E-6

Table 3.3: *Amplifiers coefficients.*

was carried out. In the last expression, A_o is the total gain and $T_l(T_h)$ is the time constant of the low (high) pass filter. The list of the coefficients obtained in this way is written in Table 3.3 for each amplifier. The value of the phase lag introduced by the amplifier was of no importance for our analysis, but its consistency between different circuits was. Therefore, we compared the phase spectrum of the different amplifiers and found that they were within 10% of each other in the bandwidth of interest.

3.5 Signal Processing

The use of signal processing techniques is twofold. Appropriate signal processing can simplify the hardware (no bank of filters, correlators) and can add quantitative information about the structure of the turbulence which can not be obtained otherwise. Futhermore, storing the raw data in digital form also makes the smallest possible commitment to the later analysis and thus preserves maximal flexibility for an optimal processing of the data.

The following subsections are concerned with stating some of the important concepts of spectral analysis as well as for curve fitting and their application to the analysis of the FFS signal.

3.5.1 Spectral analysis

The basis of all spectral analysis of digital signal is the discrete Fourier transform (DFT). It is given for a time series x(t) of N data points sampled at an interval time Δt apart by:

$$X(f_k) = \Delta t \sum_{i=0}^{N-1} x(t_i)\exp(-j2\pi ik/N) \qquad \text{for } k = 0, 1 \ldots \frac{N}{2} - 1 \tag{3.10}$$

where $t_i = i\Delta t$ and $f_k = k/N\Delta t$. The transform is effected by means of the Fast Fourier transform (FFT) algorithm of Cooley and Tukey (1967) to reduce computational time. As a consequence of the finite length of the data set, the transform distorts the spectrum by leaking some power from one frequency range into its neighbours. To reduce this, a Hanning window was applied to the raw data or equivalently implemented by a weighted average technique in the frequency domain (Smith *et al.*, 1974), i.e.

$$X'(f_k) = 0.5X(f_k) - 0.25X(f_{k+1}) - 0.25X(f_{k-1}) \tag{3.11}$$

where $X'(f_k)$ is the new estimate

The auto-power spectrum ($\mathcal{G}_{xx}$) is obtained by calculating

$$\mathcal{G}_{xx}(f_k) = \frac{2}{N\Delta t}(X^*(f_k)X(f_k)) = \frac{2}{N\Delta t}\left(\Re e(X(f_k))^2 + \Im m(X(f_k))^2\right) \tag{3.12}$$

and it represents the amount of power in the sampled signal for the discrete frequency $|f_k|$. The factor 2 arises from the fact that $\mathcal{G}_{xx}$ is defined only for positive frequencies. The cross-power spectrum ($\mathcal{G}_{xy}(f_k)$) for the two signals x(t) and y(t) corresponds to the amount of power common to the two sampled signals at each frequency. Its computation is similar to the auto-spectrum and is given by:

$$\mathcal{G}_{xy}(f_k) = \frac{2}{N\Delta t}(X^*(f_k)Y(f_k)) = |\mathcal{G}_{xy}(f_k)|e^{-j\Theta_{xy}(f_k)} \tag{3.13}$$

where $Y(f_k)$ is the DFT of $y(t)$, $|\mathcal{G}_{xy}(f_k)| = \sqrt{\Re e(\mathcal{G}_{xy}(f_k))^2 + \Im m(\mathcal{G}_{xy}(f_k))^2}$

$$\text{and } \Theta_{xy} = \arctan\left\{\frac{\Im m(\mathcal{G}_{xy}(f_k))}{\Re e(\mathcal{G}_{xy}(f_k)}\right\}.$$

The last term ($\Theta_{xy}(f_k)$), named the phase spectrum, represents the relative phase angle between $X(f_k)$ and $Y(f_k)$ at a given frequency. Another useful quantity is the coherency ($\gamma_{xy}(f_k)$)which is defined as the normalisation of the correlated power by the total power

$$\gamma_{xy}(f_k) = \frac{|\mathcal{G}_{xy}(f_k)|}{\sqrt{(\mathcal{G}_{xx}(f_k)\mathcal{G}_{xy}(f_k)}} \tag{3.14}$$

and is bounded between 0 and 1. It is a measure of the similarity between the two signals x and y at each frequency with phase differences ignored. A large value (> 0.7) indicates good correlation while a value below 0.25 correspond to two uncorrelated signals.

To improve the estimate of the different spectra, it is common practice to smooth them in one of two ways (Bendat and Piersol, 1971). The first one is to average the spectrum over an ensemble of n_d similar records. The second way is to smooth over frequency by averaging together the results from ℓ continuous spectral components in the estimate from a single sample record. The normalised random error (ε_r(w)) defined as ($\sqrt{variance\ of\ w}/w$), is then after smoothing (Bendat and Piersol, 1980),

$$\begin{aligned}
\varepsilon_r(\mathcal{G}_{xx}) &= 1/\sqrt{\ell n_d}, \\
\varepsilon_r(\gamma_{xy}{}^2) &= \sqrt{2}\,\frac{(1-\gamma_{xy}{}^2(f_k))}{|\gamma_{xy}(f_k)|\,\sqrt{\ell n_d}} \\
\sigma(\Theta_{xy}) &= \sqrt{\text{variance of } \Theta_{xy}} = \arcsin\left\{\frac{(1-\gamma_{xy}{}^2(f_k))^{1/2}}{|\gamma_{xy}(f_k)|\sqrt{2\ell n_d}}\right\}.
\end{aligned} \tag{3.15}$$

The error decreases when the coherence approaches unity or the product ℓn_d increases.

3.5.2 Curve fitting

Numerical methods were used to fit theoretical functions with free parameters to experimental data sets throughout this work. The routine employed was the so-called non-linear recursive least-squares fitting (Bevington, 1969) and we will briefly describe its algorithm.

Let us define y_i as the experimental data points and the function $y(x_i)$ as the theoretical estimate of y_i at position x_i. The method of least squares consists of determining the values of the parameters a_j of the function $y(x)$ which yield a minimum for the function χ^2 given by:

$$\chi^2 = \sum_{i=1}^{N} \frac{1}{\sigma_i}(y_i - y(x_i))^2 \tag{3.16}$$

where σ_i are the variance associated with the experimental data points y_i and N the number of data points. The inclusion of the variance in the above equation weighs the importance given to the fit at each point according to the data's own variance. If the function is a reasonable approximation to the data, then its variance from the data, which is $(y_i - y(x))^2$, should be of the same order as the actual variance of the data. This means that the reduced χ_r^2 defined as $\chi^2/(\text{N-n})$ where n is the number of parameters in the function $y(x)$ should be around unity.

In the method adopted, initial guesses are made for the parameters of the function $y(x)$ and a χ^2 is calculated. The parameters are then incremented in such a fashion as to make χ^2 decrease. This process of varying the parameters is repeated until a minimum is found. Using this iterative method, the process of finding the minimum value of χ^2 can be repeated until the desired degree of accuracy is reached. The values of the variables from the last iteration then give the best fit of the data.

3.5.3 Analysis of FFS signal

The procedure for the creation and analysis of the envelope necessary to extract information about the fluctuation, is illustrated schematically in the block diagram of figure 3.9. The analysis can be divided into two parts, each one corresponding to one branch in figure 3.9.

The first part concerns the analysis of the DC-signal due to the Gaussian light beam. From a measurement of the conductance at each detector, we can infer the power falling onto it. A least square fit of the power obtained with a Gaussian function yields the three beam parameters: Waist (W), peak position (X_0) and peak power (A_0). With a knowledge of the first two parameters (W and X_0), the dimensionless variable $u = (x - X_0)/W$ which characterises the position of the detector, can be calculated. The peak power will also be needed to find the absolute level of fluctuations.

The second branch of the figure 3.9 relates more directly to the fluctuation signal and we will describe how to construct these profiles. For the intensity envelope, an auto-power spectrum of the fluctuating signal ($I_{ac}(x,t)$) is done for each one of the 12 detectors. The amplitude spectrum is then calculated by taking the square root of the power spectrum. From these spectra, 15 bands of frequency are selected to represent a succession of 15 different events. The envelope is then created by combining the amplitude of similar frequency band from each detector.

The construction of the phase profile is similar to the intensity one, but the phase spectrum rather than the auto-power spectrum is calculated. First, a reference detector is chosen where the signal is the strongest, usually around $u = \pm 1$. Then, a cross-power spectrum is calculated between the signals from each detector and the reference one. The relative phase difference ($\Theta_{xy}(\nu)$) between the detectors is finally extracted from the cross-power spectrum and combined to produce the phase profile for each frequency.

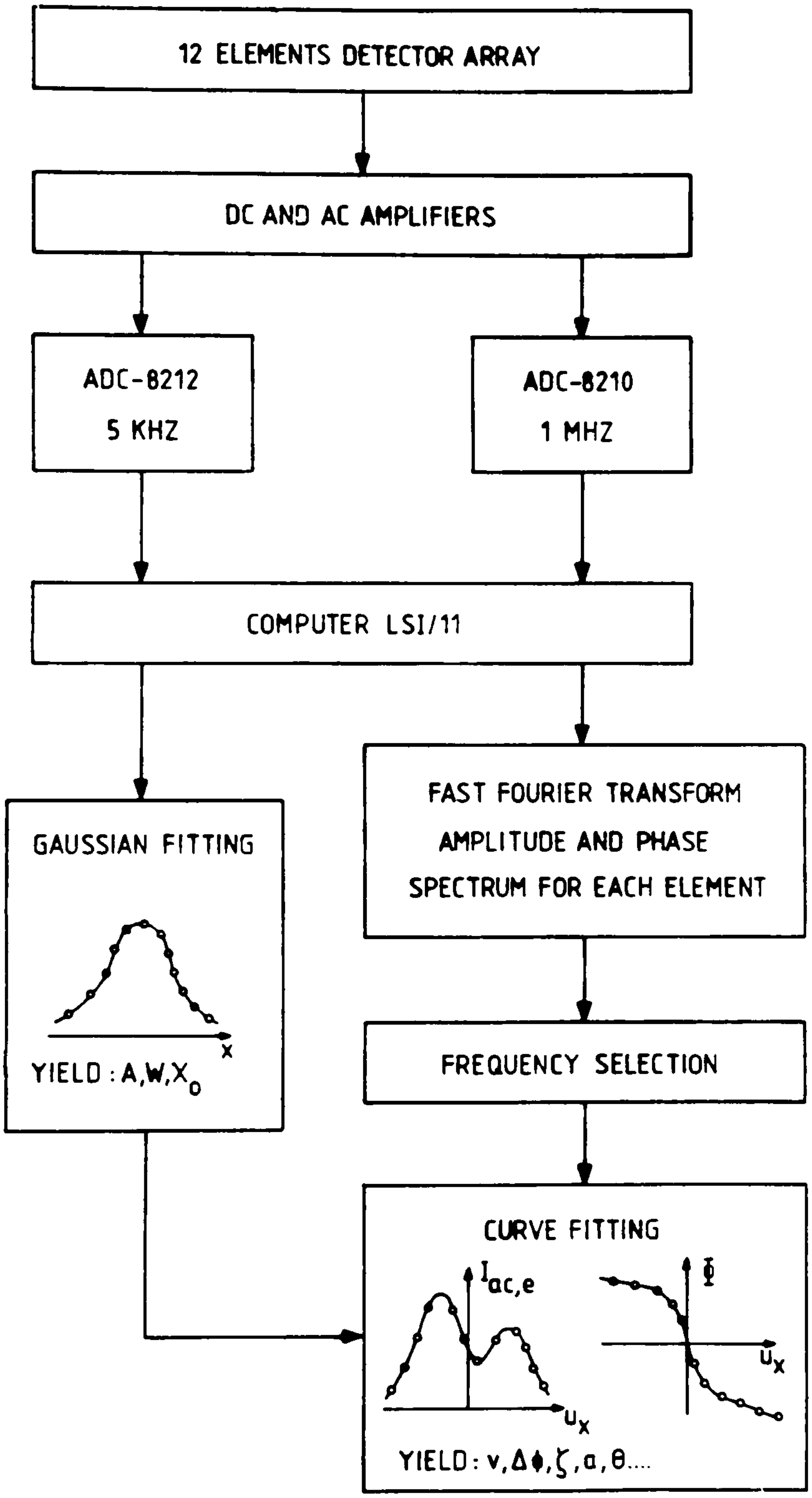

Figure 3.9: *Block diagram for data analysis.*

For the creation of the envelope in the plasma experiments, we used 3 plasma discharges(n_d) of 512 samples and the frequency bands were of 10 kHz(ℓ=5). The statistical errors were therefore reduced by a factor close to 4.

Once the envelopes for each frequency band are created with the dimensionless u as abscissa, we fit the experimental points using the theoretical function of the different models of Chapter II (single wave, damped wave, two waves...). In this analysis we are assuming that at each frequency only the event described by the model occurs and that no other perturbations exist.

3.6 Resolution of the fluctuation level

As in any experiment, it is desirable to know what level of fluctuations will yield a signal to noise ratio of one. The signal to noise ratio (SNR) at the signal processing stage after taking the auto-power spectrum, can be derived from equation 3.15 and is given by:

$$\frac{S}{N} = \frac{s}{s+1}\sqrt{\ell n_d} \tag{3.17}$$

where s it signal to noise ratio at the optical detector and the product ℓn_d was defined earlier. The last equation shows that the SNR of the system depends weakly on s when the latter exceeds one. The improvement of the SNR due to the averaging can be understood by rewriting the $\sqrt{\ell n_d}$ factor as

$$\sqrt{\ell n_d} = \sqrt{\left(\frac{\ell}{N\Delta t}\right)(n_d N\Delta t)} = \sqrt{BT} \tag{3.18}$$

where B represents the bandwidth resolution and T the total length in time of the signal (or integration time). This last form is reminiscent of the usual treatment of the SNR for a square law detector (see Cummins and Swinney, 1970) and in our analysis, the calculation of the auto-power spectrum performs the squaring. The averaging of the signal is usually carried out over 3 shots and 5 neighbouring frequencies.

In our experiment, the signal to noise ratio at the detector (s) is given by:

$$s = \frac{V_{signal}}{V_{noise}} = \frac{P_{ac}\ \alpha(V)\ A\ V_b}{V_{noise}} \tag{3.19}$$

where P_{ac} = Scattered signal power $\quad$ $\alpha(V_b)$ = responsivity of detector amplifier

V_{noise}= RMS noise voltage $\quad$ V_b = Bias voltage across detector

A = Trans-resistance gain of the amplifier $\approx 5 \times 10^6 V/A$.

The normal regime of operation of the detector is for a current of 1mA and a bias voltage of 10V. Using equation 3.2 and taking the average responsivity (30mS/W), we obtain a power onto the detector of 3mW(P_{dc}). The noise voltage is around 20mV^{rms} at these setting and is almost entirely produce by the shot noise at the detector. Then, the SNR at the detector is

$$s = 7.5 \times 10^7 P_{ac} \tag{3.20}$$

The power of the scattered signal (P_{ac}) can be expressed from the theory of Chapter II as:

$$P_{ac} = P_{dc}\Delta\phi f(u, v, \zeta \ldots) \tag{3.21}$$

where $f(u, v, \zeta)$ is a function depending on the model use for the fluctuation (usually around 0.5) and $\Delta\phi$ is the phase shift encountered by the beam.

By combining all the previous factors into equation 3.17 and 3.20, we obtain a SNR equal to unity for a phase shift of

$$\Delta\phi = 3 \times 10^{-6} rad.$$

The scattering by plasma fluctuations produce a phase shift [1] of $\Delta\phi = n_e r_e L \lambda_l$ and for L = 2cm, the minimum level of fluctuation is

$$\tilde{n}_{e,min} = 6 \times 10^{15} m^{-3}.$$

For a sonic wave in air, the phase shift is given by equation 4.2 and for L=1 cm, the minimum detectable level of pressure fluctuation is $\tilde{P}$ = 0.3 Pa .

[1] see section 2.3

3.7 Resolution in wavenumber

The resolution in K space (ΔK) for the traditional finite angle scattering is determined by the dimension of the scattering volume and can be written as (Holzhauer and Massig, 1978)

$$\Delta K \; W_o = \sqrt{2}.$$

A direct application of this formulae would not yield any resolution for a FFS experiment. Nevertheless, resolution can be improved beyond the usual diffraction limit by using *à priori* object information (Goodman, 1970). For the FFS, this information lies in the assumption that we are dealing with a pure sine wave in time (coherent). In the rest of the section, we will follow the argument put forward by Lukosz (1967) to analyse a system in which he used a moving grating, equivalent to a propagating wave, to obtain this spatial super resolution.

The fundamental invariant of an optical system is the number N of degrees of freedom of the wave field (or message) it can transmit. With coherent illumination and for a one dimensional system, N is given by:

$$N = (1 + T\Delta\nu)(1 + \Delta K W/\sqrt{2}) = \text{constant} \qquad (3.22)$$

where T is the observation time and $\Delta\nu$ the temporal bandwidth of the system. For N invariant (*i.e.* N=constant), the spatial bandwidth can be improved from ΔK to $\Delta\hat{K} < \Delta K$ by increasing its temporal bandwidth to $\Delta\hat{\nu} = \ell\Delta\nu$ and the observation time to $\hat{T} = n_d T$. As for any spectral analysis a better resolution is obtained by increasing either ℓ or n_d. Each temporal frequency must be separated by at least $\Delta\hat{\nu}$ and this condition limits the velocity of the wave(c) to values greater than $\Delta\hat{\nu} \cdot \Lambda$.

For these plasma experiments the product $\ell n_d = 15$ and the waist close to the fluctuations $W_o = 2.6$ mm^{-1}. The improved resolution is then by using the last equation(3.22):

$$\Delta\hat{K}_x = \frac{\Delta K}{\ell n_d} \simeq 0.3\mathrm{cm}^{-1} \qquad \text{for } c \geq 100m/sec. \tag{3.23}$$

The previous argument demonstrates the capability of our system to obtain higher resolution by assuming *à priori* information about the coherent nature of the wave in time (sin Ωt). In practice however, noise spoils the reconstruction of the envelope and reduces the resolution of the system to smaller values. The least squares routine which yields the different parameters of the function modelling the scattered light, also gives their standard deviation and we will use the latter to indicate the resolution for the dimensionless wavenumber v (KW_0).

Chapter 4

Experimental verification of FFS theory

The theory set up in chapter II has been partially verified using a single detector (Evans *et al.*,1982; Sonoda *et al.*, 1982) or an array of detectors (von Hellermann and Holzhauer, 1984). An attempt was made to duplicate the previous experiments to ascertain the operational range of our own FFS system and to complement them by studying the absolute level of fluctuation, broad K–spectrum effect, the scattering by two waves and an air jet and finally the reconstruction of $N_e(r,t)$ from the scattered intensity.

4.1 Single wave

The easiest way to test our system is with the help of ultrasonic waves generated transversely to the optical beam by a piezo-electric transducer (RS–307–351). These waves were emitted in pulses of limited duration (< 6 msec) so as to avoid any reflections from the surroundings. Figure 2.2 shows schematically the optical set up and in our notation the subscripts $_i$ and $_o$ referred to the image and object side of the lens.

Our first experimental test involved only monochromatic sound waves at 40 kHz (Λ= 8 mm). The variation in light intensity produced by the pressure fluctuations was detected by the array and analysed following the block diagram of figure 3.9. To include all the power of the scattered wave, we summed the signal over a narrow bandwidth of 2 kHz on either side of the mean frequency. The results and the fit of the experimental points with the single wave model are shown in figure 4.1 . Both intensity and phase profiles give good agreement with the theory and the value obtained for the wavenumber $K = v/W_0 = 0.76mm^{-1}$ and the position of the disturbance $\zeta = 0.9$, encompassed the expected value($K = 0.79mm^{-1}, \zeta = 0.8$). Sometimes the fitting of ζ does not yield the right value and we will devote the next section to this problem. The volume effect does not play any significant role for this test since $Q \leq 0.05$. Also by inverting the direction of propagation of the wave; the phase profile reverses in respect to the y axis. The new fitted value for v in this case is +.8 which represents the same wave, but with a negative K as expected.

All the previous features have been observed in the experiments already quoted, but none have conducted an absolute calibration of the signal. For this task, we employed a Bruel & Kjær sonometer (model 4135) to measure the level of pressure fluctuations at the center of the optical path. At these frequencies, diffraction of the sound wave by the microphone occurs and correction of the reading has to be made to obtain the free–field pressure. All pressure measurements were taken with the ultrasonic wave perpendicular to the diaphragm of the gridless microphone.

Knowledge of the variation of the pressure along the line of sight is needed to find the total fluctuation level. The measured sonic pressure profile is plotted in figure 4.2 and by deconvolving the measurement with the finite width of the microphone ($r = 3.5cm$), the following gaussian distribution is obtained:

$$\tilde{P}_{us}(z) = \tilde{P}_{us,o} \cdot \exp - \left(\frac{Z - Z_o}{w_{us}} \right)^2 \tag{4.1}$$

where $\tilde{P}_{us,o} = 1.06\tilde{P}_{mic}(z = 0)$ and $w_{us} = 10$ mm in this set up.

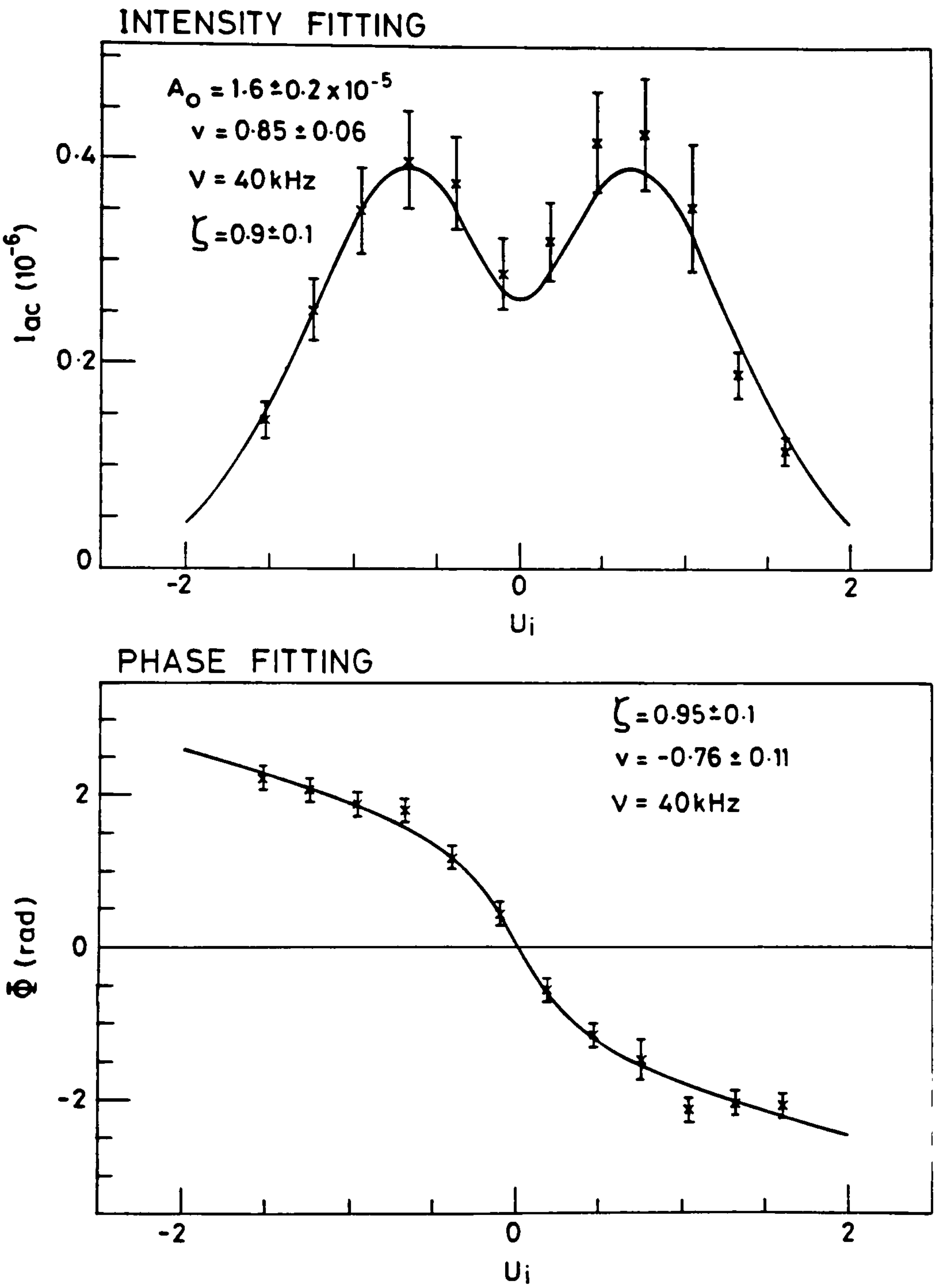

Figure 4.1: *Intensity and phase fitting for a single wave.*

The fluctuating phase shift incurred by the light beam will then be:

$$\tilde{\phi} = k_l \int_{-\infty}^{\infty} \tilde{\mu}(z)dz \tag{4.2}$$

where $\tilde{\mu}$ is the time varying refractive index. The latter is obtained from the Dale-Gladstone formulae (equation 2.9) and gives:

$$\tilde{\mu}(z) = \frac{(\mu_0 - 1)}{\gamma} \frac{\tilde{P}_{us}(z)}{P_a} \tag{4.3}$$

where $\gamma = \frac{5}{3}$ adiabatic constant , P_a= ambient pressure and μ_o=ambient refractive index for 10.6 μm. For our condition of pressure and temperature $(\mu_o - 1)$ is equal to 2.65×10^{-4} (Allen,1973).

By substituting equation 4.1 and 4.3 into equation 4.2 , we get a phase shift of $\Delta\phi_{son} = 2.9 \pm .3\ mrad.$ The outcome of the analysis of the scattered signal yields $A_o^{rms} = (1.6 \pm .2) \times 10^{-5}$. Knowing that the peak power of the laser beam is 63 ± 5 mW, the inferred phase shift is then:

$$\phi_{FFS} = \frac{A_0}{P_{pk}} = 2.5 \pm 0.5\ mrad. \tag{4.4}$$

The two values obtained for $\Delta\tilde{\phi}$ from the sonometer and the scattered signal agree within the experimental errors confirming the calibration (detectors and amplifiers) and the suitability of a FFS system to measure a phase varying object.

The linear response of this arrangement is exemplified by figure 4.3 where the intensity measured by one of the detector in the array is plotted versus the intensity measured by the sonometer. The two are directly proportional except at either end. For large ultrasonic intensity, the transducer saturates and creates harmonic of the fundamental which are not included in the FFS analysis of the signal but are measured by the microphone. For the lower end, ambient noise becomes non-negligible and adds to the microphone reading while absent in the narrow frequency band of the FFS signal. These artificial saturations due to the sonometer would be circumvented by filtering its signal in frequency around the bandwidth of interest.

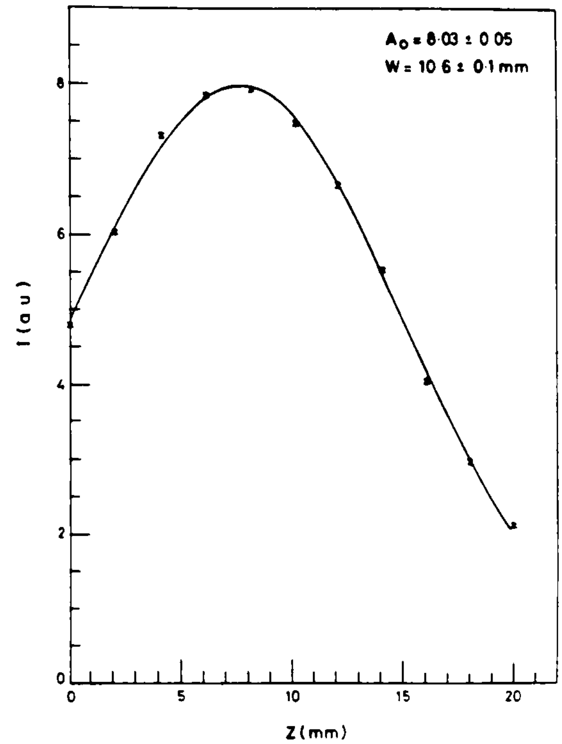

Figure 4.2: *Measured pressure profile of microphone.*

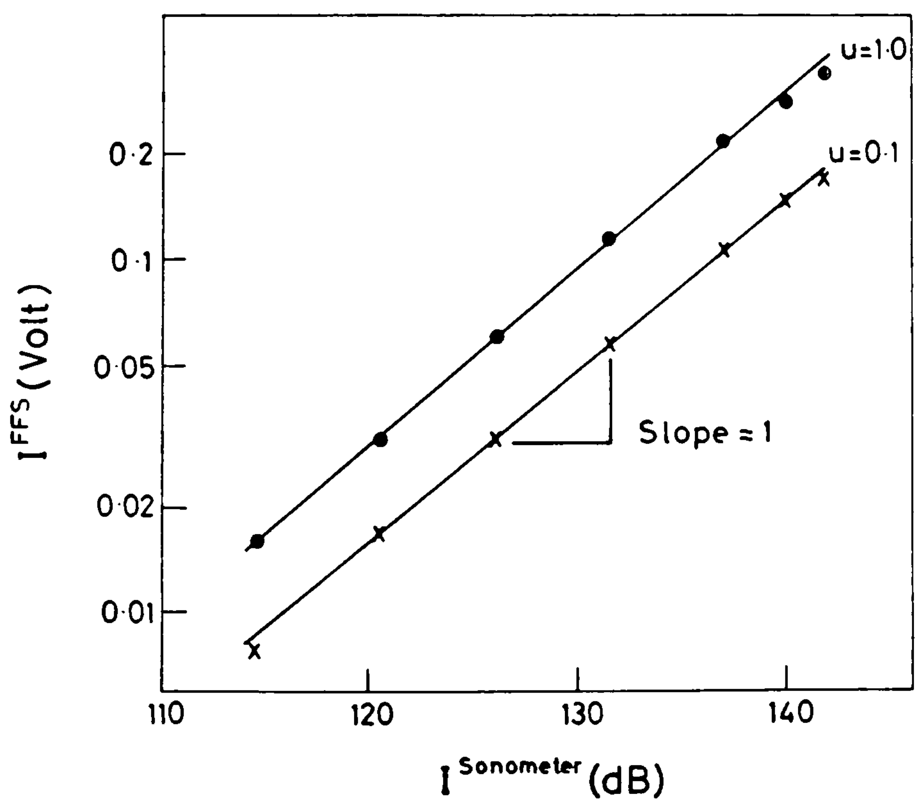

Figure 4.3: *Intensity of scattered signal versus sound wave pressure for two u positions.*

4.2 Comments on ζ fittings

As discussed earlier, fitting with ζ as the third free parameter tend to give unreliable results for ζ ranging from 0.5 to 1.5 instead of the expected 0.8 . This problem in fitting ζ was also encountered by von Hellermann *et al.*(1985) and we will describe a simple algorithm to circumvent it.

The principal reason in the inability of retrieving the right ζ lies in the dependency of the main parameters describing the shape of the profiles (R_1, S_o, S_∞) on ζ and v. Figure 4.4 shows curves of constant ratio (R_1) in function of ζ and v for the single wave case. At a given ratio R_1, ζ is roughly inversely proportional to v, and we would expect the two to interchange freely within the error bars during the fitting. As a consequence, a larger(smaller) fitted ζ would produce an underestimate(overestimate) of v and an overestimate(underestimate) of the amplitude A_o. The same dependency is also seen for the shape parameters S_o and S_∞ of the phase profile. Because of this interchangeability between ζ and v, it is preferable to fix ζ to the experimental value. In following this approach, we might lose in the generality of the technique, but the position of the source of disturbance is usually well known and its width usually represents less than 10% of the Raleigh zone (uncertainties in $\zeta < 0.1$). The fixing of ζ acts as a constraint on the fit to limit the possible range of v for a given ratio and allows a better interpretation of perturbations containing many waves.

The normalised position of the disturbance(ζ) vis-à-vis the beam waist W_o is estimated within 5–10% by the technique described in section 3–2 . Even with this good accuracy, one can ask what would be the effect of an incorrect choice of ζ on the fitting? To answer this question, a set of phase and intensity profiles were created for 12 different v (0.2 to 2.0) and only one ζ(0.3). These profiles were then fitted using the single wave model with two free parameters(v and a_o) at 5 different ζ(.2 to .4). The average ratio $\overline{(v_{fit}/v_{in})}$ was then calculated over the 12 v positions for each ζ. Figure 4.5 shows the average result of these 120 fits with the continuous

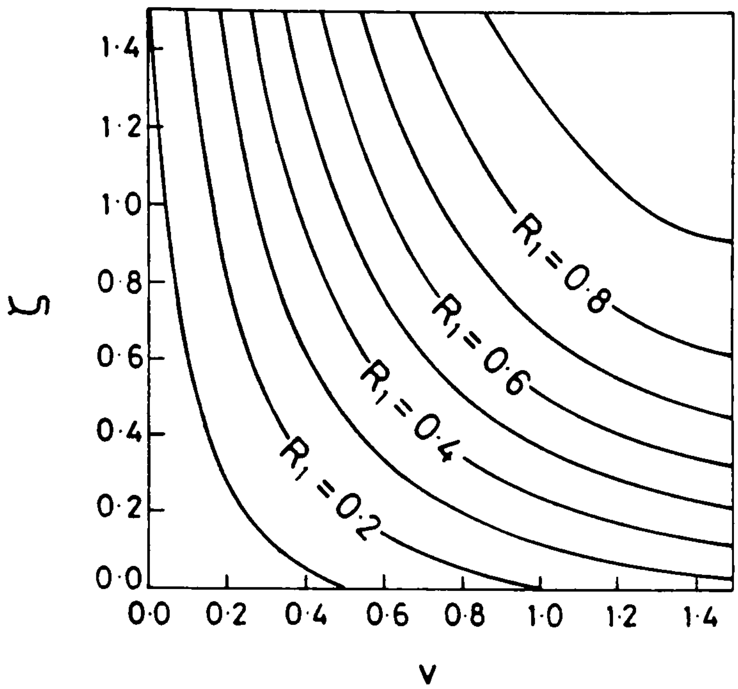

Figure 4.4: *Countour plot of constant R_1 in function of ζ and v.*

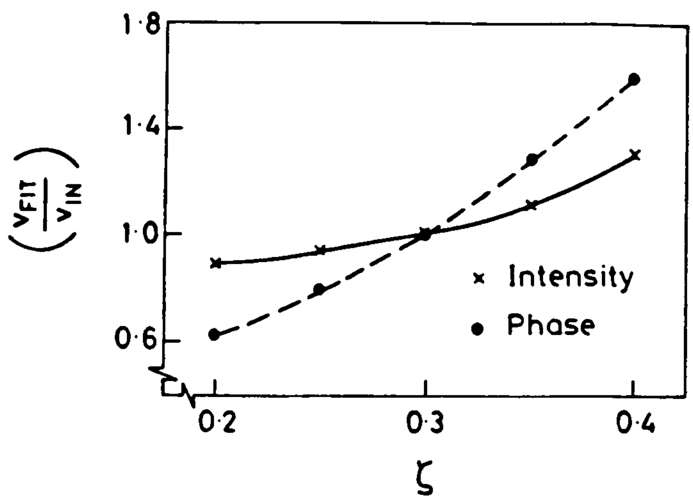

Figure 4.5: *Effect of ζ on $\overline{(v_{fit}/v_{in})}$for phase and intensity fitting.*

line representing the intensity profile and the broken one the phase profile. The fitting of the phase is more sensitive to changes in ζ and the crossing point of the two curves corresponds to the exact input ζ. Similar curves were produced for different ζ input which shows the generality of the results. From these arguments the following algorithm can be used to find the proper ζ :

1. Fitting of phase and intensity profile at one ζ
   - If $\overline{(v_{fit}/v_{in})}_{phase} < \overline{(v_{fit}/v_{in})}_{intensity} \Rightarrow$ reduce ζ
   - If $\overline{(v_{fit}/v_{in})}_{phase} > \overline{(v_{fit}/v_{in})}_{intensity} \Rightarrow$ increase ζ
2. Loop until negligible difference (< 2 %) between the two ratios of v

In practice, v_{in} is unknown but the ratio $\overline{(v_{fit}/v_{in})}$ can be replaced by the inverse of the fitted phase velocity(v_p^{-1}) as we will see in the next section.

4.3 White noise

Up to now only monochromatic sound waves have been investigated and a more realistic simulation of a real experiment should involve a spectrum of wave. This is achieved by feeding a wide band (4–54 kHz) ultrasonic transducer (MM:KSN-1005A) with a white noise generator (Bruel & Kjær, model 1405). As before, the signal lasts for 5 msec and we will observe the modulation it engenders onto the laser beam. In this case, the microphone was positioned 30 cm behind the optical path so that it could monitor the instantaneous pressure field without creating too much reverberations.

Groups of four consecutive shots were formed to reduce the statistical errors of the measurement (8000 points altogether). We divided the spectrum into 12 different frequencies from 15 kHz to 70kHz, each having a bandwidth of 1.5 kHz. After creating the phase and intensity profile at these frequencies, we fitted the

v_p $[m/sec]$	A	B	C	D	E
Intensity fitting	338±32	345±35	337±31	328±27	334±30
Phase fitting	334±29	341±26	330±24	333±27	338±26

Table 4.1: *Phase velocity obtained from phase and intensity fittings.*

envelopes with the single wave model using two free parameters (A_o and v) and varying ζ as explained in the previous section.

The outcome of the fitting for both profiles is displayed in figure 4.6 for one group of shots. The top two graphs shows the frequency (ν) versus the wavenumber (K) for the intensity and phase fitting respectively. The wavenumber is calculated by dividing the estimated v by the waist $W_o = 1.05 \pm .05$ mm of the laser beam in the object side of the lens. Both graphs exhibits strong linear dependency between the variables (ν and K). The best fitted line going through the origin and the experimental points is also drawn to characterise the linear relation. The slope of the fitted line gives the phase velocity(v_p) of the wave and table 4.1 lists the results for the 5 different groups.

Within the experimental errors, all the measured phase velocity agree with the sound velocity of $C_s \simeq 330$ m/sec. Before using the algorithm of section 4–2, the phase velocity from the phase fitting was systematically lower than the one from the intensity fitting(5-10.%). This was remedied by increasing ζ by 0.05 which corresponds to a change of 3 cm in the position of the disturbance. This is within the accuracy of the measurements of the beam waist and its position.

The third graph in figure 4.6 compares the estimated amplitude of the fluctuation (A_o) with the intensity spectrum measured with the microphone. The overall agreement is rather good with the exception of few points above 60 kHz. These

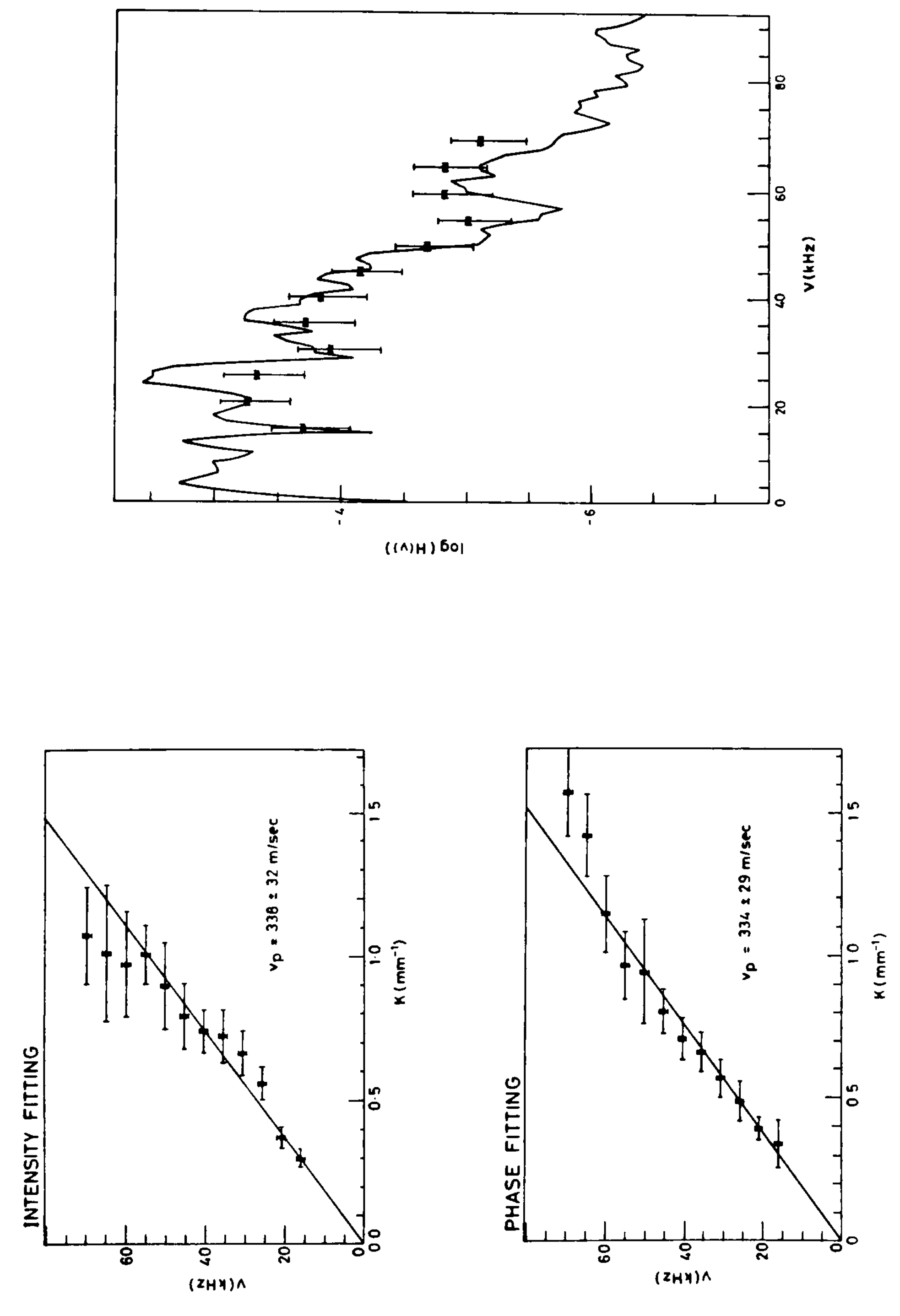

Figure 4.6: *ν–K diagram and amplitude spectrum for scattering by white noise.*

anomalies occur because the radiation pattern of the small speakers varies with frequencies making the measurement by the microphone at one point not fully representative of the total level of fluctuations.

4.4 Two waves effect

The purpose of this section is to complement the results of Sonoda *et al.*(1984) by investigating the phase profile as well as the intensity one for two propagating waves and to test the limits of our fitting program with this model.

The experimental set up consisted of 2 small piezo–electric transmitter placed at 24 cm ($\zeta = 0.2$) and 48 cm($\zeta = 0.8$) from the waist of the laser beam and emitting short pulses (5 msec) of sinusoidal signal at 40 kHz ($K = 0.74$ mm^{-1}). The phase between the two sonic beams was modified by translating one transducer with respect to the light beam and their amplitude ratio was adjusted with the balance control of an audio amplifier.

The experimental conditions were chosen so as to yield the most characteristic three–humps profiles of the two waves effect ($\theta \simeq 0^o$). Figure 4.7(a) illustrates such intensity profile as well as its phase profile. The fitting of the latter yields parameters in the neighbourhood of the experimental value ($v = .75, a \simeq 1.$). In contrast, the intensity profile does not give satisfactory results for v. This can be understood by the sensitivity of the fitting for low θ to small changes in the profile due to the calibration and/or noise. A theoretical curve for $v = 0.8$ has been drawn alongside the fitted intensity profile to demonstrate the small difference between the two.

For other experimental conditions ($|\theta| > \pi/4$), both fitted profiles concord with the theory as shown in figure 4.7(b). In that particular case, the transducer was displaced by 2 mm from the previous set up, which corresponds to a phase shift of 1.6 *rad* at this wavelength. The difference in the fitted θ for the phase profile between figures 4.7(a) and (b) is $1.9 \pm .4$ *rad* which is close to the expected value.

Only fitting with this model yields low chi-squared (χ^2) in these experiments when the trough of the intensity profile is shifted from the centre. The inability of the system to cater for low θ is not universal and we believe that with more detectors and a better calibration, the fitting of the intensity profile should give the right value of v.

4.5 Air jet

Sound waves produced by a white noise generator do not have the complete turbulent nature desired to test the merits of the FFS for its further application in plasmas. The fluctuation needed requires a broad spectrum in wavenumber (K) at each frequency. There exist many ways of creating turbulence in air, but a jet was employed due to its localised nature, large intensity and its capacity to generate high frequency by doppler shifts from the main jet.

The turbulent K–spectrum of an air jet can be divided into three regions (Hinze,1975):

- Production range at low–K which depends on the nozzle.
- Inertial range at intermediate K in which the energy is shifted upward towards higher wavenumbers without much production or dissipation taking place.
- Dissipation range at high K in which the energy put into the production range is finally destroyed.

The inertial range should be the preferred one because its energy spectrum does not depend on the physical construction of the nozzle and it obeys the Kolgomorov

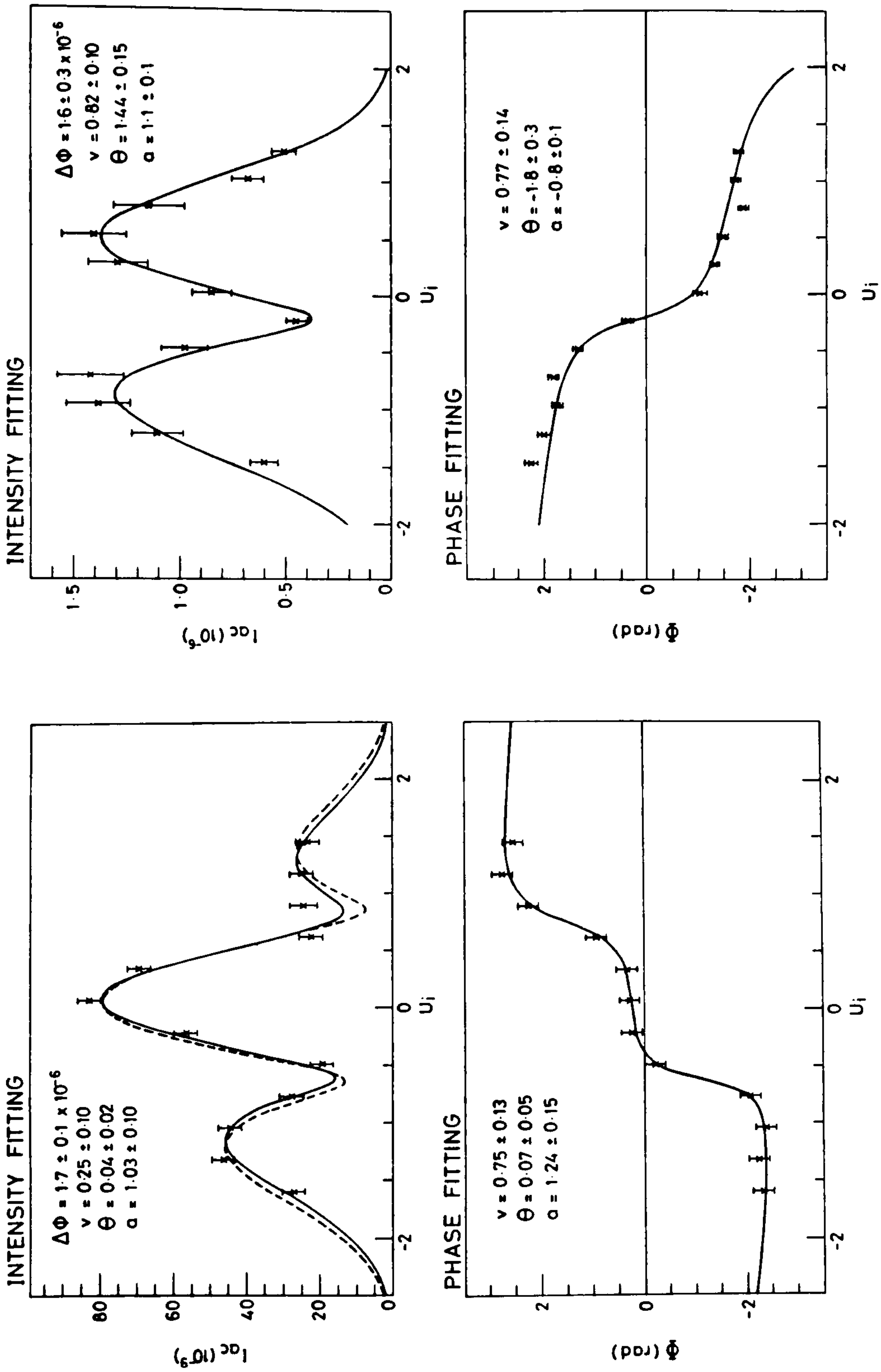

Figure 4.7: *Phase and intensity fittings for 2 waves: (a) $\theta \approx 0$ and (b) $\theta \approx \pi$.*

relation (Hinze,1975):

$$E(K) \propto K^{-5/3}$$

Unfortunately, the size of the eddies ($\propto 1/K$) in this range are much smaller than the size of the nozzle and the FFS technique is not conceived to cater for these long K. Finite angle scattering is better suited for this measurement as Stern and Gresillon(1983) demonstrated in their experiment. Nevertheless, fluctuations do occur at small K and the following will be a small study of them.

The free jet of Nitrogen(N_2) emerges from a circular nozzle of 2mm in diameter (d_n) into the stationary atmosphere. The pressure at the exit (P_1) is 2.8 bars which means that the axial velocity of the jet at the nozzle is (Davies,1972):

$$v_n \simeq C_s\sqrt{\frac{2}{\gamma}\ln\left(\frac{P_1}{P_0}\right)} \simeq 100 \text{ m/sec} \tag{4.5}$$

and the Reynold number is around 4×10^4.

In the first experiment the nozzle was oriented perpendicularly to the axis of the array which implies that the wave vectors observed (K) are normal to the air flow. The optical axis intercepts the axis of the jet and is placed 8cm away from the nozzle (d_n).

Results of the analysis from the intensity profiles of the scattered signal is shown in figure 4.8 by a plot of frequency versus the wave number(ν–K diagram). The latter is roughly constant ($2.7\pm.1$ mm) over the whole bandwidth. The scale length is comparable to the eddy mixing length defined as (Davies,1972)

$$\ell_e = 0.017 \cdot d_n \simeq 1.3 \text{ mm}$$

which corresponds to the peak in the wavenumber power spectrum. As expected, the FFS analysis selected the more energetic eddies from the spectrum. The phase profile does not give good fitting ($\chi^2 > 20$) due to the poor correlation of the signal across the array and for that reason we will not use its result.

The power spectrum of these fluctuations shown in figure 4.9 peaks around the

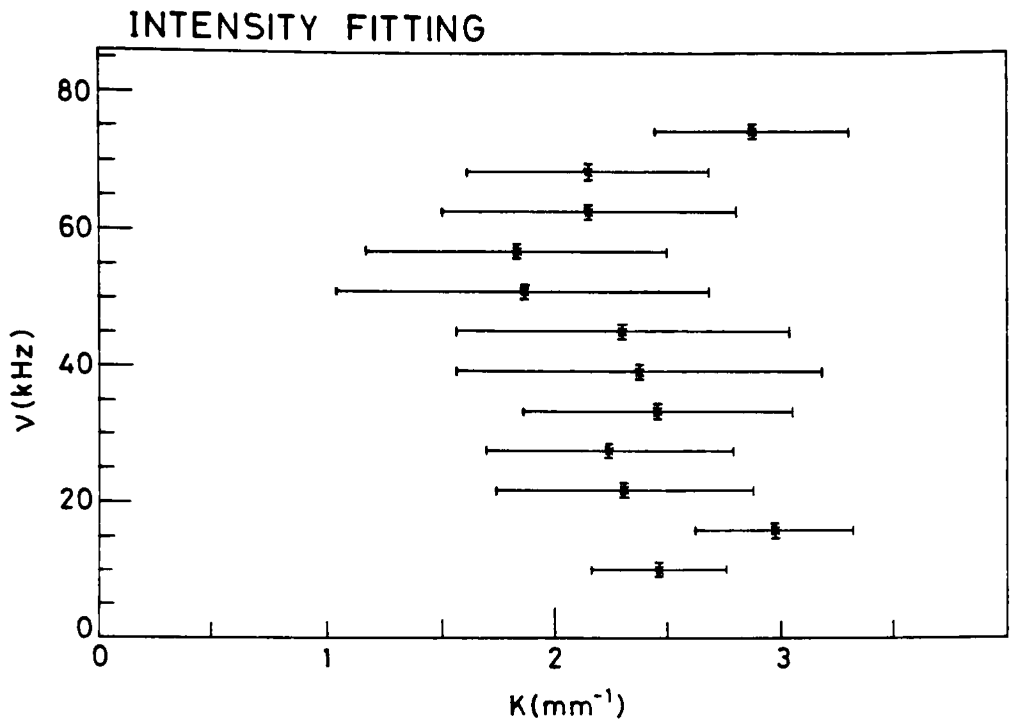

Figure 4.8: *ν–K diagram of intensity fitting for perpendicular air-jet.*

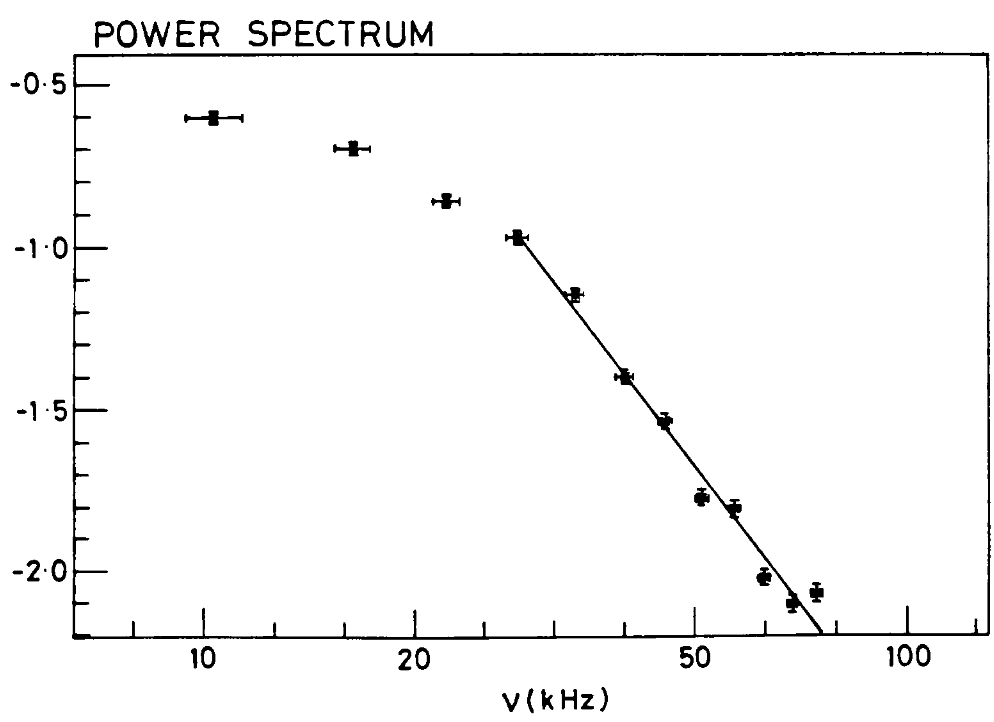

Figure 4.9: *Power spectrum for perpendicular air-jet.*

zero frequency and has a bandwidth at half height of around 6 kHz. By using the mean wave number of figure 4.8, we can interpret the spectrum as being caused by density fluctuations having phase velocity with zero mean and a standard deviation of 20 m/sec. These figures are typical of the fluctuation in speed of the main jet ($\lesssim$ 25% of the mean velocity $v_{axial} \sim 100$ m/sec).

In the second experiment the nozzle was oriented parallel to the axis of the array. This should produce signals doppler shifted by the velocity of the jet it encounters. The axial velocity of the fluid decreases with increasing distance (x) downstream from the nozzle according to (Davies,1972):

$$\bar{v}_x \simeq 6.4\frac{d_n}{x}\bar{v}_n \tag{4.6}$$

where d_n is the diameter of the nozzle. The distance between the nozzle and the laser beam (x) was varied from 6 to 10 cm.

The power spectrum of the scattered signal from one detector is shown in figure 4.10 when the air jet is switched on and off. All the power is concentrated in frequencies below 100 kHz which limits the scope of the studies to low K. Alterations of the amplification stage to reduce the power at these low frequencies has not been carried out because it would have involved too many changes from the original design.

Results of the analysis for 3 distances x and for a jet displaced laterally by 0.5 cm(y = 0.5) are listed in table 4–2. The dispersion curve for the first case in the table ($x = 6\ cm$) is plotted in figure 4.11 for the phase and intensity profile and clearly shows the linear relation between ν and K.

As in the white noise section, ζ had to be reduced by 5% so that the phase velocity inferred from both profile are similar. When the laser beam crosses the axis of the jet ($y = 0$), good agreement is obtained between the measured and expected value of the fluid velocity. The situation is not so satisfactory in the wings of the air jet ($y = .5$) where the measured phase velocity is beyond the error margins of the theoretical one. This could be explained by considering that the air

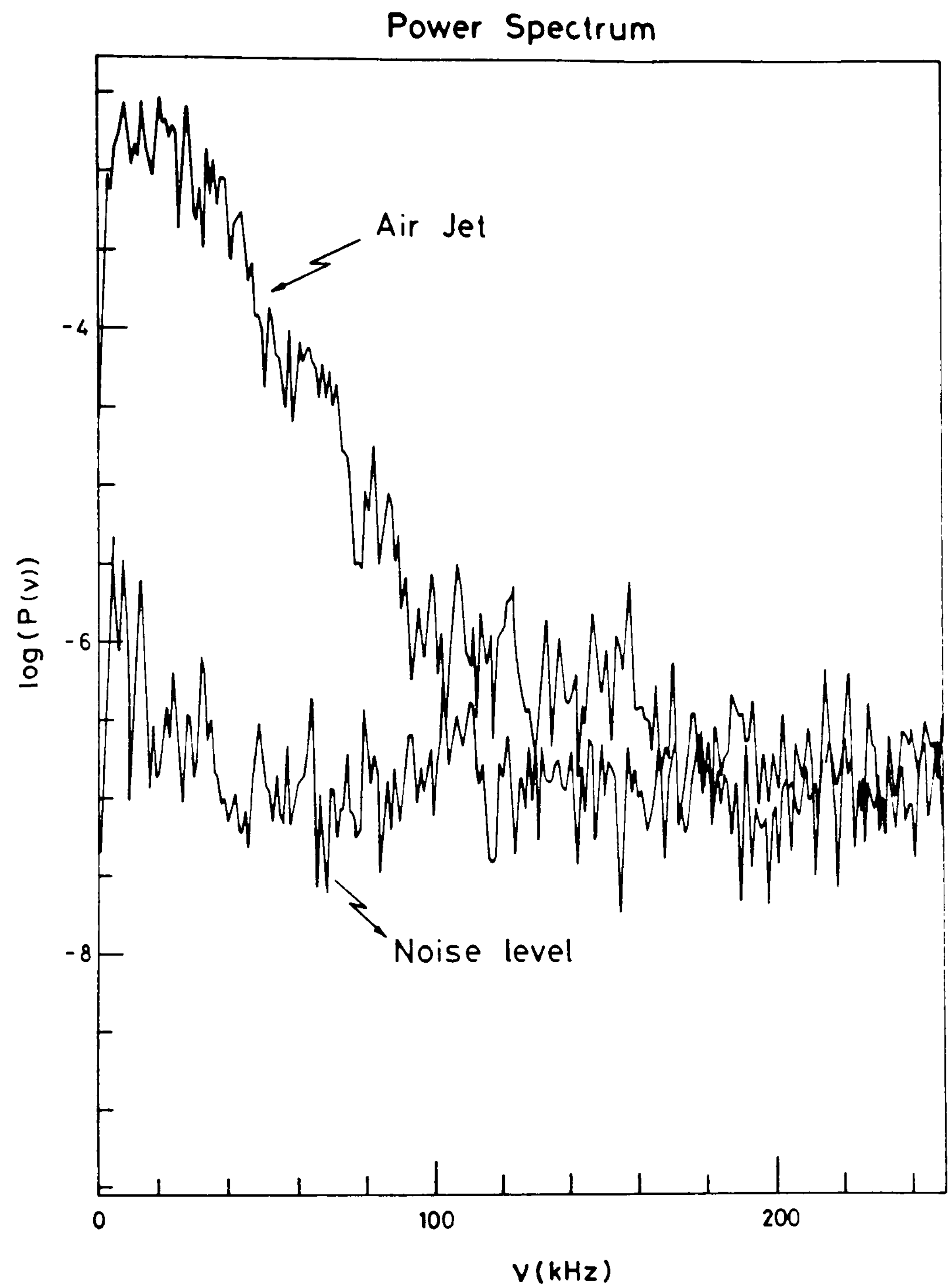

Figure 4.10: *Power spectrum for parallel air-jet.*

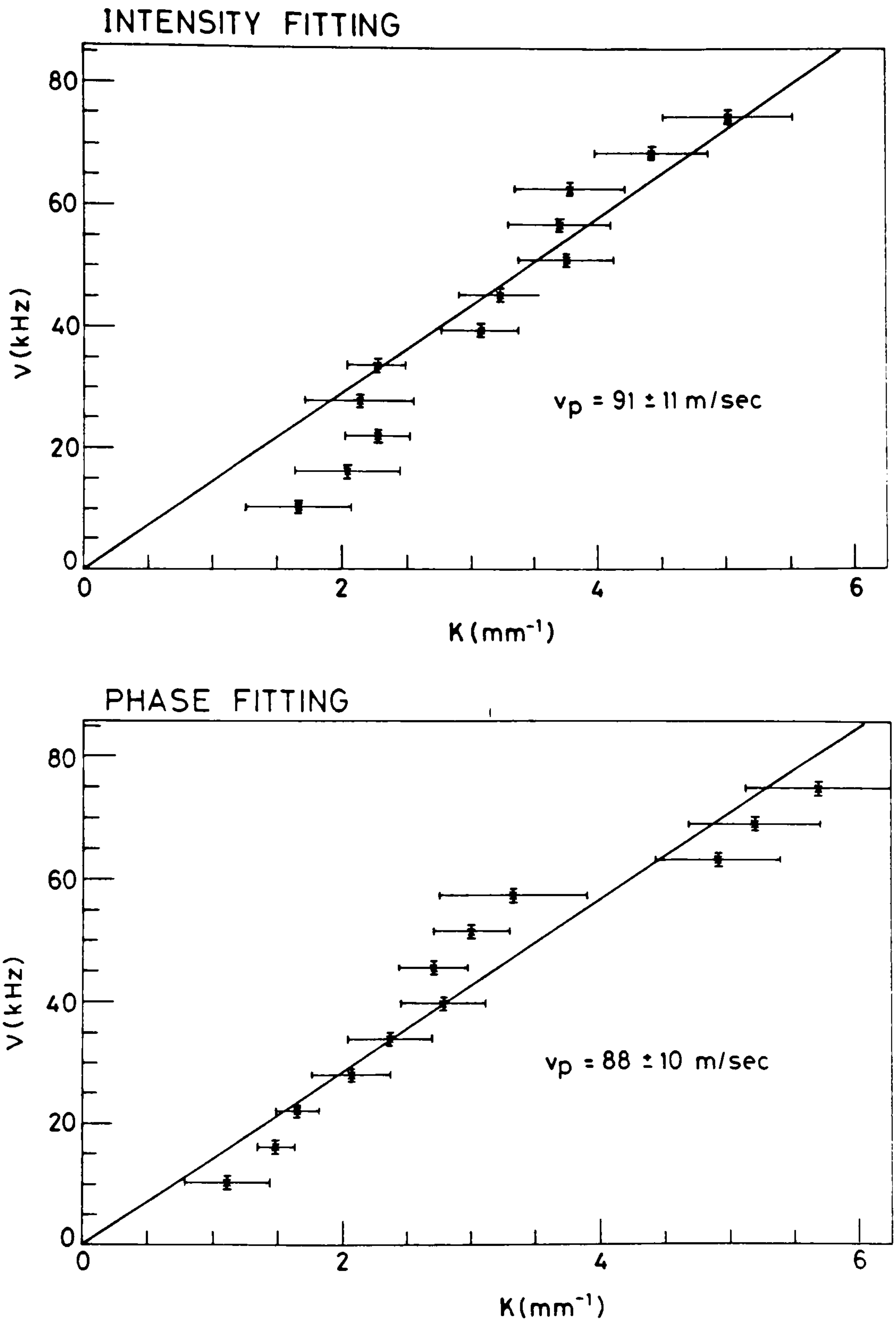

Figure 4.11: *ν–K diagram for parallel air-jet.*

x	y	v_p [m/sec]		
(cm)	(cm)	Int. Profile	Phase Profile	Expected
6	0	91±11	88±10	80±8
8	0	62± 8	62± 8	60±6
10	0	45± 7	42± 6	35±4
6	0.5	69± 9	68± 9	50±8

Table 4.2: *Theoretical and experimental phase velocity (v_p) for different positions of the air jet.*

jet has a velocity profile and that our measurements are not pin-point.

4.6 Comments on K saturation

As shown in the air jet section, the dispersion diagram ν–K exhibits saturations at small and large K. These might be real but their constant occurrence lead us to look for external effects to explain these anomalies. Two interesting mechanism which creates saturation were found and we will discuss them in this section.

The first one is an instrumental effect due to the uncertainties in the measurement of the waist at the detector plane. It affects the fitting via the dependant variable u. Simulations were carried out to detect what changes in the ν–Kdiagram are produced by an incorrect estimation of the waist (W_i). The algorithm was rather simple. One set of intensity and phase profile were created using the single wave model at 12 different v(0.2 to 2.0) and at ζ=0.8. Each profiles consisted of 12 points sampling the u space at regular intervals of $\Delta u = 0.3$. By multiplying the u-axis by a correction factor(UFAC) without altering the ordinate value at each u point(Intensity or phase), we were able to simulate changes in the waist. These modified profiles were then fitted in the usual way with the single wave model. The result of stretching(UFAC=1.05) and shrinking(UFAC=0.95) of the u axis is shown in figure 4.12 and we can immediately notice the changes in the ν–Kdiagram. The middle graph represents the results for the correct waist(UFAC=1.) which are in agreement with the input v of the simulation.

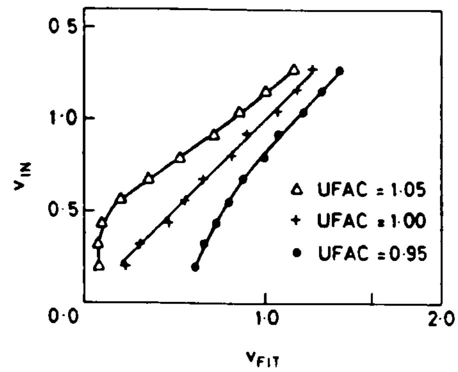

Figure 4.12: *Effect of changes of u_x on fitting.*

The other mechanism which creates saturation is related to the K-distribution at one frequency(ω) of the disturbance. Before considering its effect on the ν–Kdiagram, it is educative to ask what would be the fitted K obtained from an arbitrary distribution $S(K,\omega)$? Intuitively, K_{fit} should be an average of $S(K,\omega)$ depending on some instrumental function $\Im(K)$ and could be expressed by:

$$K_{fit} \approx \frac{\int_0^\infty K S(K,\omega)\Im(K)dK}{\int_0^\infty S(K,\omega)\Im(K)dK}. \tag{4.7}$$

The approximate sign indicates the heuristic nature of the last expression. The instrumental function has not been defined yet and we will try to find an estimate of $\Im$(K) for the single wave case.

For $v < 1$ and $\zeta \approx 1$, the peak of the intensity profile remains around $u_{pk} \cong 0.7$ and the ratio R_1 between the trough and the peak intensity increase in a linearly fashion with v. Addition of two waves of different v but equal phase would yield a profile which can be fitted by a weighted average of the two initial v. Because of the consistency of the peak position (u_{pk}), the weight here is the intensity of the peak position ($I_{env}(V)\mid_{u_{pk}}$) and this leads us to define:

$$\Im(v) = I_{env}(v)\mid_{u_{pk}} \tag{4.8}$$

For $v > 1$, the situation is not as clear because the shapes changes a great deal between different v ($u_{pk} \neq constant$). Nevertheless, $I_{env}(V)\mid_{u_{pk}}$ does still play an important role in the fitting and we will assume for convenience the same $\Im(K)$. Figure 2.5(b) shows the variation of the peak intensity(I_{env}) with v.

With this definition of the instrumental function, we can estimate what could be the K_{fit} for different K distribution. In the case of highly coherent waves, $S(K,\omega)$ can be described by delta functions ($\delta(K - K_o)$) and the result of the integrals in equation 4.7 would yield the right wavenumber K_o. For broad $S(K,\omega)$, the equation would distort K_{fit} by giving more weight to K which are closer to the condition $v \approx 1$. In this context, distortion means that the K_{fit} obtained at a given ω_1 is not equal to the peak value of $S(K,\omega_1)$

By using the ΔK model of section 2-9 , we could compare qualitatively the results of equation with the ones from the fitting of the profiles. The normalised wavenumber v will be used instead of K from now on . In a first step we evaluated equation 4.7 with the following $S(v,\omega)$

$$S(v,\omega) = \exp\frac{-(v-v_o)^2}{\Delta v^2}$$

at 10 different v_o(0.2 to 2.0) with $\Delta v = 0.05$ and 0.5 . The v_{fit} obtained in this fashion is plotted in figure 4.13 versus the input v_o as crosses. For small spectral width, v_{fit} and v_o are comparable, but at large Δv saturation occurs at small v_o.

In a second step, we created 10 intensity profiles using equation 2.34 and 2.24 for the ΔK model for the same set of v_o(0.2 to 2.0) and Δv. These profiles were then fitted using the single wave model and the results are plotted in figure 4.13 as circles. As before there is good agreements between v_{fit} and v_o for small Δv. For larger Δv, v_{fit} saturates at lower v_o but it yields the right v_{fit} at higher $v(> 1)$.

A comparison between v_{fit} obtained via the instrumental function and the fitting shows good qualitative agreement agreements for $v_o < 1$. By contrast, for $v_o > 1$ the fitting of the envelope is not affected by the Δv while the results from equation 4.7 shows the beginning of some saturation. These results will tend to reinforce the former discussion about the validity of $I_{env}(V)\mid_{u_{pk}}$ as the the instrumental function only for $v_o < 1$. The evaluation of the right instrumental function

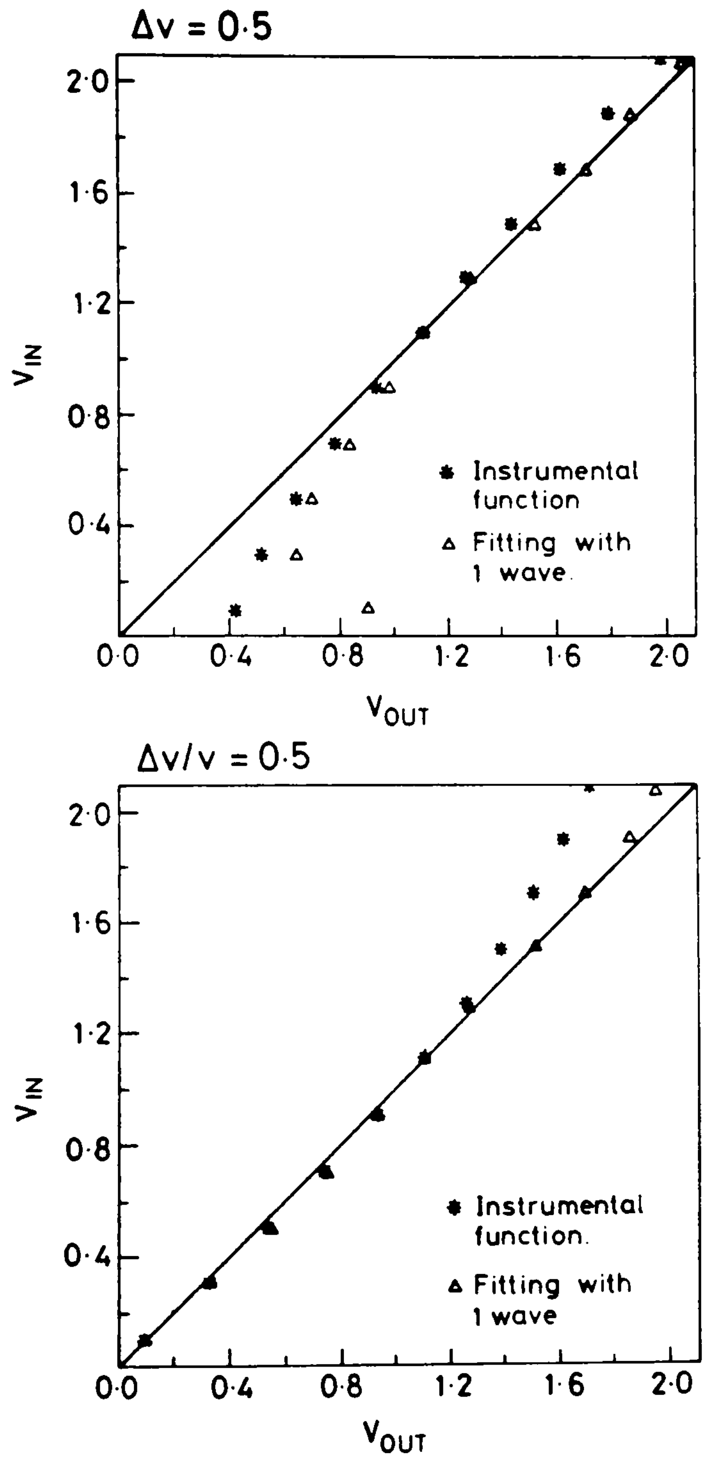

Figure 4.13: *Effect of* ΔK *on fittings.*

is beyond the limit of this work and could be of little use unless $S(K,\omega)$ is known in advance. However, K-saturation due to spectral width has been demonstrated for low v and could explain some results from the air jet.

4.7 ΔK effect

In this section, we will be concerned with the analysis of the ΔK model with theoretical and experimental signals. In a first step, profiles were constructed with the single wave model (section 2-5) and subsequently fitted with the ΔK model of section 2–9. The results of such process yielded the same dimensionless wavenumber (v) as the input with only negligible Δv ($\simeq 10^{-2}$). This test demonstrates that the ΔK model reduces to the single wave one for small spread in wavenumber. A similar analysis was carried out for the input profile calculated using the ΔK model at different Δv (0.2 and 0.5) and v (0.2 to 1.2). The results of the fitting did correspond with the theoretical values only when $\Delta v/v < 0.8$. This important condition represent the limit for which one wavelength is at least included in the width at e^{-1} height of the wave packet or equivalently, the limit at which we can still talk of waves in our analysis. Addition of Gaussian random noise at each of the 12 u positions did not alter the previous result. In summary, the ΔK model caters well for theoretical signals.

Experimentally, one possible way of simulating the effect of spread in wavenumbers is by grouping artificially in frequencies the scattered signal from acoustical white noise. Since there is a direct relationship between frequency and wavenumber, a given bandwidth in frequency (Δf) will produce a bandwidth in wavenumber ($\Delta K = 2\pi\ \Delta f/C_s$). To increase the similarity with our ΔK model, we will multiply each frequency in the chosen bandwidth ($\pm\Delta f$) by a gaussian weighting factor:

$$I(f_0) = \sum_{f=f_0-\Delta f}^{f_0+\Delta f} I(f)\exp - \left(\frac{f-f_0}{.75\Delta f}\right)^2 \tag{4.9}$$

Δf	$\Delta K_{th.}$	ΔK_{fit}	v_p
(kHz)	(cm^{-1})	(cm^{-1})	m/sec
0.5	0.1	0.1	360±30
1.5	0.3	0.3	342±30
4.0	0.8	0.2	385±40
8.0	1.6	0.2	390±45

Table 4.3: *Theoretical and experimental ΔK for different frequency bandwidths.*

where $I(f)$ is the intensity at one discrete frequency. The underlying assumption in the summation of intensity is that each frequency element are in phase as for the ΔK model.

This calculation is performed for each detector and the results are grouped to form the intensity and phase profile following the usual algorithm. The profiles are then analysed with the ΔK model of section 2–9. Table 4-3 lists the result of the ΔK analysis for one group of shots and for 4 different frequency bands. Only the results of the intensity profile fittings are given because the values obtained from the phase profile were too much inconsistent. Unfortunately, the fitted values of ΔK varied little in comparison with the changes in the bandwidth (Δf) and were always around negligible levels ($\Delta v \simeq 5\%$). The phase velocities(v_p) were for their part larger than the results of table 4–1.

The disagreement might be explained by an experimental phase spectrum which is different from the assumed one in the theory of the ΔK model.

4.8 Reconstruction of $N_e(r,t)$

The analysis of the scattered signal has so far always presupposed a knowledge of the fluctuation (*e.g.* sine wave, damped sine wave ...). A better approach would be to skip this stage and try to reconstruct the density fluctuation ($N_e(r,t)$) from the observed signal at the detector plane. This is analogous to the optical reconstruction of an image from an hologram but in this case optical detectors instead of photographic films are being used.

Before creating the computer code for the reconstruction of the signal, we designed one which accomplished numerically the calculation of the scattered field at the detector plane from the knowledge of the density perturbations(forward calculation). Apart from serving as test bed for the subroutines, this code will help in defining the limits for the parameters and the numerical link between the image and the object plane .

The optical geometry used in this code is identical to the ultrasonic experiment for which we wish to reconstruct the signal. This means that the detector plane is situated at the back focal plane of the lens (i.e. $D_2 = f$).

For a given density fluctuation ($\Delta\phi = \sin(Kx - \Omega t)$) as shown in figure 4.14(a), the code calculates the instantaneous fluctuating scattering intensity for each time by using

$$\tilde{I}_{ac} = jC\left[\mathcal{F}(\Delta\phi\, U_{go})^{*}\,\mathcal{F}(U_{go}) - \mathcal{F}(\Delta\phi\, U_{go})\,\mathcal{F}(U_{go})^{*}\right] \qquad (4.10)$$

where U_{go} is the gaussian light beam at the disturbance plane , $C = 1/(2\pi\sqrt{1+\zeta^2})$ and $\mathcal{F}()$ represents a one-dimensional Fourier transform. The last equation is derived from equation 2.15 by keeping only terms proportional to $\Delta\phi$. Higher order terms ($\Delta\phi^2$) are neglected because the phase shift induced by the waves in our experiments is small ($\Delta\phi \simeq 10^{-5}$). The result of such a calculation is shown in figure 4.14(b). This operation is carried out for 20 different times inside one full cycle of the fluctuation. At each image position, the code extracts the phase and the intensity of the scattered signal and creates the usual intensity and phase profile displayed in figure 4.15. The excellent agreement between the code and the theoretical curve signifies that the former reproduces well the theoretical calculation.

By multiplying the density fluctuation by $e^{-\alpha x}$ and re-running the code, we reproduced the expected profiles for the damping wave case as shown in figure

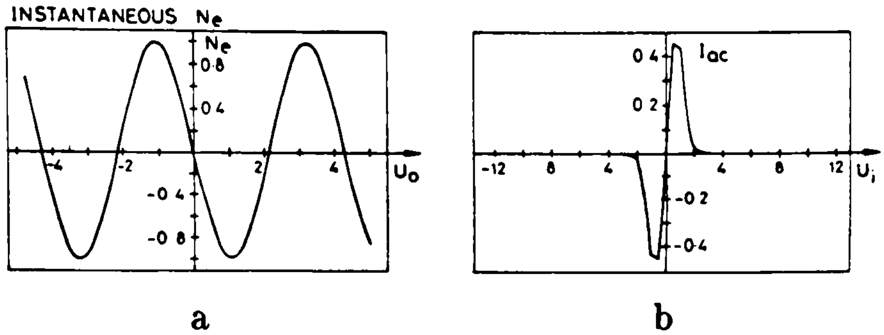

Figure 4.14: *Instantaneous density fluctuation(a), and scattered intensity(b).*

4.16. The simulation of the ΔK effect was also carried out by multiplying $\Delta\phi$ by $\exp -(K - K_0)^2/\Delta K$ and the result can be seen on figure 4.16. This code is versatile enough to check the results from most models of fluctuations in this simple geometry, as long as the signal is reproducible in time. The code could be expanded to cater for the more general geometry of section 2–4, by calculating equation 2.14 instead of equation 4.10 .

To carry out these forward calculations, we used a Discrete Fourier Transform(DFT) routine taken from the book "Programs for Digital Signal Processing" edited by the IEEE digital signal processing committee (1979). A Fast Fourier Transform (FFT) algorithm in this case is inefficient because of the small number of points used (12 to 100). For our DFT, the Nyquist sampling theorem states that for N samples separated by Δx_o in the object plane, the spatial frequency resolution $(\Delta\nu_i)$ in the image plane is given by:

$$\Delta\nu_i = \frac{\Delta x_i}{\lambda_l f} = \frac{1}{N\Delta x_o}$$

where λ_l is the wavelength of the radiation and f the focal length of the lens. This last equation can be rewritten using our dimensionless parameters as:

$$\Delta u_i = \frac{2\pi}{N\Delta u_o(1+\zeta^2)^{1/2}}$$

where Δu_i and Δu_o correspond to the separations between the sample in the image and object plane respectively.

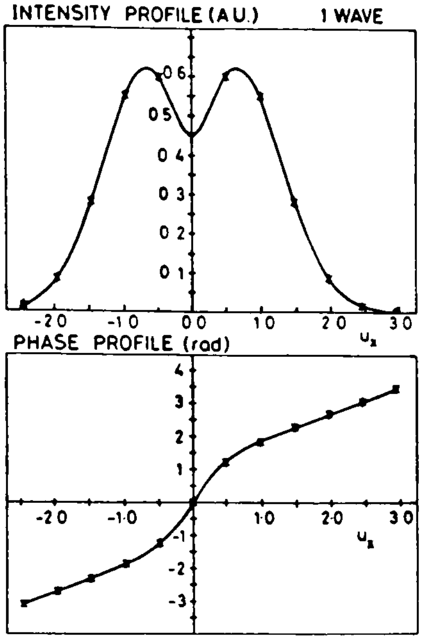

Figure 4.15: *Simulated intensity and phase profile for single wave model.*

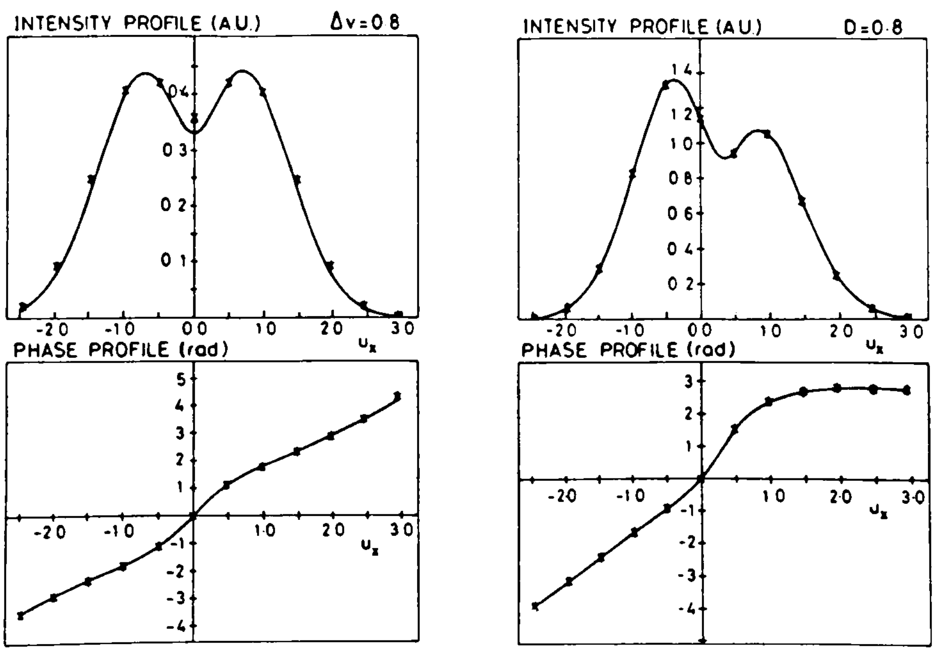

Figure 4.16: *Simulated intensity and phase profile for ΔK and damping model.*

The code yields the right profile as long as we resolve the two problems associated with DFT: discreteness and side lobe leakage. The discreteness problem occurs when the input signal is sampled with too large intervals. The sampling sequence does not represent the gaussian beam accurately enough and the output of the transform becomes deformed. The criterion used to avoid this problem is that the sum of the sampled signal be within 5% of the integral of the input signal. For the single wave case, the steps in the object plane need to be smaller than 1 ($\Delta u_o < 1$) to satisfy the criterion. The discreteness problem is more restrictive than the aliasing one for the interval length of the sampling sequence. To avoid aliasing, the spacing needs only to be smaller than $1/(2\Delta\nu_o^b)$ where $\Delta\nu_o^b$ is the spatial frequency bandwidth of the input signal.

The second problem, side lobe leakage, arises from the finite extent of the sequence of samples ($N\Delta u$). The window of samples should encompass most of the power of the signal ($\simeq$ 98%) and in our case due to the gaussian light beam in equation 4.10, this corresponds to $N\Delta u_o > 5$. The code always gave the good profiles for all values $v, \zeta, D, \Delta K$ ... as long as the previous conditions are met.

After having succeeded in doing the forward transformation, the reconstruction problem can be tackled. Doyle (1985,b) suggested a numerical iteration to reconstruct the fluctuating image from the scattered intensity for the simple geometrical layout without lens. Unfortunately as stated in his paper, the iteration is almost intractable because it involves convolution of vectors instead of single variables. We will re-express the problem for our particular situation and solve this inequality.

To simplify the notation in the expression of I_{ac}(equation 4.10), we will define

$$\tilde{I}_s = \mathcal{F}(\Delta\phi\ U_{go})\,\mathcal{F}(U_{go})^* = a + j\ b \tag{4.11}$$

where a and b are the real and imaginary part of I_s. By substituting I_s in equation 4.10, we obtain:

$$b = \frac{I_{ac}}{2C} \qquad \text{and} \qquad a \text{ is indeterminate}$$

Since our signals are always discrete, let us rewrite I_s in that form

$$I_s = \left(\Delta u_o \sum_{i=0}^{N-1} U_g(x_i)\Delta\phi(x_i)W_{ik}\right)\left(\Delta u_o \sum_{i=0}^{N-1} U_g(x_i)W_{ik}\right)^* = a(x_k) + j\ b(x_k) \quad (4.12)$$

where $W_{ik} \equiv e^{-j2\pi ik/N}$. In the last complex equation $a(x_k)$ and $\Delta\phi(x_i)$ are the unknowns and using the fact that $N_e(r,t)$ is real i.e. $\Im m(\Delta\phi) \equiv 0$, we have a closed set of equations. By taking the imaginary part of I_s, we obtain:

$$\Im m\left\{\tilde{U}^*_{g_k} \cdot \Delta u_o \sum_{i=0}^{N-1} U_g(x_i)W_{ik}\Delta\phi(x_i)\right\} = b(x_k) = \frac{I_{ac}}{2C} \quad (4.13)$$

where $\tilde{U}_{g_k}$ is defined as the discrete Fourier transform of U_{go} i.e. the terms inside the second parenthesis of equation 4.12. The latter equation which is written in indicial form can be rewritten as a matrix product

$$\Im m \begin{pmatrix} \tilde{U}^*_{g_1}U_{g_1}W_{11} & \tilde{U}^*_{g_1}U_{g_2}W_{12} & \dots & \tilde{U}^*_{g_1}U_{g_N}W_{1N} \\ \tilde{U}^*_{g_2}U_{g_1}W_{21} & \tilde{U}^*_{g_2}U_{g_2}W_{22} & \dots & \tilde{U}^*_{g_2}U_{g_N}W_{2N} \\ \vdots & \vdots & \ddots & \vdots \\ \tilde{U}^*_{g_N}U_{g_1}W_{N1} & \tilde{U}^*_{g_N}U_{g_2}W_{N2} & \dots & \tilde{U}^*_{g_N}U_{g_N}W_{NN} \end{pmatrix} \begin{pmatrix} \Delta\phi_1 \\ \Delta\phi_2 \\ \vdots \\ \Delta\phi_N \end{pmatrix} = \frac{1}{2C'} \begin{pmatrix} I_{ac_1} \\ I_{ac_2} \\ \vdots \\ I_{ac_N} \end{pmatrix} \quad (4.14)$$

where the imaginary part operator ($\Im m(\ )$) applies only to the square matrix ($\mathcal{M}$), $C' = C\Delta u_o$ and that the indices $_{i,k}$ refer to x_i and x_k respectively. The matrix form clearly shows that any point in the image plane is formed from a summation over all the object plane. All the elements of the matrix $\mathcal{M}$ are known and $\mathcal{M}$ acts as a linear operator which transforms the $\Delta\phi$ into the scattered intensity ($I_{ac}(x_k)$) at the image plane. To retrieve $\Delta\phi$, there is no need of numerical iteration but only to solve the set of linear equations represented by

$$\Delta\phi(x_i) = \mathcal{M}^{-1} \cdot \frac{I_{ac}(x_k)}{2C'} \quad (4.15)$$

where $\mathcal{M}^{-1}$ is the inverse of the matrix $\mathcal{M}$.

The above equation was implemented into a code using the NAG subroutine F04AEF (1986) to calculate the solution of the set of linear equations with Crout's factorisation. Before trying with experimental data, theoretical estimate of I_{ac} (equation 2.17) at a series of different times served as controlled input for the reconstruction program. Figure 4.17 shows in a 3–Dimensional plot the result of such a calculation for the particular case where v=1 and with 20 positions spaced by Δu_o=0.2 . The sinusoidal nature of the graph, its amplitude, temporal and spatial frequencies are as expected. This demonstrate the correctness of our software and theory in reproducing the fluctuating signal.

The running of this code caused a few problems. Firstly, the determinant of the matrix is rather small ($\sim 10^{-20}$) due to the rapidly decreasing gaussian beam and the singular values (σ_i) of the matrix varies from from around 1 (σ_1) to 10^{-11} (σ_n).For these large differences ($\frac{\sigma_1}{\sigma_n}$), the matrix $\mathcal{M}$ is said to be ill-conditioned for the calculation of its inversion. This means that for small changes of order ϵ in the matrix $\mathcal{M}$ or I_{ac}, relatively large changes($\propto \frac{\epsilon}{\sigma_n}$) in the solution of $\Delta\phi$ occurs for small σ_n (Golub and van Loan, 1982). To avoid these singularities,we truncated the extreme points of the reconstructed signal by keeping only a few around the centre of the beam (u=0.). The limit of truncation was usually set around $|u_o| = 2.5$.

Secondly, the finite extent of our signal (I_{ac}) induces a DC-level in the reconstruction of $\Delta\phi$. The removal of this shift was carried out by subtracting for each point the average of the selected set of points($|u_o| < 2.5$). This methods yields the correct answer for a large number of wavelengths, but introduces a bias at low frequencies when only a fraction of a wavelength is averaged over. This type of removal was chosen because it does not require any presupposed knowledge of the fluctuations.

The third problem is more inherent to the reconstruction technique and it limits its resolution. Unlike FFS which "averages" over a period of time to reduce the errors, in this case instantaneous values are taken and the resolution equation for the traditional finite angle scattering is valid(Holzhauer and Massig,1978):

$$\Delta K \; W = \sqrt{2} \tag{4.16}$$

Not withstanding the previous difficulties, we applied the code to the experimental data in the case of the scattering signal from ultrasonic waves at fixed frequencies. Prior to the reconstruction, the measured I_{ac} was fitted to a cubic-spline function with 4 knots placed at the extrema of the profiles. Subsequently, the spline function was evaluated at $u_i = i\Delta u_i$ for $-\frac{N}{2} < i < \frac{N}{2} - 1$, so as to correspond with the position of the discrete Fourier frequencies component. The 3–dimensonal plot of the reconstructed ultrasonic wave $(\Delta\phi)$ for the case of $\nu = 40$ kHz is shown in Figure 4.18. The standing wave patterns arise from the removal of the DC-level even though the wave is propagating. A comparison between the reconstructed structure and the expected one shows good agreement, but the lack of spatial resolution impedes further discussion. The agreement was also good at 60 kHz, but was rather poor at 20 and 30 kHz. The latter two frequencies are at the resolution limit of equation 4.16.

In this section, we demonstrated that it is possible to reconstruct the signal from the scattered signal for a FFS without any assumptions. Nevertheless, many constraints limits the scope of such reconstruction and it might be advantageous to use an optical reconstruction of the signal instead of the technique described. The phase contrast developed by Zernike(1935) and applied to tokamak plasmas by Weisen(1985) seems more appropriate to measure fluctuations in real time rather than the method suggested because of its better resolution(wider beam) and its optical imaging properties.

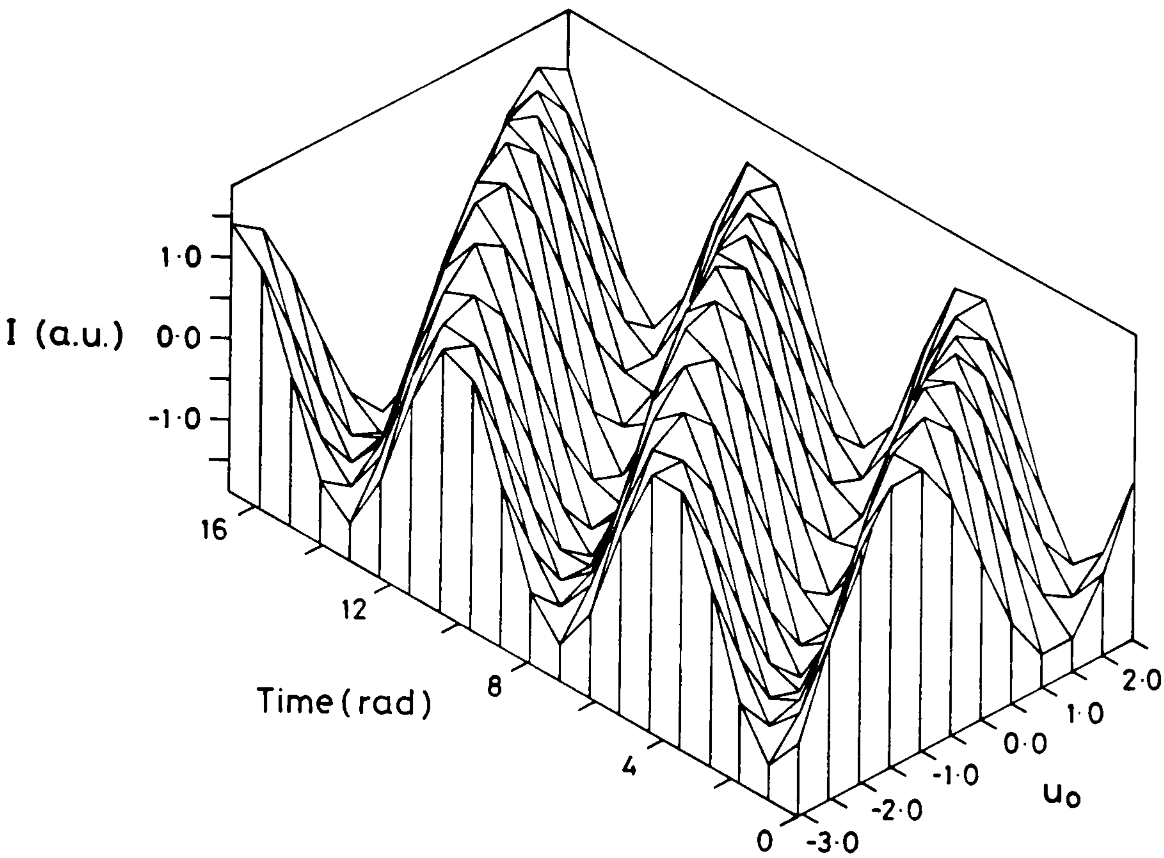

Figure 4.17: *3-D plot of the reconstruction for a theoretical wave.*

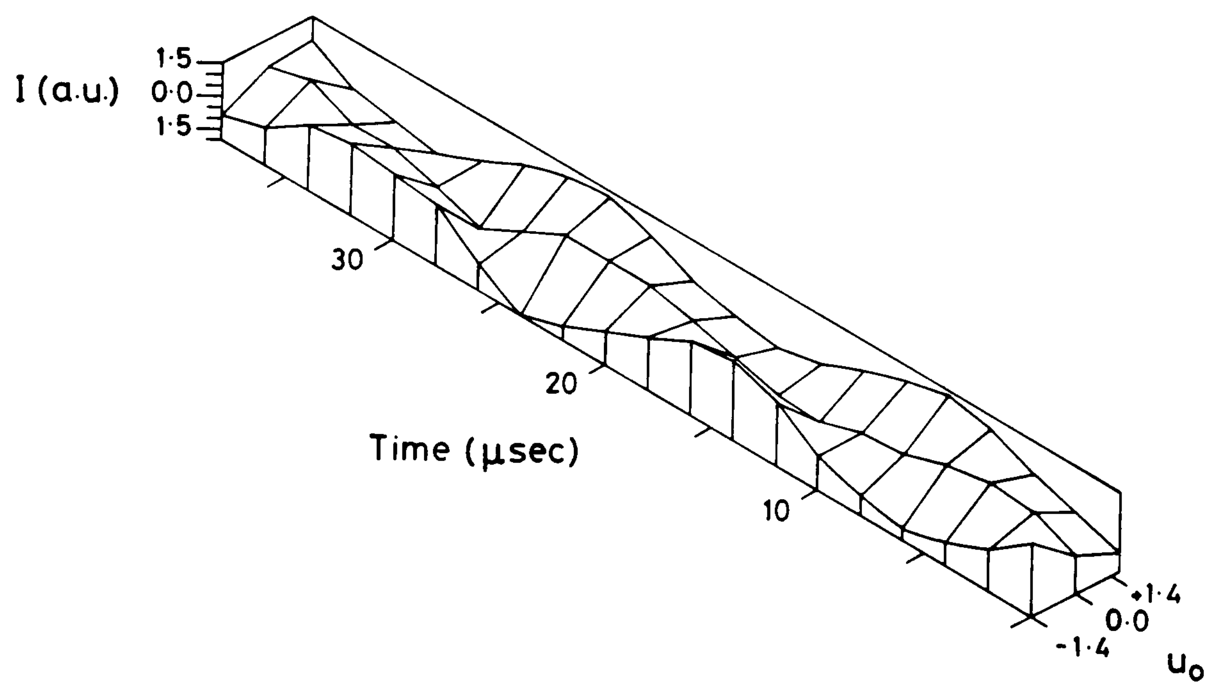

Figure 4.18: *3-D plot of the reconstruction of ultra-sonic wave.*

Chapter 5

The TOSCA tokamak

In this chapter the tokamak TOSCA and its main diagnostics are summarised. The results from the experiments carried out on TOSCA will be presented in the next chapter. A more general description of tokamaks can be found in Wesson(1987). There is also a brief account of the theory of turbulence and its effect on transport.

5.1 Machine description

TOSCA is a small air-core tokamak having a stainless vacuum vessel with major and minor radii of 30 cm and 10 cm respectively(King,1974). It has been designed to study the effects of minor cross-section shaping on plasma confinement and stability but this thesis is only concerned with the simple case of circular plasmas.

Fields are produced by coils outside the vessel which are connected to capacitor banks. Apart from the feedback vertical field which controls the horizontal position of the plasma, all the fields are preprogrammed and can only be varied between shots by changing the voltages and firing times of the individual capacitor banks. The plasma current pulse is power-supply limited to less than 6 msec with a flat top time of around 3 msec. A molybdenum rail limiter situated at 8 cm from the top time of around 3 msec. A molybdenum rail limiter situated at 8 cm from the minor axis of the vessel restricts the expansion of the plasma. The working gas for the experiments to be described was Hydrogen introduced via a piezoelectric valve. The density could be increased during a shot by gas puffing with a second valve.

Table 5-1 lists the main parameters of TOSCA measured using standard diagnostics which are described in the following subsections. Figure 5.1 shows examples of data taken for a typical discharge on TOSCA.

Major Radius	R	30 cm
Plasma minor Radius	a_l	8 cm
Plasma current	I_p	6–12 kA
Loop voltage	V_l	2–4 V
Magnetic field(Toroidal)	B_ϕ	0.5 T
Mean density	$\bar{n}_e$	0.4–2.$\times 10^{19}$ m^{-3}
Electron temperature on axis	$T_e(0)$	100–300 eV
Ion Temperature on axis	$T_i(0)$	30–80 eV
Confinement time	τ_E	0.2–0.6 msec

Table 5.1: TOSCA *parameters.*

5.1.1 Electromagnetic diagnostics

Many of the macroscopic properties of a tokamak plasma may be inferred from electrical measurements made external to the plasma boundary(Hutchinson,1987). The total current is measured with a Rogowski coil. This consists of a solenoid bent around the minor circumference of the vessel to form a loop. The transient plasma current generates a poloidal magnetic field which induces a voltage proportional to $\mathrm{d}I_p/\mathrm{d}t$. Passive or active integration of the output voltage from the loop yields I_p.

The loop voltage(V_l) is measured with a single wire placed toroidally around the machine. As well as the resistive voltage, inductive voltages may be generated

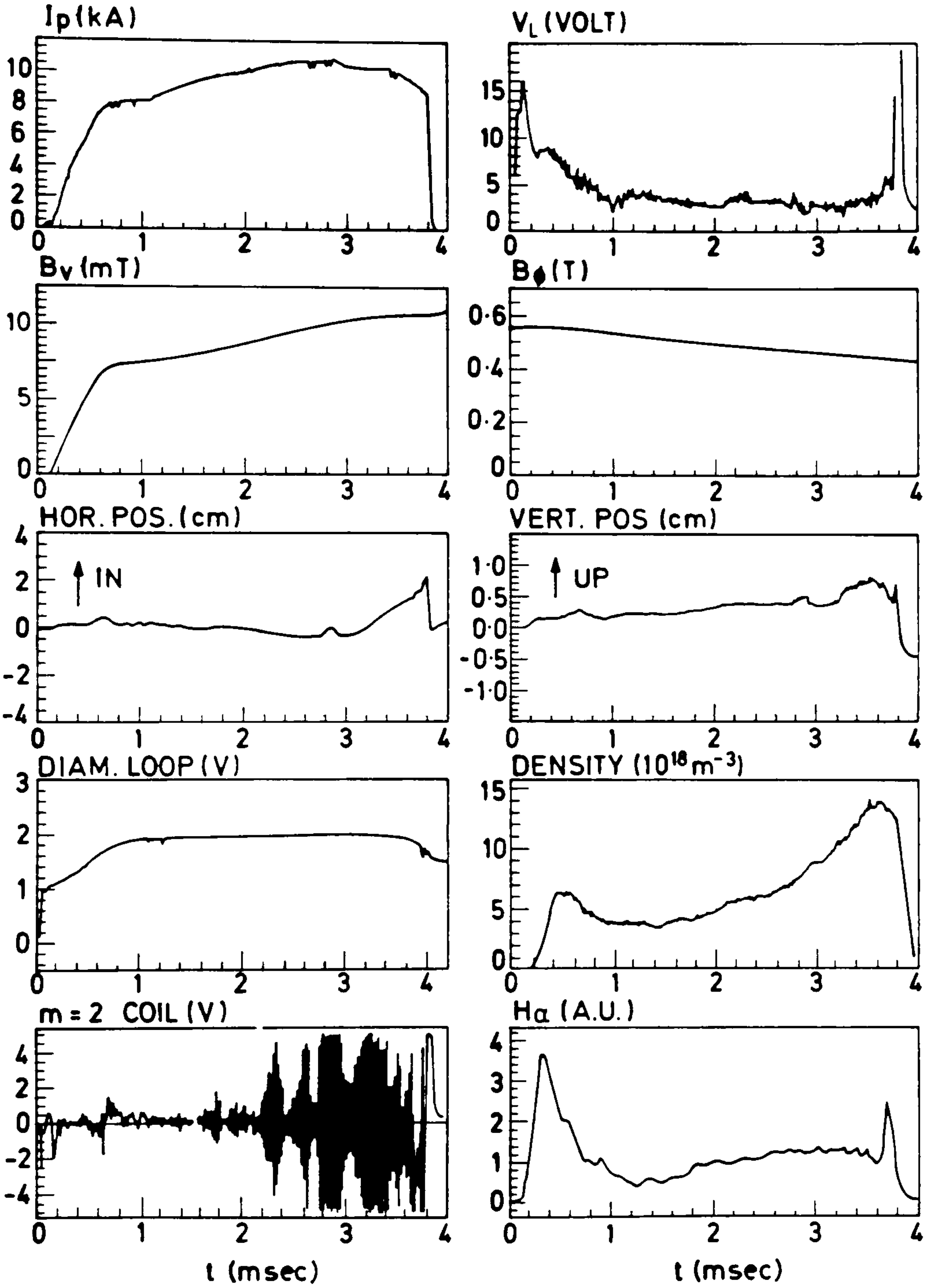

Figure 5.1: *Typical discharge parameters for* TOSCA.

by the transient discharge current and time-varying plasma inductance (Shafranov,1971) so that

$$V_l = R_p I_p + L\frac{\mathrm{d}I_p}{\mathrm{d}t} + I_p\frac{\mathrm{d}L}{\mathrm{d}t}$$

where L is the total plasma inductance, R_p the plasma resistance and I_p the plasma current. The plasma resistance depends on the plasma temperature and impurity concentration as demonstrated by Spitzer(1962).

The plasma position and MHD effects causing changes in the external field are studied with Rogowski type coils wound around the minor circumference having variable winding density proportional to the sine or cosine of the poloidal angle($\sin(m\theta)$). The integrated output of the $\cos(\theta)$ coils(m=1) is proportional to the displacement of the column while the output of the m=2 coil allow the study of low frequency magnetic oscillation (Mirnov) attributed to the m=2 tearing mode.

A diamagnetic loop wound around the minor cross section was used to measure the plasma pressure by detecting changes in magnetic flux($\Delta\Phi$) due to the plasma creation. It can be shown that (Braginskii,1959)

$$\Delta\Phi = \frac{(\mu_o I_p)^2}{8\pi B_\phi}(1-\beta_p)$$

where β_p is the poloidal beta defined by $\beta_p = \langle p \rangle / (B_\theta^2(a_l)/2\mu_o)$ and $\langle p \rangle$ is the average kinetic pressure over the plasma cross section. The change of the flux ($\Delta\Phi$) enclosed by the loop induces a voltage which is then time-integrated to yield β_p from the previous equation.

An alternative method for measuring β_p comes from the expression for the vertical field(B_v) necessary for equilibrium(Shafranov,1971):

$$B_v = \frac{\mu_o I_p}{4\pi R}\left[\ln(\frac{8R}{a_l}) + \frac{\ell_i}{2} + \beta_p - \frac{3}{2}\right]$$

A measurement of B_v, I_p, R and an estimate of the internal plasma inductance (ℓ_i) yields β_p. Both techniques have been used on TOSCA and gives similar results for steady conditions(Morris,1985). The energy confinement time τ_E can be estimated for the plateau phase of the discharge by calculating

$$\tau_E = \frac{\text{Plasma internal energy}}{\text{Rate of loss of energy}} \simeq \frac{\frac{3}{2}V <p>}{\text{Input power}}$$

where V is the plasma volume ($2\pi R \cdot \pi a_l{}^2$) and the input power is simply $V_l I_p$ for small plasma inductance. Many scaling laws have been produced to fit the experimental data and the Goldston low-density ohmic law(Goldston,1983) shows good agreement with the TOSCA results(Ellis,1984).

5.1.2 Interferometer

The plasma electron density n_e is determined by measuring the change in the refractive index caused by the presence of the electron gas[1] using a microwave fringe shift interferometer(Equipe TFR, 1978). The signal from a klystron(139 GHz) is frequency modulated by a sawtooth(200 kHz) and split into two beams one of which is directed through the vertical central chord of the torus while the second one goes along a reference path. The mixing of the beams after passing through the plasma onto the detector produces a signal phase shifted proportionally to the chord average density $\bar{n}_e$. Refraction is small over the range of densities on TOSCA if the discharge is reasonably centred. With only one chord available, a parabolic density profile was assumed which is typical for small tokamak. For the system installed on TOSCA, a phase shift of 2π or one fringe represents a line average density of 6.5×10^{18} m^{-3} for an interaction length of 16 cm.

5.1.3 Plasma emission diagnostic

No exhaustive survey of the radiation spectrum of the plasma was needed for this thesis and only two diagnostics were used to monitor the plasma condition.

The first one was composed of two photomultiplier tubes equipped with interference filters to select the H_α and O_{II} line radiation. A low level of impurity

[1] see section 2-3

radiation(O_{II}) indicated a clean plasma while H_α monitored mainly the neutral density at the edge.

The flux of soft X-rays due to bremsstrahlung radiation was detected by a pin-hole camera with an array of 8 surface barrier diodes designed by McGuire (1979). The flux increases strongly with electron temperature and to a lesser extent with density. Consequently, soft X-ray measurements are useful for monitoring the plasma core.

5.1.4 Langmuir probes

These probes are small electrodes inserted in the cooler edge of the plasma to measure its density, temperature and potential. A 4-pin probe having as electrodes platinum balls (spherical probe) of 1.1 mm in diameter placed at each corner of a square of side 3 mm, was positioned at the last closed magnetic surface ($r = a_l = 8cm$). The probe, amplifiers and part of the software were designed by A. Howling(1985).

For comparison with the FFS result only fluctuating quantities are of interest and measurements in at least two positions are required to infer statistical dispersion. Since the saturation current(i_{sat}) can be measured only at a single point for hardware reasons, the probes were left unbiased to measure the floating potential(V_f). Two pins of the probe were oriented parallel to the direction of the local magnetic field (within $\pm 10°$) while the other ones were displaced poloidally by 3mm. The floating potential of each pin was isolated from all others by an optical link (1 Hz–500 kHz) to avoid any ground loop interference.

The floating potential of a probe is determined by making the electron and ion currents falling onto it equal (Swift and Schwar, 1970). For weak magnetic field and with ion temperature much lower than the electron temperature, the floating potential is given by:

$$V_f = V_p - \frac{T_e}{2e} \ln\left(\frac{M_i}{2\pi m_e}\right) \tag{5.1}$$

The effect of the magnetic field has been ignored in most tokamak measurement because the turbulence breaks up ion orbits(Robinson and Rusbridge,1969) and the same assumption will be used. Howling(1985) calculated for the edge plasma in TOSCA that

$$V_f = V_p - \alpha T_e \quad \text{where} \quad \alpha = 2.3 \pm 0.2 \ .$$

He used a more sophisticated theory developed by Stangeby(1984) which accounts for non-zero ion temperature and secondary emission from the probe due to electron bombardment.

Fluctuations of the floating potential($\tilde{V}_f$) can then originate from either temperature fluctuation($\tilde{T}_e$) or plasma potential fluctuation ($\tilde{V}_p$). The former was found experimentally to be negligible (Howling, 1985) for frequencies above the MHD modes and we will therefore interpret the signal from the fluctuating potential as being plasma potential fluctuation($\tilde{V}_f = \tilde{V}_p$).

The statistical dispersion relation of the potential fluctuation was calculated using the method of Beall *et al.*(1982). To determine it, one monitors the fluctuations at two points spaced by a distance Δx. The temporal phase shift between the two points(Θ_{xy}) which can be calculated using the cross power[2] is related to the local wavenumber and its average over a sequence of shots yields the dispersion:

$$\overline{K}(\omega) = \left\langle \frac{\Theta_{xy}(\omega)}{\Delta x} \right\rangle$$

The underlying assumption in this approach is that the fluctuations in a plasma can be described by a linear superposition of waves each being characterised by a relationship $K = K(\omega)$. This calculation is valid if the wavenumber changes are small over one wavelength and if $K_{max} < \pi/\Delta x$ (Beall *et al.*,1986).

The estimate of the wavenumber spectral width($\sigma(\omega)$) is given by (Beall *et*

[2]see section 3-6

al.,1982):

$$\sigma(\omega) = \frac{\sqrt{2(1-\gamma^2}}{\Delta x} \tag{5.2}$$

where γ is the coherence between the two probes signal. It can be viewed as a measure of the turbulent broadening of the dispersion relation.

Also, an estimate of the growth rate of the fluctuation can be calculated by statistical analysis. For Gaussian input signal, the growth rate($\gamma(\omega)$) is given by (Ritz *et al.*,1988)

$$\gamma(\omega) = \frac{1}{\Delta x}\left(\frac{|\mathcal{G}_{xy}|}{\mathcal{G}_{xx}} - 1\right) \tag{5.3}$$

where $\mathcal{G}_{xx}$ and $\mathcal{G}_{xy}$ are the auto and cross power spectrum of the time series. This equation ignores nonlinearity of the input signal and yields a gross estimate. For negative values of $\gamma(\omega)$, the wave is damped and the correlation length can be approximated by $L_c \propto 1/\gamma(\omega)$.

5.1.5 Far forward scattering

Most of the relevant information about the FFS system has been discussed in Chapter III and we will limit ourself to discuss the details of the experiment on TOSCA. Figure 5.2 shows a schematic of the set up as installed on TOSCA. A cylindrical lens(L_3) was included just before the detector to select the wave direction(see Appendix B).

The optical path for the FFS was in the same poloidal plane as the side limiter and displaced toroidally by around 90° from the Langmuir probe. The ports were also used to refill the tokamak with neutral gas. The influx of gas did not directly influenced the scattering signal since a high pass frequency filter(30 kHz) eliminated all of the sonic frequency range.

The main problem encountered in the phase fitting was due to the unavailability at the time of the experiment of a master clock module. Instead, each ADC had its own internal clock, and each was triggered by a common signal. This introduced

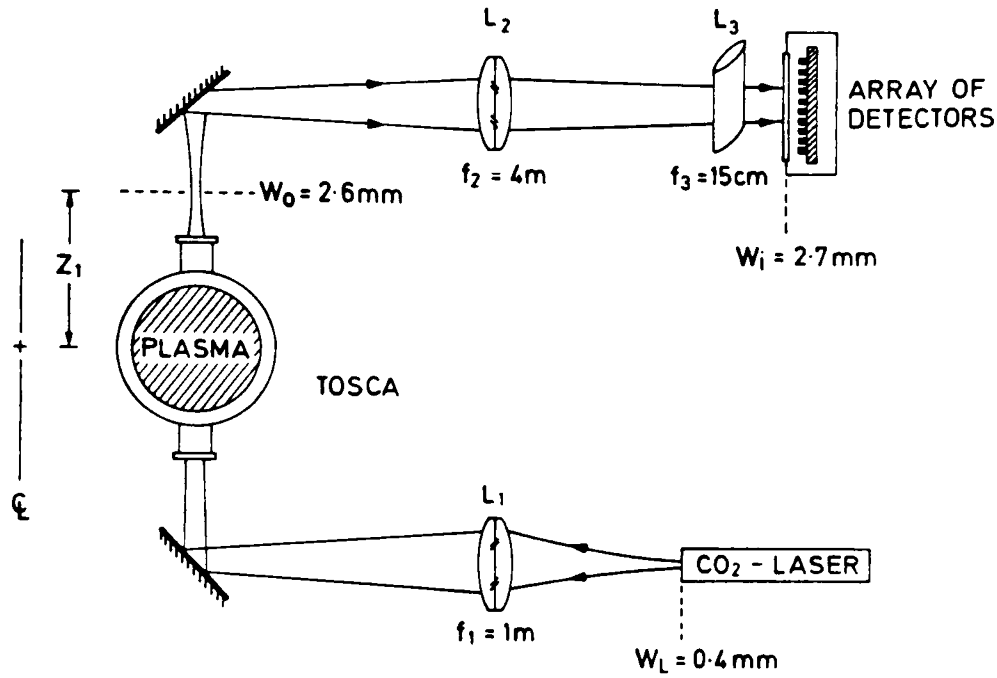

Figure 5.2: *Optical layout for FFS system on* TOSCA.

a time delay smaller than the sampling rate ($1\mu sec$) and produced random phase jumps between ADCs which are dependent of the frequency.

Figure 5.3 shows a typical phase profile for a plasma shot with jumps. A program was written to eliminate these jumps by fitting lines on the 4 points of each ADC outside the center (ADC-1,ADC-3). Then, the difference was calculated between the phase of the neighbouring point of the middle ADC(2) and the extrapolated value from the line at the same position (shown as a cross) at each frequency. Finally, a linear fit of the phase difference versus the frequency was carried out to find the delay from the slope as shown in figure 5.4. By applying these corrections to the two extreme ADCs(1 and 3), the phase profile appears correct. In this treatment, we assumed that the phase varied linearly around the transition point and this might not always be true. By over-compensating for the phase jump, the fitted value of v would be smaller than the expected one.

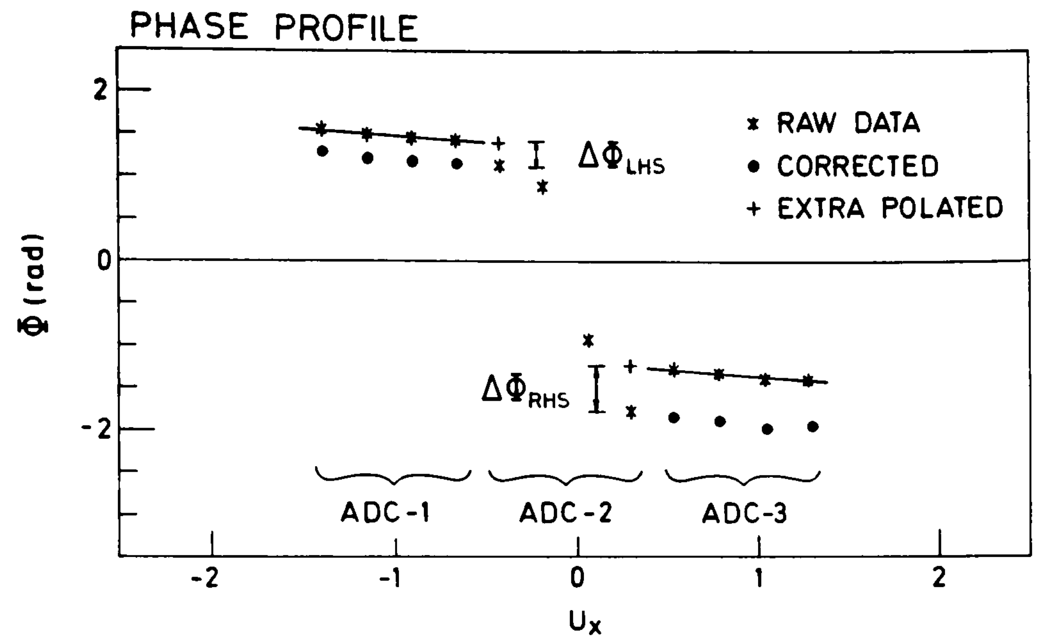

Figure 5.3: *Correction of phase profile to account for lack of synchronisation.*

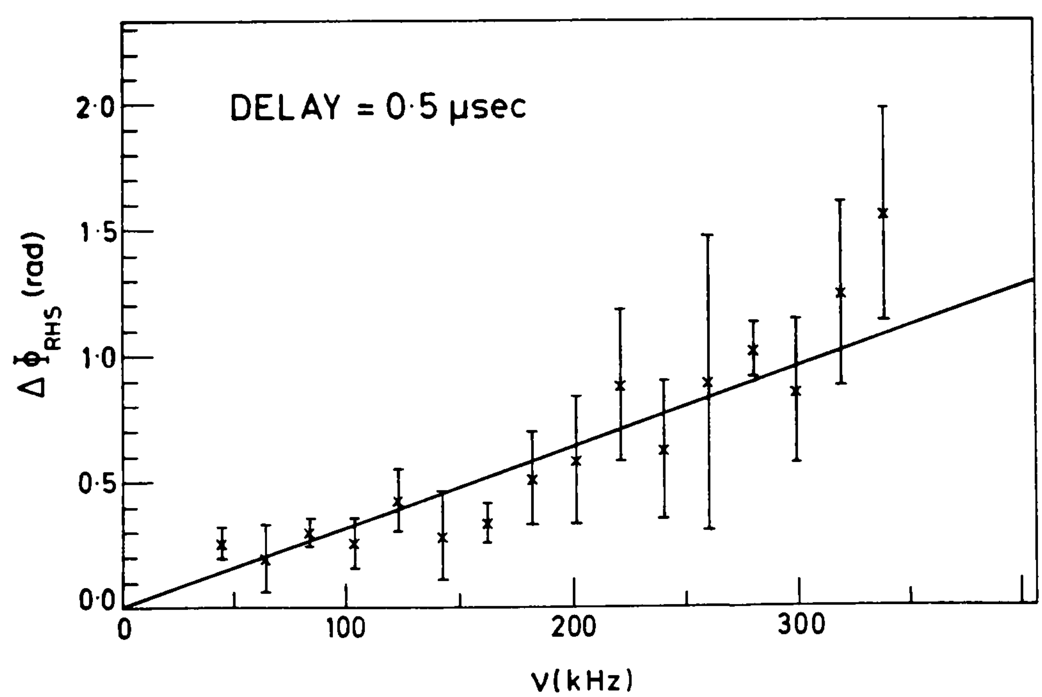

Figure 5.4: *Phase jumps between ADC in function of frequency.*

5.2 Micro-instabilities

Most of the explanations for density fluctuations and anomalous transport observed in tokamak rely on the drift-wave(Liewer,1985). A full review of all the drift-wave theory(Tang,1978) exceeds the scope of this work and only the relevant points are going to be treated.

Drift waves result from perturbation of the density profile and propagate perpendicularly to the magnetic field and density gradient in the direction of the diamagnetic drift with a velocity for $k_\theta \gg k_{\|} \approx 1/Rq$ given by

$$v_{de} = \frac{\omega_{*e}}{k_\perp} = \frac{T}{eB_\phi n_o}\frac{\mathrm{d}n}{\mathrm{d}r} \ . \tag{5.4}$$

The derivation requires under the condition $\omega/k_{\|} \ll v_e$ that the electrons reach a Boltzmann distribution *i.e.*

$$\frac{\tilde{n}_e}{n_o} = \frac{e\tilde{\phi}}{T_e} \ . \tag{5.5}$$

The drift wave in the above model is neutrally stable($\gamma(k) = 0$), however it may be driven unstable by adding dissipative terms, these have the effect of restricting the electron flow along the field line. The $\tilde{n}_e$ and $\tilde{\phi}$ are no longer in phase and the drift wave can grow.

The electron drift wave is most unstable when the ion temperature gradient is smaller than or about equal to the density gradient($\eta_i \equiv d\ln(T_i)/d\ln(n) \lesssim$ 1–2; Guzdar, 1983) which is the case for most tokamak. Electron drift waves are divided into three classes according to the collision rate between the electron and ion(ν_{ei}):

- collisional, resistive or dissipative drift instabilities(for $\nu_{ei} > v_e/qR$) are driven by electron–ion drag which impedes the parallel electron motion. These modes are likely candidates for edge plasma fluctuations.

- collisionless or universal drift instabilities (for $(r/R)^{\frac{3}{2}} < \nu_{ei}(qR/v_e) < 1$) are unstable because of inverse electron Landau damping *i.e.* a resonance of the waves with the electrons.

- trapped electron drift modes(for $(R/r)^{\frac{3}{2}}\nu_{ei} < v_e/qR$) are unstable because a fraction of the electrons are trapped in the magnetic mirror of the poloidal field spatial modulation.

The last instability has been a favorite candidate to explain anomalous transport in the hot collisionless core plasma (Waltz, 1985; Romanelli *et al.*, 1986) and has a linear growth rate(Kadomtsev and Poguste, 1971)

$$\frac{\gamma}{\omega_*} \sim \epsilon^{\frac{3}{2}} \frac{\omega_T}{\nu_{ei}} \,. \tag{5.6}$$

where $\omega_T = k_\theta (\mathrm{d}T_e/\mathrm{d}r)/(eB_o)$.

For TOSCA parameters(see table 5.1), this mode can exist for $r/a < 0.5$ with a growth rate of $\gamma/\omega_* \sim 0.2$. This correspond to a strong instability and demonstrates the need for models with strong turbulence.

A theory of strong turbulence is defined as one in which the effects of the turbulent fluctuation themselves are included to lowest order in calculating the relationship between the particles(or fluid) motion and the fluctuation in the electric and/or magnetic fields. Many computer models of non-linear fluid equations(Hasegawa and Mima, 1978; Waltz and Dominguez, 1983; Terry and Diamond, 1985) have given concordant results. They all yield a saturated fluctuation level($\tilde{n}_e/n$) equal to the mixing length level (Kadomtsev, 1965)

$$\frac{\tilde{n}_e}{n_o} \sim \frac{1}{k_\perp L_n} \tag{5.7}$$

where $L_n = n_o(dn/dx)^{-1}$ is the density-gradient scale length. At this level the fluctuations are large enough instantaneously to flatten the density gradient which is the free energy source for the fluctuations.

Non-linear processes can couple modes of comparable poloidal wavenumber (k_θ) and cause a local transfer of mode energy from the most unstable ($k_\theta \rho_s \sim 1$) towards smaller wavenumbers leading to an "inverse cascade" effect. The various models then predict that the mean wavenumber falls in the range $k_\theta \rho_s \sim 0.1$–0.3. The mode coupling process also couples the radial(k_r) and poloidal(k_θ) modes producing isotropic turbulence in the poloidal plane. The fluctuations with small wave number(k) are then finally damped by non-linear Landau damping(Sagdeev and Galeev, 1969) and non-linear magnetic shear damping(Tange *et al.*, 1982).

Howling(1985) found that the results of an analytical two-point renormalisation of the non-linear fluid equation by Terry and Diamond(1985), provide a good description of TOSCA edge plasma turbulence. Together with all the previous properties, the model yields a broadband spectrum characteristic of high-level incoherent activity for which the power decays approximatively as $P(f) \sim f^{-2}$.

Most models consider the drift wave as purely electrostatic. However Waltz (1985) showed that the drift wave has a magnetic component for $\beta_\theta > 1$ given by

$$\frac{\tilde{b}_\perp}{B_\phi} \sim \frac{\beta}{2}\frac{q\tilde{n}_e}{n} \ . \tag{5.8}$$

Other electromagnetic instabilities exist in the plasma(micro-tearing, rippling mode ...) but they are not detectable directly from our FFS diagnostic.

5.3 Fluctuation-induced transport

In this section, the mechanisms by which turbulence can cause particle and energy radial transport in the plasma are considered. Small fluctuations in the electric ($\tilde{E}$) and magnetic($\tilde{b}$) fields of a tokamak lead to fluctuation in the particle velocities and position which could result in additional transport.

The radial fluctuation velocity($\tilde{v}_r$) resulting from these fluctuating fields can be expressed as:

$$\tilde{v}_r \simeq \frac{\tilde{E}_\theta}{B_t} + v_\parallel \frac{\tilde{b}_r}{B_t} \tag{5.9}$$

where $v_\parallel$ is the parallel velocity flow and is limited to the ion thermal velocity by ambipolar flow. For TOSCA(Howling, 1985), the electrostatic contribution to radial velocity in the last equation dominates the magnetic one. The radial flux of particles is then given by

$$\Gamma_\perp = \left\langle \frac{\tilde{n}\tilde{E}_\theta}{B} \right\rangle \equiv -D_\perp \nabla n \tag{5.10}$$

where the brackets denote a time average and $D_\perp$ is the perpendicular diffusion coefficient. Although simple in appearance, evaluation of the flux involves the measurement of many quantities. To illustrate this, we rewrite the last equation to express the radial flux in a small band of frequency $d\omega$

$$\Gamma_\perp(\omega)\;\; d\omega = \frac{k_\theta(\omega)}{B} |\gamma_{n\phi}(\omega)| \sin(\Theta_{n\phi}(\omega)) \tilde{n}_{rms} \tilde{\phi}_{rms}\; d\omega \tag{5.11}$$

where

$$\begin{aligned} \tilde{\phi} &= \text{fluctuating electric potential} = \tilde{E}/k, \\ \gamma_{n\phi} &= \text{degree of coherence between } n \text{ and } \phi, \\ \Theta_{n\phi} &= \text{angle between } n \text{ and } \phi. \end{aligned}$$

All of these parameters could vary with frequency but also in space and time during the course of the experiments. Estimation of a transport coefficient with only a knowledge of $\tilde{n}$ will rely heavily on assumptions. The most common one is to assume quasi-linear turbulence by introducing a phase difference (γ_k/ω_{*e}) into the Boltzmann equation, *viz.*:

$$\frac{\tilde{n}_e}{n_o} = \left(1 - j\frac{\gamma_k}{\omega_{*e}}\right) \frac{e\tilde{\phi}}{T_e} \;. \tag{5.12}$$

By substituting this into equation 5.10, the radial diffusion coefficient can be written as

$$D_\perp \sim \gamma_k \left\langle \frac{\tilde{n}_e}{n_o} \right\rangle^2 L_n^2 \;. \tag{5.13}$$

Assuming that the saturation level of the fluctuation occurs at the mixing length level, the diffusion coefficient is equal to $D_\perp \sim \gamma_k/k^2$ (Kadomtsev, 1971).

Similarly, the heat flux induced by fluctuations can be calculated by(Liewer, 1985)

$$Q_{\perp e} = \frac{5}{2} e T_e \left\langle \frac{\tilde{n}\tilde{E}_\theta}{B} \right\rangle + \frac{5}{2} e n_e \left\langle \frac{\tilde{T}_e \tilde{E}_\theta}{B} \right\rangle + K_{\parallel e} \left(\frac{\langle \tilde{B}_r^2 \rangle}{B^2} + \left\langle \frac{|\tilde{B}_r|}{B} \frac{d\tilde{T}_e}{dr} \right\rangle \right) \tag{5.14}$$

where $K_{\parallel}$ is the classical parallel heat flux(Braginskii, 1965). The first two terms represent the electrostatic contribution to heat flux and can be combined using the pressure fluctuations($\tilde{P}_e$) to $\left\langle \tilde{P}_e \tilde{E}_\theta / B \right\rangle$. The last term is the conductive heat flow due to magnetic field fluctuations (Haas, 1981).

TOSCA is operated in the low-density($\overline{n}_e < 2 \times 10^{19}$ m^{-3}) electron dominated regime where the electron losses determine the energy confinement time($\tau_E \ll \tau_{equip.}$)(Liewer, 1985). This small plasma pressure(low β) does not induce ballooning modes and additional transport due to magnetic field fluctuations is negligible(Waltz, 1985; Ellis, 1984). Evolution of a heat pulse produced by an $m = 1$ internal disruption suggests that the energy loss is due to a small scale diffusive-type process.

Chapter 6

Results of plasma experiments

In this chapter the experimental observations of plasma density fluctuations will be presented in a detailed fashion followed by a discussion of the results including a comparison with transport estimates.

6.1 Temporal dependency

The collected scattered signal(I_{ac}) for a typical plasma discharge is displayed in figure 6.1 for each one of the 12 detectors. The plasma parameters for this shot are illustrated in figure 5.1. The array was oriented to look predominantly in the poloidal direction and the spacing of the elements corresponds to a $\Delta u_x = \Delta x / W_i \simeq 0.3$. The formation and extinction of the plasma can easily be distinguished from the noise which is 10 times smaller than the signal for detectors around $u_x \approx \pm 1$. The detectors around $u = 0$ and in the wings of the Gaussian($|u| > 1$) shows the expected decrease in intensity for the FFS signal.

After the breakdown of the gas, the density fluctuations rises steadily with the mean electron density before decreasing to a stable value when the latter reaches a plateau. This phenomena was also observed by van Andel *et al.*(1986) and Strachan

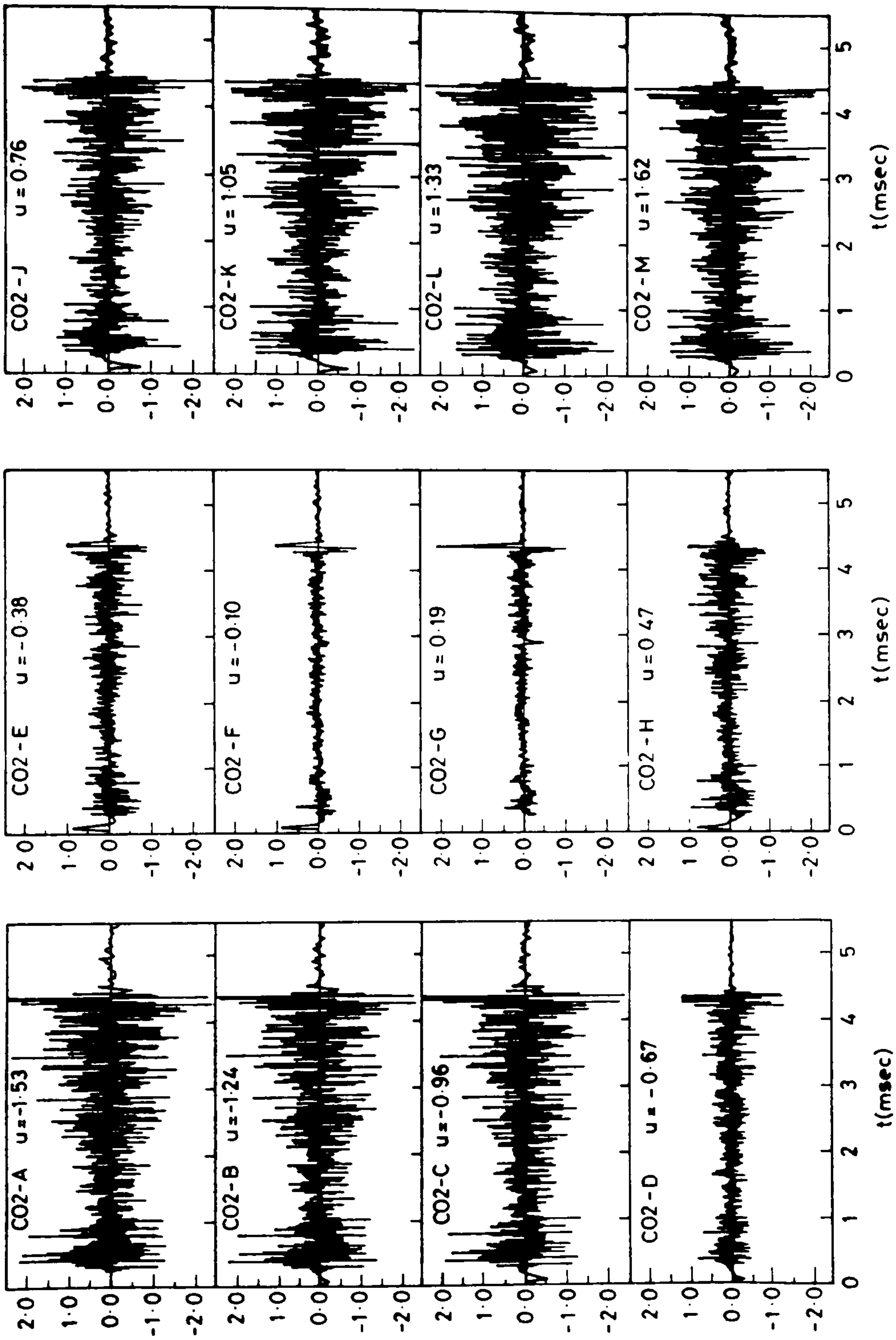

Figure 6.1: *Typical scattered signal for plasma shot.*

et al.(1982). The fluctuation level thereafter increases with the density until the end of the discharge when a burst of activity occurs. The beginning and end of the discharge were not analysed with the FFS theory because of their transient nature which cannot be Fourier analysed. In the following sections, we will restrict the study to the plateau or slowly varying region only.

In figure 6.2 is shown the power spectra of the detector at $u = -1$ for two different time periods during the discharge. The first one(fig 6.2(a)), which corresponds to the period 1.0–1.5 msec, shows no strong peaks and displays a roll-off frequency around 150 kHz. By contrast, the spectra of a later period exhibits peaks which will be analysed further in section 6–7. These distributions are not true power spectra since the instrumental function which depends on K, has not been deconvolved at this stage. Nevertheless, they help in identifying the coherent modes.

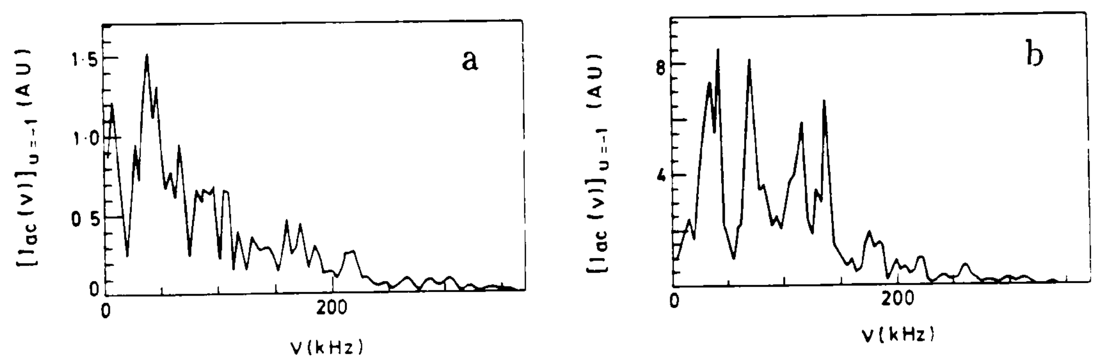

Figure 6.2: *Power spectra for scattered signal at u_x=-1. for the time period 1-1.5 msec(a) and 2-2.5 msec(b).*

Before proceeding to further analysis, a brief survey of the temporal variation of the main laser beam is done to determine the effects of vibration on the signal. Figure 6.3 shows the variation of the DC-power of the laser beam and the loop voltage versus time. The plasma is present when the loop voltage is positive. The power falling onto each detector was calculated from the digitised V_i^{dc} and V_v^{dc} and the calibration of section 3–3. The graphs on the left represents one plasma shot with the array pointing vertically and the light focused with a cylindrical lens while the one on the right is another shot without the the cylindrical lens. A comparison

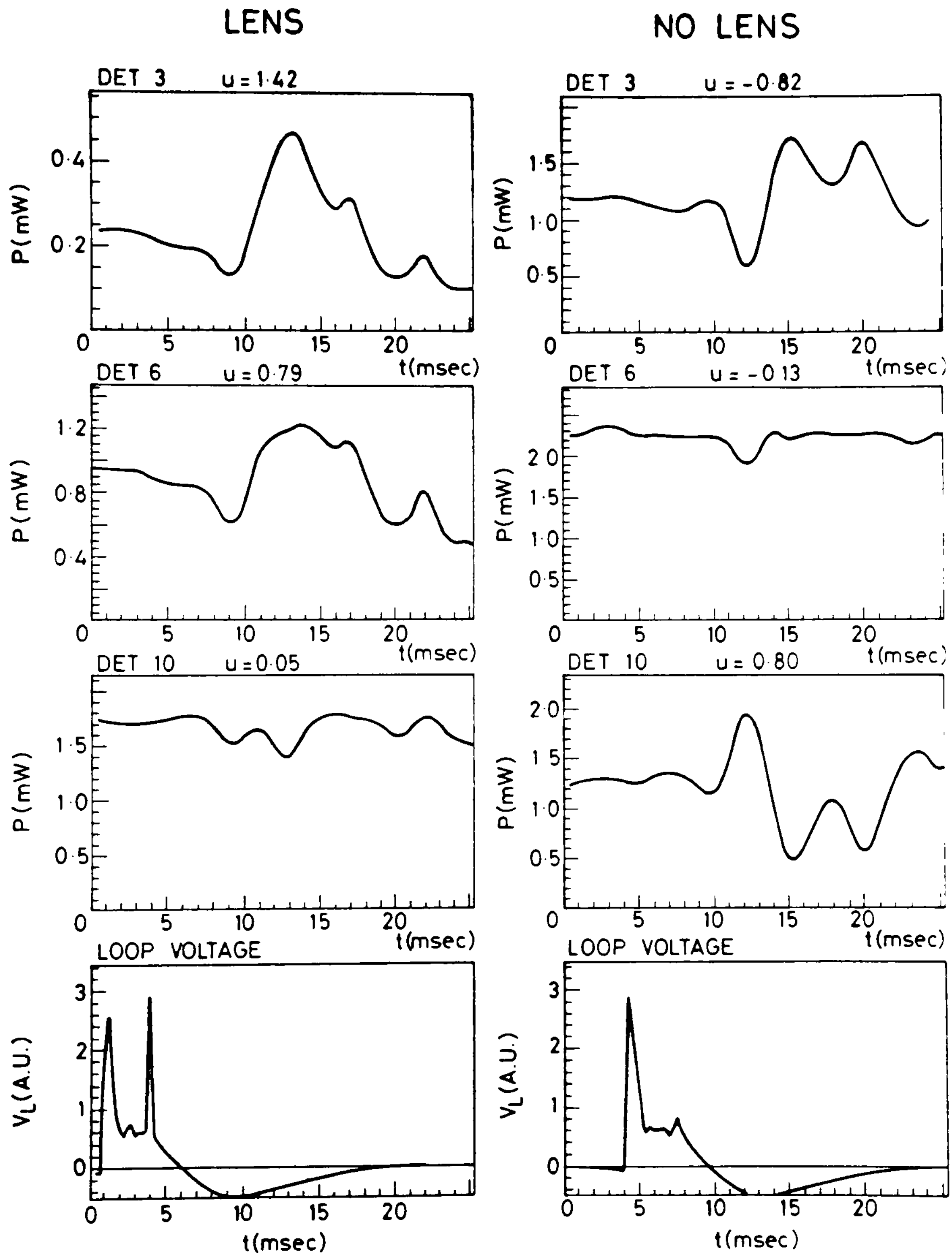

Figure 6.3: *Variation of laser beam power at detector due to mechanical vibration.*

of the power with the loop voltage measured with the same ADC shows that the mechanical vibrations are stronger after the discharge is terminated. Furthermore, the anti-symmetric time behavior of the signal for opposite detectors($u = 1$ and $u = -1$) indicates that the beam moves mainly vertically at the detector. The beam moves slightly during the discharge but nothing significant. Due to its integration effect, the insertion of a cylindrical lens should eliminate any horizontal vibration but the shot without the lens indicates small horizontal variations during the discharge. It appears safe however to assume that the vibration of the mirrors around the machine does not affect the measurement of the fluctuation during the discharge.

6.2 Statistical analysis

Before going on to the results, a statistical analysis of the raw data ($\tilde{n}_e$) can help in identifying the coherent structure of the turbulence. Rusbridge(1986) suggested the evaluation of many statistical quantities on the experimental data to permit comparisons with results from numerical simulations.

A useful diagnostic in the identification of self coherence is the Kurtosis ($\mathcal{K}u$) or flatness, defined for zero mean fluctuation as $\mathcal{K}u(\phi) =< \phi^4 > / < \phi^2 >^2$ where the angle brackets represent ensemble average. Suitably normalised, this has the value three for completely random fluctuations and for the FFS signal we obtain a value of $\mathcal{K}u(\tilde{n}_e) \simeq 3.3 - 4$. This indicates that the density fluctuation is not self coherent and more random in nature. Another diagnostic test is the Skewness defined as $\mathcal{S}k(\phi) = < \phi^3 > / < \phi^2 >^{3/2}$ where $< \phi >\equiv 0$. Its value should be zero for random fluctuation and it usually varies between ± 0.5 for the scattered intensity. Theoretically, these calculations are only valid for ergodic data in which the average moments do not depend on the starting time. In our application the first few moments do not vary much for the same plasma conditions (n_e, B, I) and we can assume our signal to be approximately ergodic.

The parent distribution which describes the spread of the data points is another useful statistical quantity. The probability distribution of our FFS signal(Volt) is plotted in figure 6.4 as a histogram with error bars given as the square root of the number of events for each voltage value. A chi-square test, which compares the experimental distribution to a gaussian parent distribution, has been performed and yields a reduce ${\chi^2}_\nu = \chi^2/\nu = 0.97$ where ν is the number of degrees of freedom. This signifies that the parent distribution is Gaussian and that it describes well the spread of points as can be seen on figure 6.4.

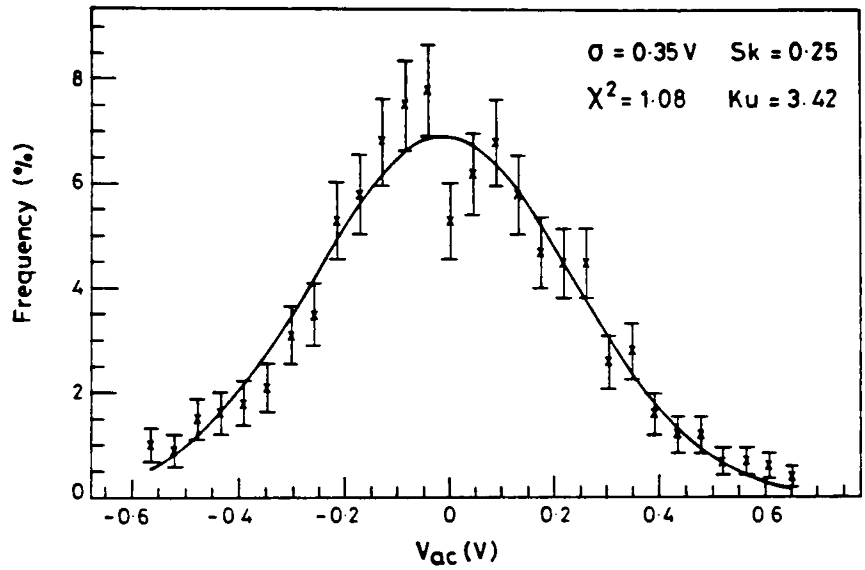

Figure 6.4: *Probability distribution of scattered signal.*

6.2.1 Bicoherence

Linear spectral analysis is of limited value when various spectral components interact with one another due to some non-linear or parametric process. In such a case, higher order spectral technique is necessary to characterise the fluctuating signal. Quadratic non-linear interaction manifests itself through the bispectrum(Kim and Powers,1979) defined by

$$B(k,l) = \frac{1}{N}\sum_{i=1}^{n} F_k^i F_l^i F_{k+l}^{*i}$$

where F_k^i is the Fourier component at frequency ω_k of the i^{th} time series out of n. $\mathcal{B}$ is non-zero only if there is a phase dependence between 3 modes. A test of the coupling model is given by the bicoherence spectrum $b(k,l)$, defined by

$$b^2(k,l) = \frac{|\mathcal{B}(k,l)|^2}{\frac{1}{N}\left[\sum |F_k^i|^4 \sum |F_l^i|^4\right]^{\frac{1}{2}} \sum |F_{k+l}^i|^2}$$

Calculation of $b^2(k,l)$ for the FFS showed no signal above the expected noise level. This indicates a system with many different modes or just random noise.

A recent paper by Ritz *et al.*(1988) calculates the growth rate and the energy cascading for the data measured by a double probe at the edge. Their technique cannot be applied to the scattered data because it involves bicoherence spectrum calculation which as just shown, are meaningless for our signal. Also, simultaneous measurements at two spatial positions are required, while we have only one.

6.2.2 Dimensionality

One question that we might address is whether the turbulence represented by these plasma fluctuations is truly chaotic or deterministic, *i.e.* does the turbulence posses an infinite number of degrees of freedom or can the dynamical system be modeled by non-linear equations with only few variables. This bears on the question of the number of independent processes producing the signal. An algorithm proposed by Grassberger and Procaccia(1983) estimates such number of degrees of freedom(ν) and we will briefly describe it.

Let $x(t)$ be the time series of the fluctuation. The analysis requires the construction of multidimensional vectors from these signals; this is done by making the vector component equal to different points taken at a regular time interval. Thus the L dimensional vector $X_L(t)$ is given by:

$$X_L(t_k) = [x(t_k), x(t_k+\tau), x(t_k+2\tau)\ldots, x(t_k+(L-1)\tau)]$$

where τ is the time lag. From these vectors we calculate the integral correlation function:

$$C(r) = \lim_{N\to\infty} \frac{1}{N^2} \sum_{i,j=1}^{N} H(r - |X_L(t_i) - X_L(t_j)|)$$

where H is the Heaviside step function. $C(r)$ is a measure of the number of points in this L dimensional space which are within a distance r. For value of L large enough, the dimension ν will be given by:

$$\nu = \lim_{r\to 0} \frac{\mathrm{d}\ln C(r)}{\mathrm{d}\ \ln r}$$

This procedure has been applied to the analysis of different signals on TOSCA: FFS($\tilde{n}_e$), Langmuir probe($\tilde{V}_f$) and magnetic coils ($\tilde{B}_\theta$), as reported in Côté *et al.*(1985). The signals were sampled at 1 MHz and time series of up to 2000 points during the flat top have been used. Figure 6.5 shows a plot of the correlation integral ($\log(C(r))$) of the FFS signal for a time lag of τ=7 μsec and different values of L. The slope in this case does not saturate to a finite value which indicates a high value for the dimensionality or that the fluctuation resembles white noise.

To make a clearer comparison, we plotted on figure 6.6 the dependence of the dimensionality(ν) on the number of phase space variables(L) for the 3 TOSCA signals and for a white noise signal. The latter has the highest dimensionality and is close to the expected theoretical limit of $\nu = L$. Departure from the limit is due to the finite size of the phase space and would have required more points($N \gg 10000$) and smaller spacing.

Both the CO_2 scattering and the Langmuir probe signal exhibit a non-saturation of the dimensionality(ν). This indicates a higher value of number of degrees of freedom or that the fluctuation behaves as white noise. With the magnetic coil however, ν saturates around 2.4 which indicates that the activity is characterised by fractal dimensionality associated with a strange attractor and that only three variables are involved.

A recent paper by Barkley *et al.*(1988) estimated the correlation dimension of plasma turbulence measured by coherent scattering on TFR. By having a high

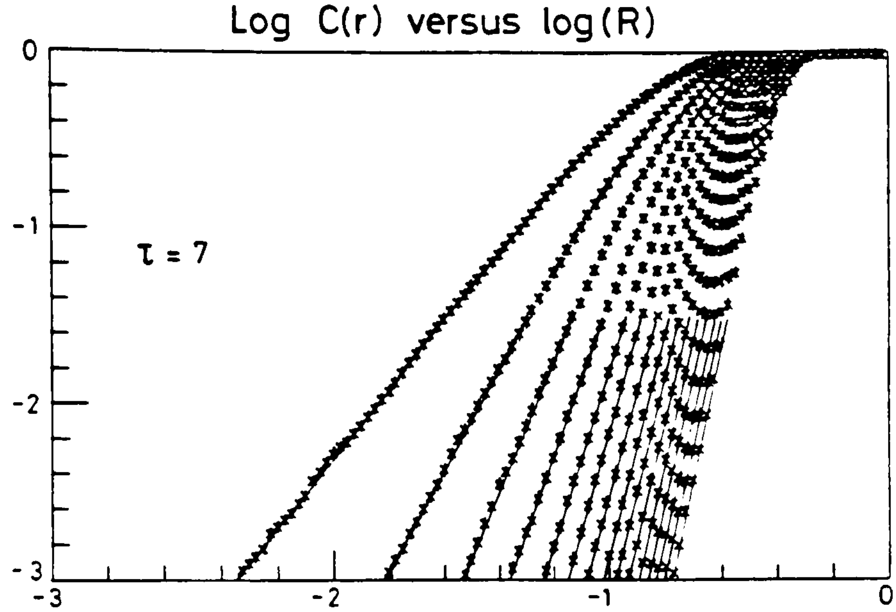

Figure 6.5: *Log $C(r)$ as a function of log(r) for FFS signal.*

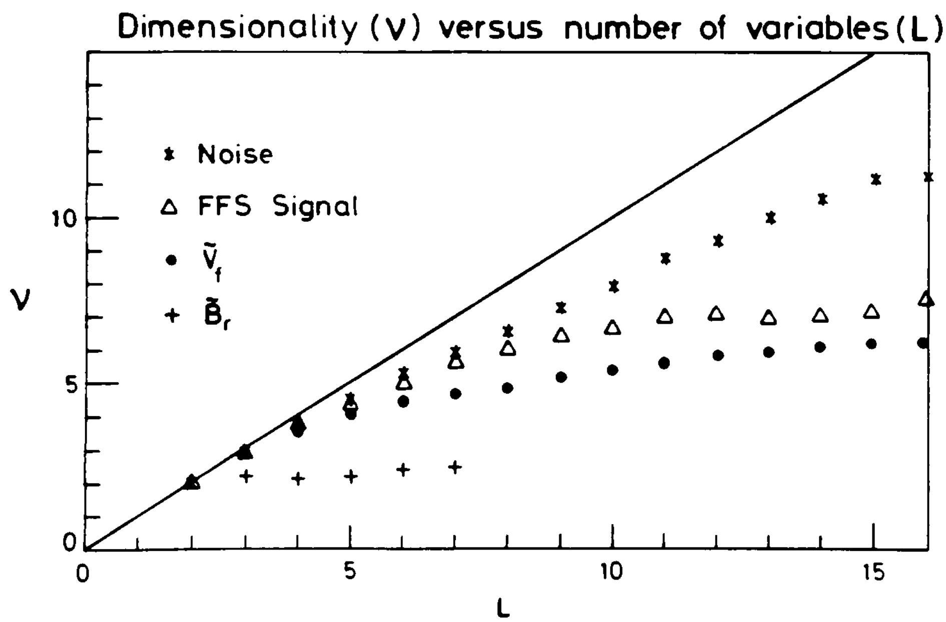

Figure 6.6: *Dimensionality(ν) as a function of L for white noise($*$), FFS signal($\triangle$), Langmuir probe($\bullet$) and radial magnetic field fluctuation($+$).*

acquisition rate(100 MHz), they discovered some structure in this turbulent process by measuring a low correlation exponent($\nu \sim 2.6$). This dimension is similar to the one obtained from the magnetic coils. They repeated their experiment with a slower acquisition rate like ours($\sim$ 4 MHz) and they did not find any saturation of ν with L. Since all our amplifiers were bandwidth limited($<$ 1MHz), the higher frequency range($\sim$ 100 MHz) was inaccessible in this experiment.

6.3 Two dimensional mapping of the scattered light

The FFS technique selects components of the fluctuations which possess K vector parallel to the array of detectors. In most of our experiments the array was positioned to measure only the poloidal K vector, but in the following an attempt was made to gather both directions (poloidal and toroidal) at once.

Experimentally this was achieved by removing the cylindrical lens of the optical path and by moving the laser beam every 3 plasma discharges perpendicularly across the array so that we scan u_y. Here we define u_x as the direction along the array and u_y the one orthogonal to u_x. This technique is similar to the one used for a FFS experiment using a single detector(Evans *et al.*,1983;Côté *et al.*,1985), but in this case the array sampled u_x at 12 positions instead of integrating along it with a lens. Seven positions of u_y spaced by $\Delta u_y = \Delta y/W_i$=0.4 were chosen with the 12 positions along the array($\Delta u_x = 0.3$) to produce the two dimensional(2-D) mapping. Two more u_y scans were taken at either end, but the poor signal to noise ratio due to the low power of the laser beam in the wings($<$ 2.% of the peak) lead us to ignore them. The plasma parameters were roughly constant($I_p = 10kA, \overline{n}_e = 8.0 \times 10^{18} m^{-3}, B_\phi = 0.45T$) over the 1 msec period of analysis and repeatable over the 21 shots.

A good check of the set up and stability of the laser was to deduce the waist along u_y from a knowledge of the DC-profile along u_x for each u_y position. The measured waist with the beam profiler was 2.75 $\pm$ 0.1 mm which compares well with the value deduced, namely 2.65 mm. The waist in the opposite direction (u_x) varied slightly for the 7 different u_y and we normalised it to 2.75 mm.

The data for each u_y position was analysed in the usual way using Fourier transform and produced intensity and phase profiles along u_x at a set of discrete frequencies. We combined the profiles of the seven u_y position to create a 2–D mapping of the signal and plotted the results for ν = 40 kHz and ν =160 kHz in figure 6.7 as functions of u_x and u_y. Each level for the intensity plot represents $\frac{1}{9}$ of the peak intensity, while for the phase profile each level correspond to an increase of $\frac{2}{3}$ radians. The representation of the phase profile by this 2–D mapping is slightly misleading because the only meaningful results are parallel to the u_x axis. Nevertheless, by normalising the phase signal to the mean of the extreme detectors good comparison can be made.

Both plots suggests that a wave is propagating at an angle of about 30° anti clockwise(acw) from the u_x axis. This tilt is better seen with the equiphase of the phase plot. Unfortunately the position of the poloidal and toroidal axis with respect to the u_y and u_x axis is only known within $\pm$15°. The optical lay out introduces a rotation acw of 10°(.16 rad) due to the projection of the beam not going through the center of the torus. Also, to align the axis of the array in the proper vertical direction, we tilted the whole vacuum shroud adding an uncertainties around $\pm$10°.These 2–D plots allow the FFS signal to be interpreted as due to a plasma disturbance propagating within $\pm$15° of the poloidal direction.

Only a qualitative discussion of the contour plot will be presented since fittings of the integrated profiles with the cylindrical lens are simpler to perform and would yield the same results. A comparison of the intensity plots in figure 6.7(a) and figure 6.7(b) indicates that the higher frequency has a lower dip at the middle of the profile($u_x = 0, u_y = 0$). This corresponds using the theory of FFS to wavenumber which is larger at 160 kHz than for 40 kHz. The slope of the phase plot around

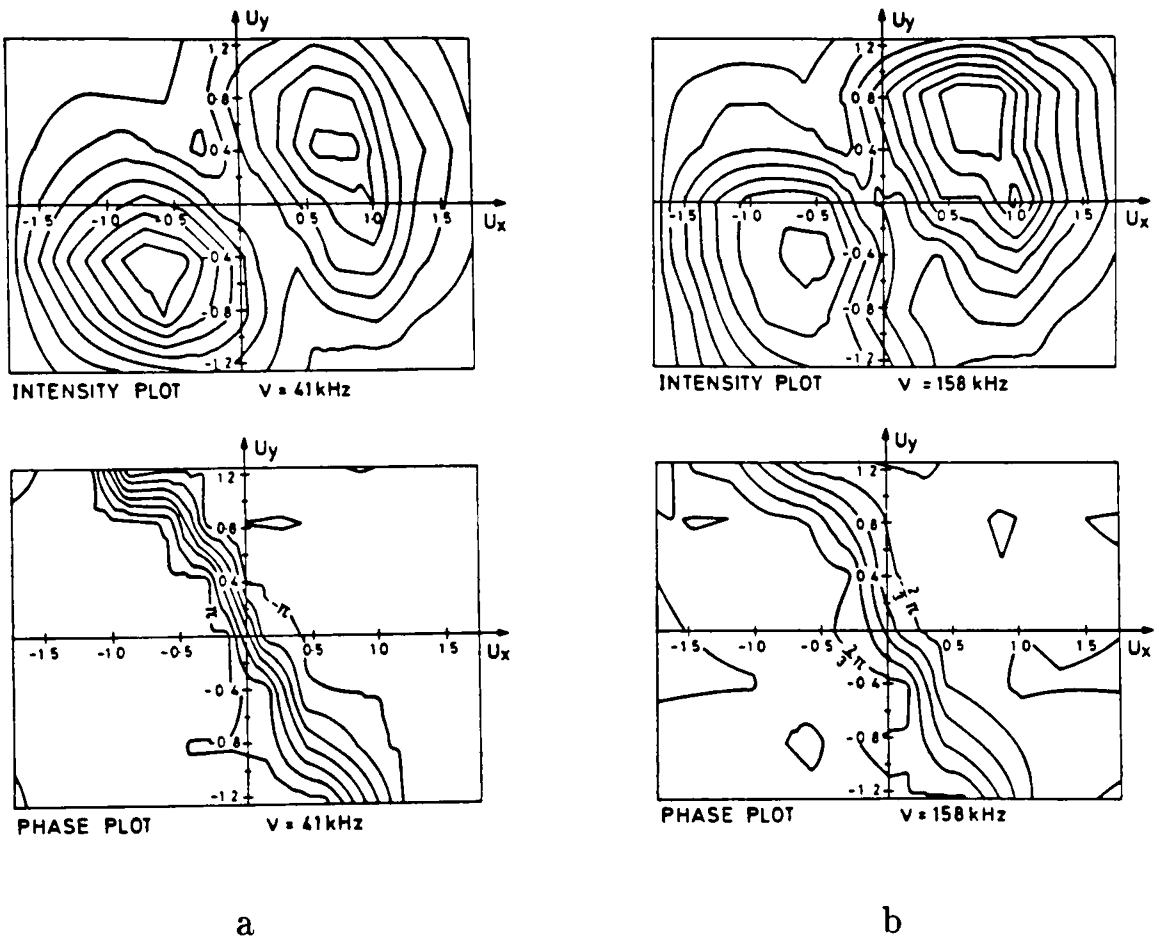

Figure 6.7: *2-dimensional plot of FFS signal for 40 kHz(a) and 160 kHz(b).*

the origin(S_o) is greater at lower frequencies(40 kHz) corroborating the intensity result of a larger K_θ at higher frequencies.

Another conclusion which can be drawn from these figures is the importance of using a cylindrical lens with an array of detectors. Absence of such a lens can lead to dramatic asymmetry which is only the result of a tilt in the direction of the wave. For example, a profile taken at $u_y = 0.4$ in figure 6.7 displays strong asymmetry even though the whole 2–D map does not. A cylindrical lens will integrate along the u_y axis for each u_x position and will yield a symmetric profile at all u_x if the disturbance can be modelled by a single wave(see Appendix B). This propagation direction effect does not, therefore, account for the asymmetry seen even when a cylindrical lens is in use.

6.4 Langmuir probe

In this section, we outline the typical results from a statistical analysis of the floating potential of a Langmuir probe at the plasma edge. As quoted in section 5.1.4, the floating potential on TOSCA corresponds to plasma potential fluctuations. The characteristics of these fluctuations provide guidance in selecting the appropriate model for the FFS analysis. The following results apart from the damping and the growth rate calculation have also been measured on TOSCA by A. Howling(1985).

The data were grouped in 3-5 shots to attain better statistical resolution. A power spectrum of the fluctuations is shown in figure 6.8. The broadband spectrum peaks at frequencies associated with MHD activities (40 kHz). After correcting for the anti-aliasing filters, the power spectrum decays at large frequencies with a power law dependence $P(f) \approx f^{-p}$ where the index $p = 2. \pm 0.5$.

Simultaneous measurements of floating potential at points toroidally and poloidally separated by 3 mm were made by aligning the 4-pin probe with the magnetic field. The average dispersion relation, wavenumber spread, growth and coherence

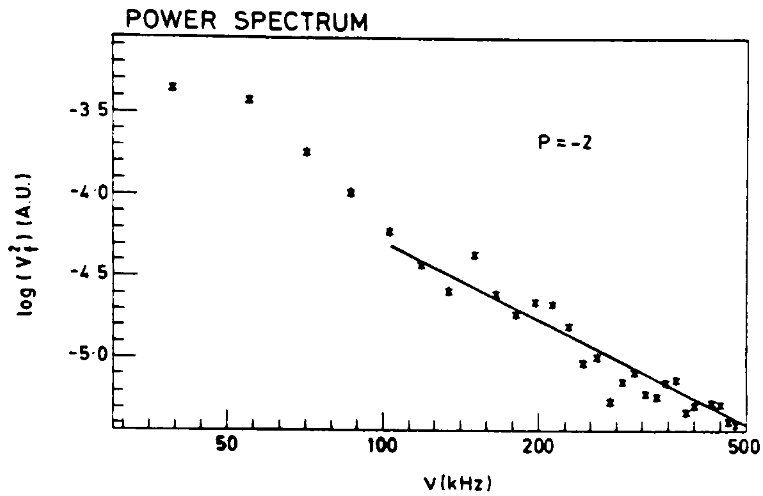

Figure 6.8: *Power spectrum for floating potential of Langmuir probe.*

were then calculated according to the method outlined in section 5.1.4 .

The results for the poloidal direction are displayed in figure 6.9. The phase spectrum shows a linear dispersion up to 200 kHz. The apparent phase velocity of 3.2 ± 0.2 in figure 6.9(b) is in the electron diamagnetic direction. The coherence (fig. 6.9(a)) decreases with frequency indicating a spread in wavenumber. The ratio of this spread (Δk) to the wavenumber is plotted in figure 6.9(c) and remains around unity for all frequencies. This implies a coherence length of the order of the wavelength. The growth rate(fig. 6.9(d)) in the electron diamagnetic direction is not significantly different from zero indicating some poloidal isotropy. Validation of the calculation for the last two parameters (Δk and α) is limited to coherence greater than 0.4 from the theory.

In the toroidal direction, the coherence is around 0.9 at all frequencies and the phase difference between the two probes is negligible ($\overline{\Theta}_{xy} \simeq 1° \pm 3°$). The growth rate is also constant and around zero.The toroidal wavenumber spread is smaller than the poloidal one which implies that the fluctuations are toroidally elongated.

In summary, the fluctuations seems to propagate predominantly in the electron diamagnetic drift direction to within 10°. The phase velocity calculated with this

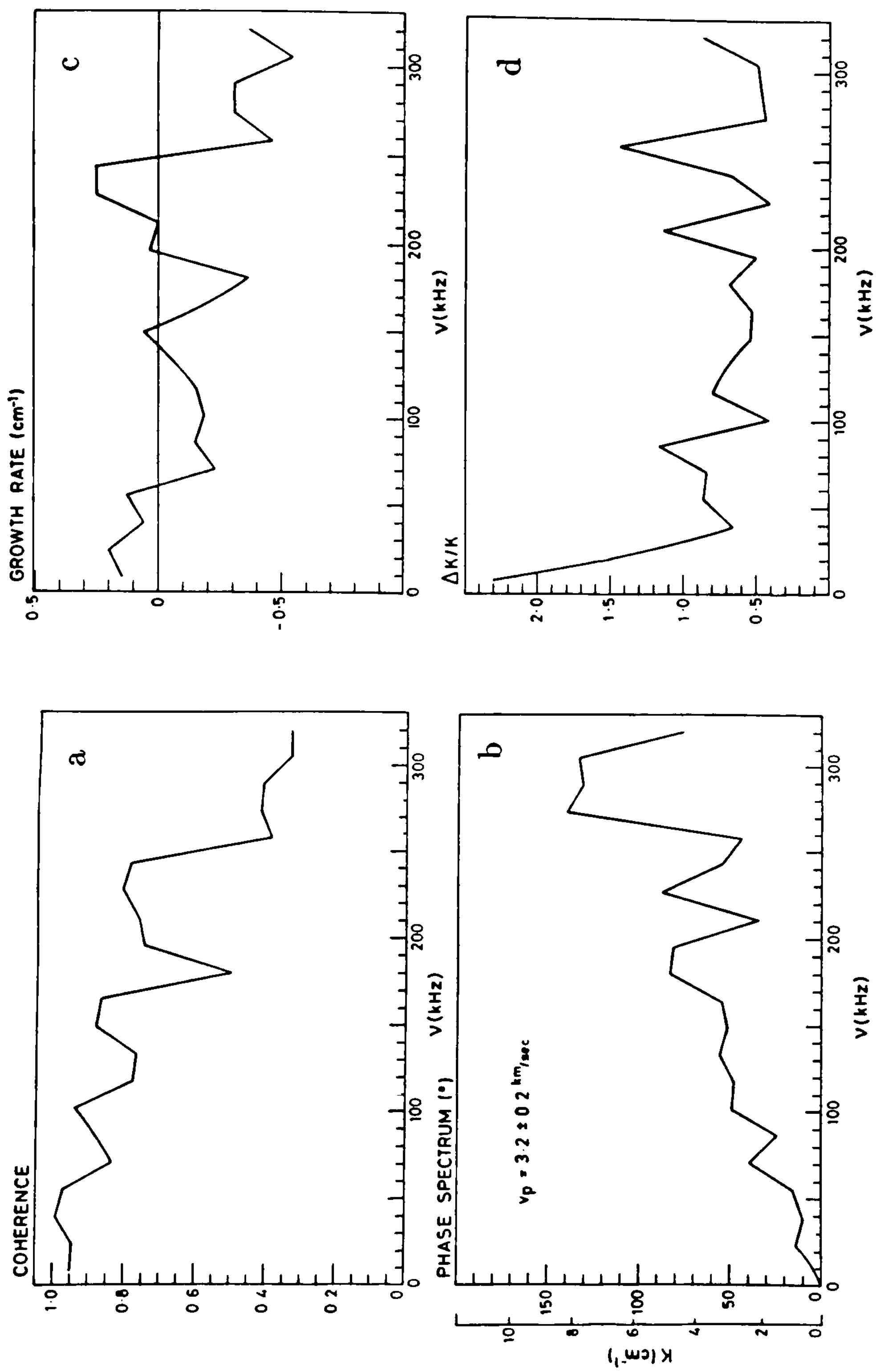

Figure 6.9: *Floating potential coherence spectrum(a), phase spectrum(b), growth rate spectrum(c) and $\Delta K/K(d)$.*

method can originate from true fluctuation propagation in the fluid rest frame and/or bulk plasma rotation. Since the main source of plasma rotation is the average electric field which has not been measured simultaneously, we are not able to distinguish between the two causes of phase velocity.

6.5 Single wave analysis

In this section, a typical plasma shot is analysed thoroughly to demonstrate the method and to extract the general characteristics of the discharge. As in Chapter 4, the shots were grouped in 3 for the envelopes calculation so as to reduce statistical errors. The plasma density was $8 \times 10^{18} m^{-3}$ and constant for a current of 10 kA. Two milliseconds after the breakdown of the gas, the data was collected for 0.5 msec. The linear array was directed vertically so as to measure poloidal perturbations. Fifteen intensity and phase profiles corresponding to 15 different frequencies were created following the block diagram of figure 3.9. The frequency spacing between each envelope was around 20 kHz and their width 4 kHz.

A typical intensity and phase profile is displayed in figure 6.11. The intensity profile exhibits the central dip and the two symmetric peaks which are characteristic of the scattering by a single wave. On the other hand, the phase profile is different from the expected results because of phase jumps due to a lack of synchronisation between the different ADC as explained in section 5.1.5 . By applying these corrections to the two extreme ADC(1 and 3), the phase profile appears correct. In this treatment, we assumed that the phase varied linearly around the transition point which might not always be true. By over compensating for the phase jump, the fitted value of v would be smaller than the expected one.

Before fitting the envelopes, it is informative to look at the variations of the parameters characterising the profiles for one time interval in one discharge. In figure 6.10, 6 parameters($R_1, R_2, u_o, u_{pk}, S_o, S_\infty$) defined in section 2.5 and calculated for this typical shot, are plotted against frequency. A parabolic interpolation over the 3 points around the two peaks and the trough of the intensity profile was carried out to improve the estimation of these parameters. The average trough position(u_o) is -0.05 which can be considered central since the dimensionless width of the detector is 0.15 . This position varies slightly (± 0.1) during the shots indicating as stated previously that vibration is not important for these short discharges ($t < 4$ msec). The trough position also coincides as expected with the inflexion point of the phase envelope. The peak position slightly increases with frequency(ν) from a level of 0.72 to 0.8 . The ratio in intensity between the trough and the average value of the peak (R_1) has a larger spread but a definite increasing linear trend can be seen between R_1 and ν.

In the case of the phase profile, the estimate for the slope S_o is calculated by taking the phase difference between neighbouring detectors at the centre while S_∞ is calculated by averaging the slope of the fitted lines used in the correction of the phase jumps. S_∞ increases with frequency while S_o decreases with it. Abrupt changes of the sign of S_o occur occasionally due to the $\pm 2\pi$ indeterminacy of the arctangent. All the dependence between the parameters (R_1, u_{pk}, S_o and S_∞) and the frequency seems to indicate that the wavenumber K (or v) is weakly dependent on ν.

The remaining parameter R_2 which is the ratio between the two peaks, points to a small asymmetry. By combining this weak asymmetry with the central trough position, we could say that the single wave model is sufficient to describe this shot. The parameter ΔS_∞ which is the difference in the slope between the two sides of the phase profile, should help in determining the right model but it lacks sufficient resolution to be a clear indicator.

The foregoing discussion about the variation of the parameters with respect to frequency yields mainly qualitative information about the disturbance. Quantitative results can be obtained, as for the air jet, by fitting the phase and intensity envelopes with the single wave model, and in the remainder of this section, we will

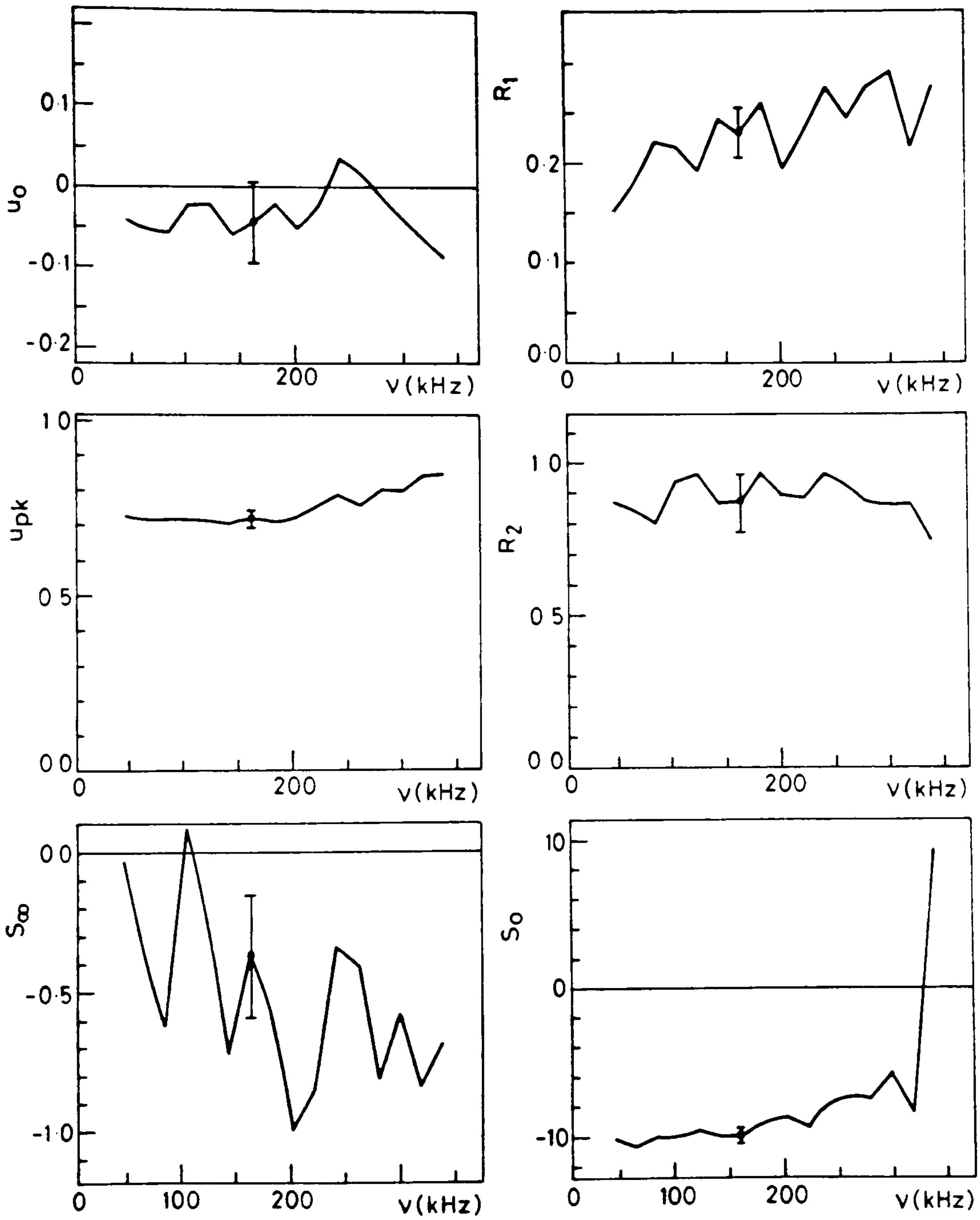

Figure 6.10: *Variation of shape parameters with frequency.*

follow this approach.

The choice of the right estimation of the position of the waist(ζ) in the fitting of the plasma results was less clear than for the air jet due to the added uncertainties coming from the correction of the phase jumps. The experimental value of 0.3 for ζ was the starting point for the algorithm of section 4–2 . The results from the intensity and phase profile were too far apart to reconcile them by fine adjustment of ζ. A value of $\zeta = 0.1$ did give less disparity in the main value of the two fittings but the distortion it created in the $\nu - K$ diagram was unacceptable. Instead, we fitted the envelopes with 3 free parameters (A_o, v and ζ) and the average value of ζ was found to be 0.25 ± 0.07 and 0.3 ± 0.2 for the intensity and phase profile respectively. Due to the small minor radius of TOSCA ($a_l = 8.0$ cm), fixing ζ is desirable so as to restrain the origin of the perturbations to be within the vessel. Hence, a value of ζ=0.25 was chosen for all of the following fittings.

Figure 6.11 shows the result of such analysis for 4 frequencies out of the 15. As for the 2–D mapping, the dip in the middle decreases with frequency indicating an increase of v which is resolved by the fitting program. The results of all the fittings are summarised in figure 6.12. The $\nu - K$ diagram of figure 6.12(a) exhibits strong linear correlation (r=0.9) which indicates a wavelike or bulk rotation of the perturbations. The slope of the best fitted line going through the origin corresponds to a phase velocity of 4.2 ± 0.4 km/sec. The error bars of the velocity are calculated by summing the relative errors of the linear fitting with that associated with the beam waist close to the plasma (W_o). This phase velocity is similar to that obtained with the Langmuir probe and a discussion of its relevance will be presented later.

A logarithmic plot of the line integrated fluctuation level($\tilde{n}_e L$) determined by the curve fitting versus frequency is shown in figure 6.12(b). This graph rather than the one shown in figure 6.2 is the true fluctuation power spectrum. Towards higher frequencies, the power of the fluctuations decreases according to a power law ν^{-2} which agrees with the observations made with the Langmuir probe. Spikes in the amplitude spectra often occur and are caused by an under-estimation of v(e.g.

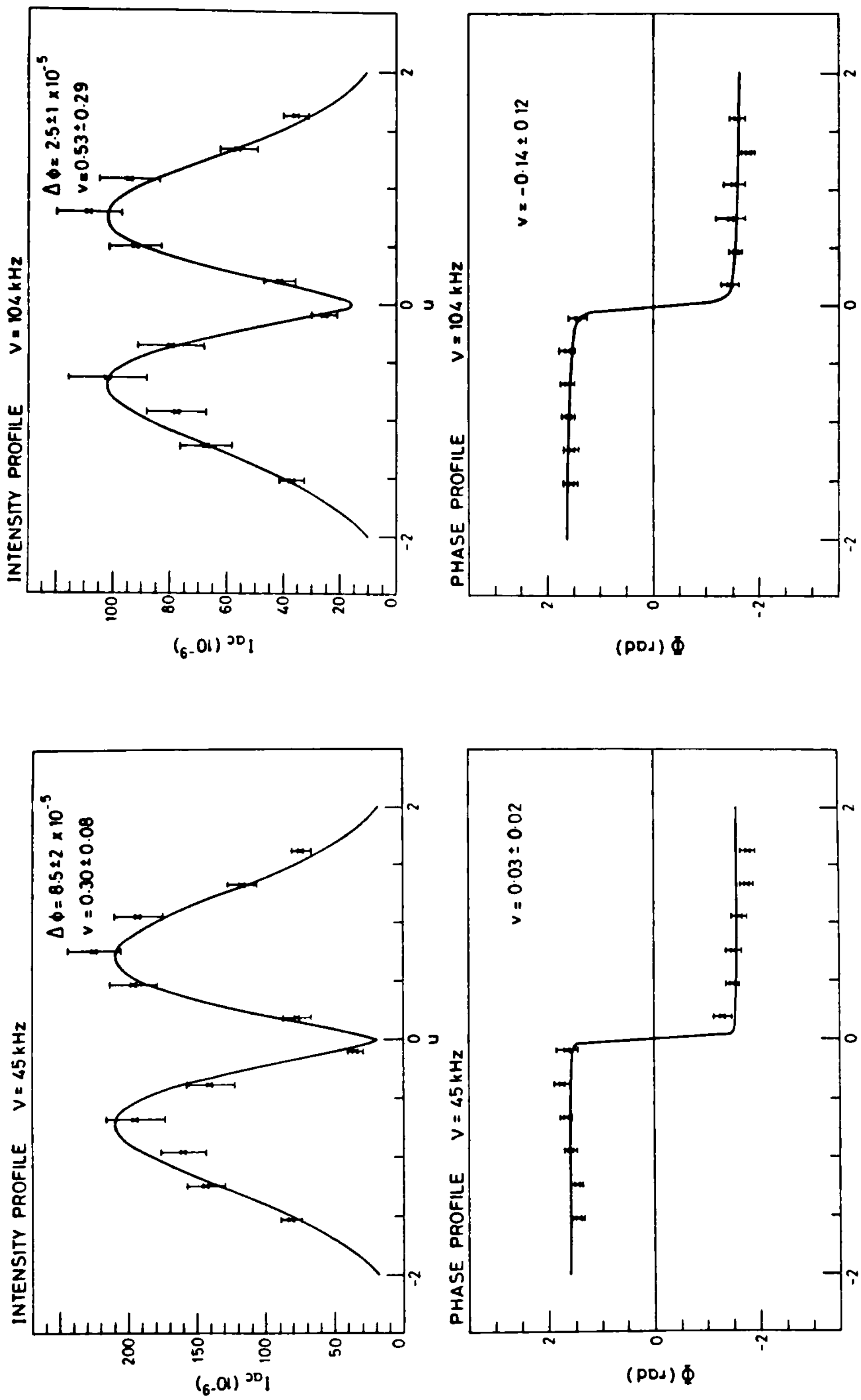

Figure 6.11: *Example of 4 envelope fitting from plasma scattering.*

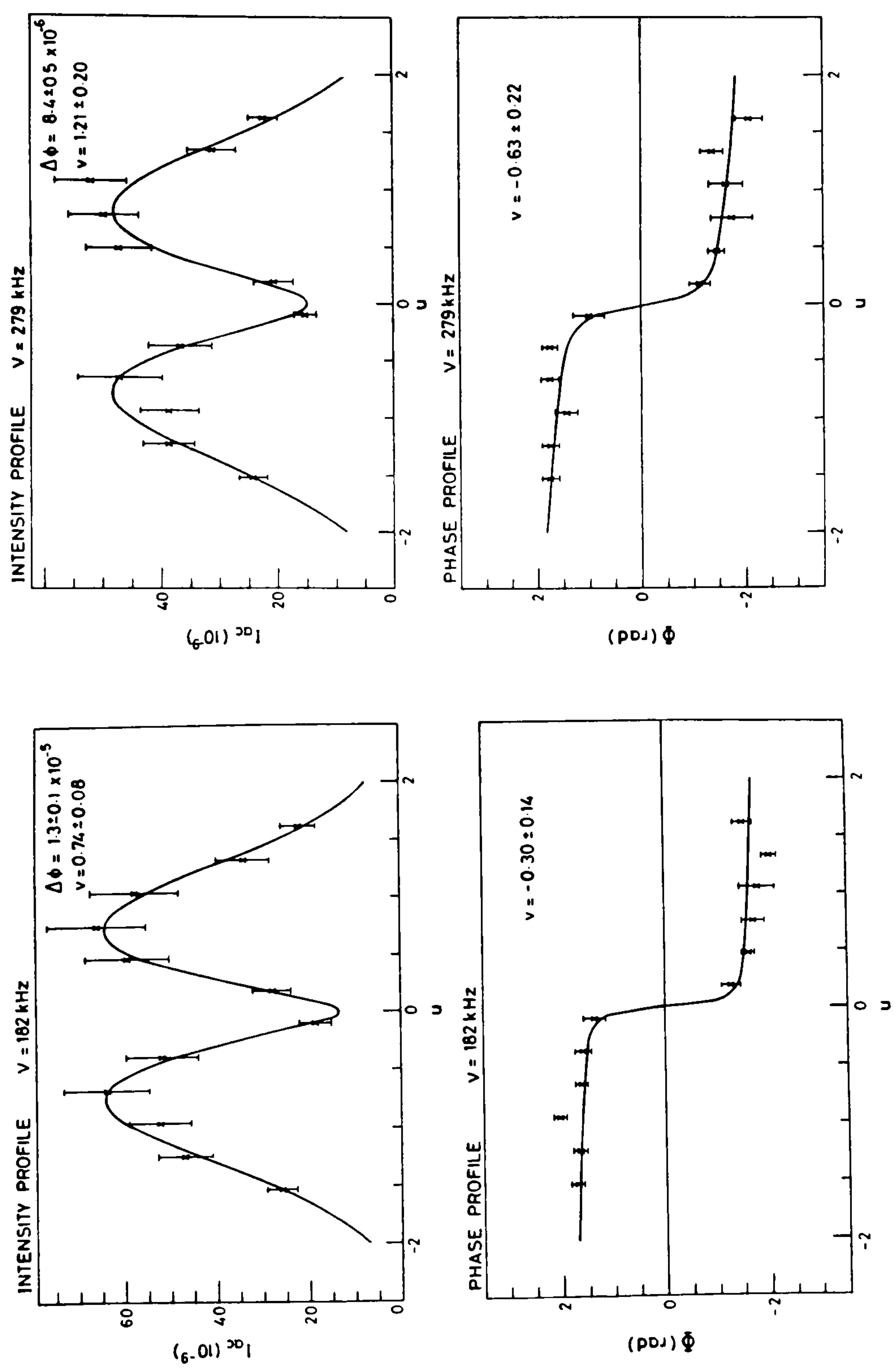
INTENSITY PROFILE
V = 279 kHz
Δφ = 8.4±0.5 x10^-6
v = 1.21±0.20
I_ac (10^-9)
u
PHASE PROFILE
V = 279 kHz
v = -0.63±0.22
Φ (rad)
u
INTENSITY PROFILE
V = 182 kHz
Δφ = 1.3±0.1 x10^-5
v = 0.74±0.08
I_ac (10^-9)
u
PHASE PROFILE
V = 182 kHz
v = -0.30±0.14
Φ (rad)
u

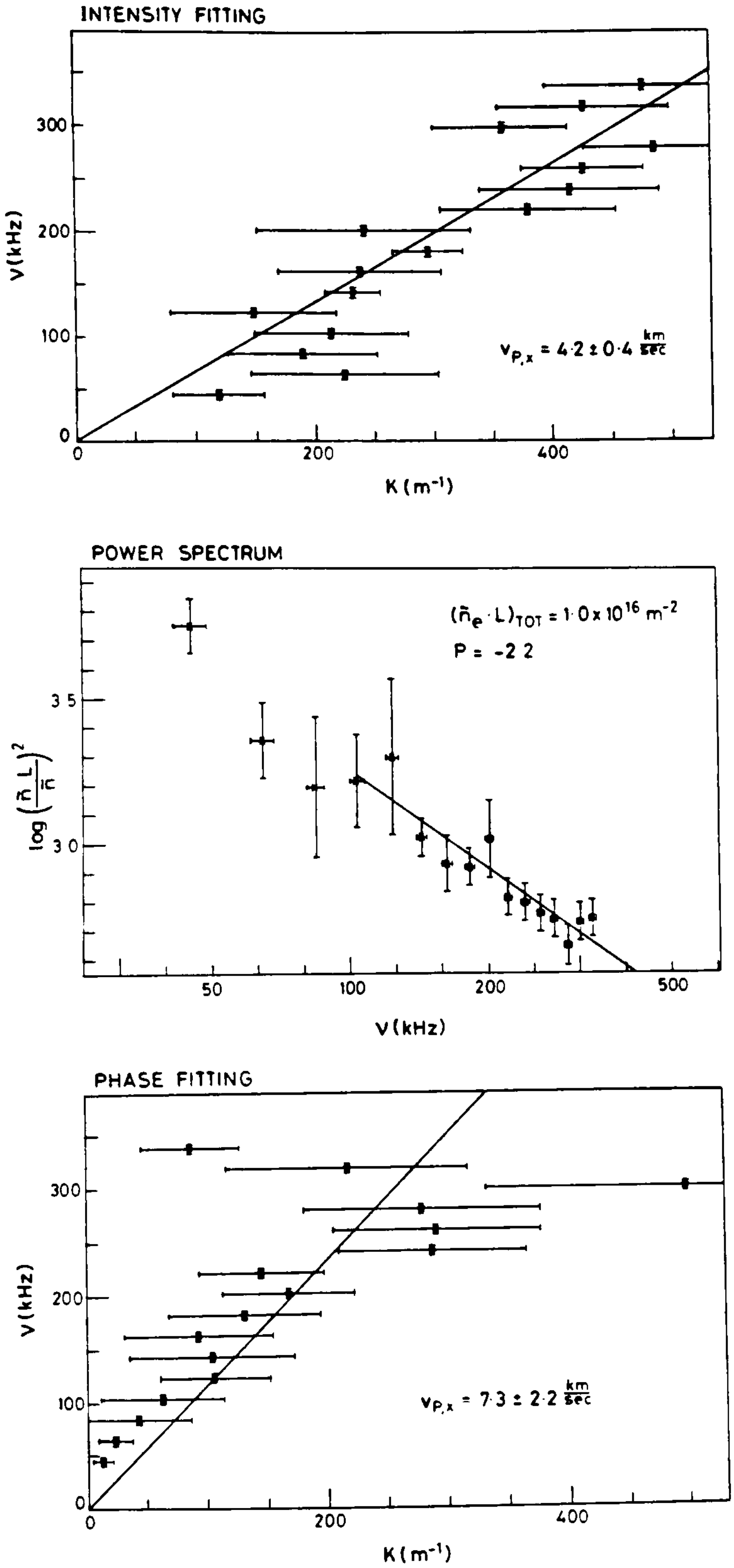

Figure 6.12: *ν-K diagram from intensity(a) and phase(c) fitting with amplitude spectrum(b).*

see at 200 kHz). This knock-on effect on the intensity arises from the insensitivity of the amplitude to the shape of the profile.

To obtain the fluctuation level($\tilde{n}_e$), it is necessary to estimate the interaction length L. The latter is bound on one hand by the size of the plasma($2a_l$) and on the other by the wavelength(Λ). Calculations by Weisen *et al.*(1988) showed that for an instrument effecting a line integration in a random medium, the effective integration length(L_{eff}) is given by $\sqrt{\ell_z L}$ where ℓ_z is the correlation length and L the interaction length. Experimentally, they found ℓ_z to be roughly equal to $\Lambda_{typ}/4$ where Λ_{typ} is the typical wavelength. The above calculations assumed isotropic and homogeneous fluctuations. For the measurements on TOSCA, $\ell_z \simeq 0.5$ cm and $L \simeq 8$ cm which imply a $L_{eff} \simeq 2$ cm.

The total fluctuation level calculated by summing

$$\tilde{n}_e = \frac{1}{L_{eff}}\sqrt{\Delta\nu\sum[\tilde{n}_e(\nu)L]^2} \tag{6.1}$$

is equal to $5.0 \times 10^{17} m^{-3}$. This level of density fluctuations is many orders of magnitude above the thermal level(Evans *et al.*,1983). By assuming that the turbulent region is situated around $r/a \simeq 0.5$ which correspond to a density of $8.0 \times 10^{18} m^{-3}$, the relative fluctuation level is 6%. The uncertainties on this level are estimated to be a factor 2 mainly due to the evaluation of L_{eff}.

The last graph in figure 6.12(c) is the $\nu - K$ diagram obtained via the phase profile. The K inferred tends to be smaller than that obtained from the intensity profile. One possible explanation for this systematic difference might be due to the correction of the phase jumps between ADC. Most of the fitted v are positive which correspond to waves propagating from left to right. Due to the lack of spatial resolution, the poloidal direction of propagation is indeterminate. Nevertheless, by assuming the electron diamagnetic direction given by the Langmuir probe we could say that the turbulence being observed lies in the upper half of the minor cross-section of the torus.

6.6 Comparison of different FFS models

Analysis of groups of shots using different FFS models are treated in this section. Only intensity profiles are going to be compared because of the more problematic analysis of the phase profiles. The study is restricted to two types of shot: symmetric and asymmetric.

The group of shots in the last section forms a good example of symmetrical shots. Fitting of these intensity profiles with other FFS models tends to give similar results as summarised in Table 6–1. No marked difference can be seen in the average phase velocity(v_ϕ), the total density fluctuations(n_e^{tot}) and the decay index(p) at large frequencies of the power spectra.

Model	$\overline{\chi^2}$	v_ϕ [km/sec]	Extra parameter	n_e^{tot} $[10^{17}m^{-3}]$	Power index (p)
1 wave	0.7	4.2 ± 0.4	—	5.0	-2.1
2 wave	0.5	4.3 ± 0.5	$2.5(a)$	5.4	-2.9
Damping	0.4	3.8 ± 0.6	$< 0.5(D)$	4.6	-1.8
ΔK	0.7	4.0 ± 0.5	$< 0.2(\Delta K)$	5.1	-2.4

Table 6.1: *Comparison between models for symmetric profiles.*

Fitting with the 2 wave model gives an amplitude ratio(a) larger than 2.5 which is equivalent to the single wave model. The damping model yields a slightly better average χ^2 over the 15 frequencies($\overline{\chi^2}$) than the others due to its adaptability to small asymmetry. Nevertheless, the small value of the damping inferred($<$ 0.5) signifies that a simpler model could have been used. Results of the ΔK models are very similar to the single wave case with only negligible $\Delta K(< 0.2)$ added. In summary, the extra parameters of these models are usually small ($\Delta K <$ 0.2; $Damping \simeq 0.5$) or large($a > 2.5$) confirming the appropriateness of the single wave model used.

In the case of the asymmetric profiles which we defined as envelopes with $R_2 < 0.8$ and $|u_o| > 0.1$, the situation is not as clear. One example of such a profile is shown in figure 6.13. They tend to occur when the density is high and/or we use a special frequency filter and constitute around 40% of the whole data base. As for the symmetric case, we fitted one group of shots with the 4 models and the results are listed in table 6–2. The volume effect is unimportant on TOSCA ($Q \ll 1$) which means that scattering occurs in the Raman–Nath regime.

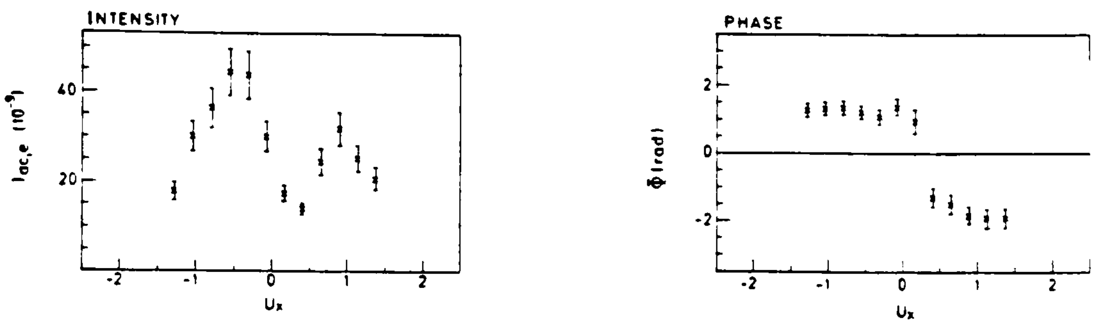

Figure 6.13: *Asymmetric intensity and phase profile.*

The single wave and the ΔK model give the worst χ^2 since they produce intrinsically symmetric profiles. The phase velocity, fluctuation level and decay power index inferred from the single wave model are consistent with the results for the symmetric profile and the Langmuir probe. The ν–K diagram of the ΔK model does not show a linear dispersion, but rather a cluster of points around $K = 3.0cm^{-1}$. The power decay index($p = -0.7$) is too small and is caused by large values of $\Delta K(0.6)$.

The 2 wave model does not give a cluster of points like the ΔK, but its large phase velocity, decay index and fluctuation level render it debatable. Before continuing with this model, it is worthwhile to question its validity for this plasma experiment. The underlying assumption in this model is that the two waves differ only by a phase difference which remains constant for all the selected time duration. Knowing that the poloidal coherence length is only a few cm(Langmuir probe), it would be surprising if waves at the top and bottom of the torus were coherent.

This situation might be different for the low frequency coherent mode.

Model	$\overline{\chi^2}$	v_ϕ [km/sec]	$\overline{\Lambda}$ [cm]	Extra parameter	n_e^{tot} $[10^{17}m^{-3}]$	Power index
1 wave	0.7	3.6 ± 0.5	1.7 ± 0.4	—	4.3	-1.7
2 wave	0.5	5.1 ± 1.0	2.5 ± 0.7	$1.7 \pm 0.6(a)$	5.1	-3.4
Damping	0.4	—	1.4 ± 0.2	$1.2 \pm 0.4(D)$	2.6	+0.2
ΔK	0.7	—	2.0 ± 0.8	$0.6 \pm 0.5(\Delta K)$	5.9	-0.6

Table 6.2: *Comparison between models for asymmetric profiles.*

Fitting with the damping wave model yields the best average χ^2. Nevertheless, the results do not seem to corroborate those from the single wave model and in particular the decay power index is positive instead of being negative. Also, the ν–K diagram exhibits a cluster of points around $K = 4.5$ cm^{-1} and the damping factors obtained are much larger than that inferred from the probe. Even though the damping model represents the best curve fit, the results from the single wave model are in better agreement with the probe results.

6.7 Low frequency coherent mode

The frequency spectrum of the FFS signal in figure 6.2 exhibits coherent fluctuations which are also observed by other diagnostics such as the m=2 coil and the poloidal coils. Their amplitude is usually larger at the end of the discharge indicating a lower $q(a)$. These signals are said to be created by rotating magnetic islands with their associated density perturbation. A magnetic island is a filament of plasma with its own set of nested flux surfaces surrounding its own local magnetic axis. It is situated at one of the resonant surfaces which occur at rational values of the safety factor q.

A correlation analysis between the FFS signal and other fluctuating signals has been performed. Figure 6.14 shows in the top four graphs the FFS and the m=2 coils signal and their associated auto-correlation. The bottom graph displays their cross-correlation. A large level of cross-correlation indicates strong links between the two which are due to the m=2 island and higher frequency structure at a lower level of cross-correlation can also be seen. This is not an artifact of the analysis since cross-correlation with noise shows a much lower level. The same analysis between the FFS signal and the floating potential of the probe has shown similar correlation, contrary to previous observations(Côté,1984). The main difference was that the Langmuir probe was positioned in the scrape off layer of the plasma which isolates the probe from any gross features of the hotter plasma, whereas in this experiment it projected into the plasma. This is consistent with the results of Howling and Robinson(1988) which state that the limiter removes coherent fluctuations of the probe if the latter is situated 2 cm behind its leading edge.

Peaks of higher frequencies are also seen in the spectrum. They could be due to other magnetic island such as (m,n)=(3,2) ...which are weaker than the m=2. Another possible explanation is that the density distribution in the m=2 island is not perfectly sinusoidal which would lead to harmonics of the m=2 frequency.

Results from the fitting to the FFS intensity profile using the single wave model gave wavenumber in the range of $K \approx 1$–$2\ \mathrm{cm}^{-1}$ at the MHD frequency(40 kHz). Intensity fitting with the two wave model gave a large spread in $v(0.4 < v < 0.9)$ which is reminiscent of the results of section 4–4 with ultrasonic waves produced in air by two piezoelectric transducers. Furthermore, the phase difference between the top and bottom waves for an even m number should be around zero making a three humps intensity profile instead of the two seen in experiment. A possible explanation is that the jitter in the phase due to plasma column displacement might reduce the correlation between the two waves. Nevertheless, by using the result from the single wave model and assuming that the magnetic island propagates

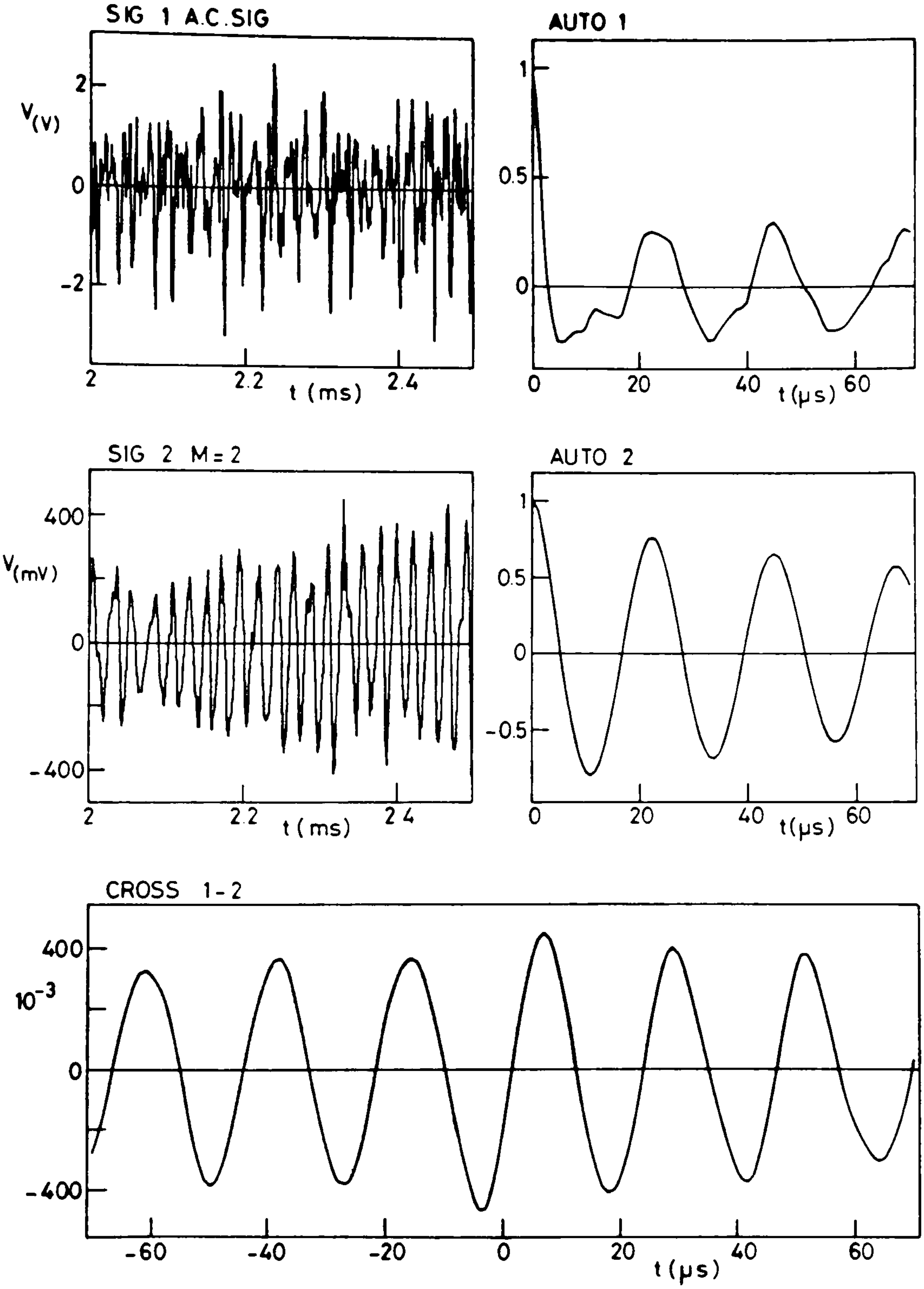

Figure 6.14: *Auto and cross correlation of FFS signal with m=2 coil signal.*

twice during one circular tour, the radius for which $q = 2$ is

$$b = \frac{2}{K} \simeq 1 - 2\text{cm}.$$

Now the radius b can be estimated from the definition of the safety factor q. Taking the experimental values of B_ϕ(0.5 T), I_p(10 kA), R (30 cm) and with the assumption that half of the plasma current is contained inside the resonant surface($r < b$), b is found to be around 3 cm. Thus, the radius of the resonant surface deduced from FFS is in broad agreement with the value expected to prevail in the tokamak.

6.8 Parametric dependency

The dependence of the fluctuation level on the main plasma parameters was investigated. With a one-man tokamak like TOSCA, it was difficult to carry out a systematic scan of the plasma parameters due to a lack of diagnostics ($T_e, n_e(r) \ldots$) and manpower. For these reasons, only the line average density was scaled with the fluctuation level. The range of density was restricted from 0.4 up to 1.3×10^{19} m^{-3} because of the uncertain interpretation in the asymmetric scattering profiles at higher density. The plasma current varied between 6–10 kA while the toroidal field stayed relatively constant around 0.5 T.

The relative fluctuation level($\tilde{n}_e/\overline{n}_e$) remains constant and around 6% over a wide range of mean density as shown in Figure 6.15(a). The proportionality measured between $\tilde{n}_e$ and $\overline{n}_e$ is common to most tokamaks (Equipe TFR, 1983; Weisen *et al.*, 1988; Van Andel *et al.*,1987) including the edge of TOSCA(Howling,1985). The small spread of data can be caused by changes in the density profiles which are not monitored and also by variation of the interaction length or the coherence. The average phase velocity($\overline{v}_{p,x}$) inferred from the intensity fitting along the direction of the array and the average amplitude–weighted wavevector($< K_\theta >$) stayed relatively constant around 4.1 $\pm$ 0.5 km/sec and 2.0-2.5 cm^{-1} respectively for the given range of density and both are shown in Figure 6.15.

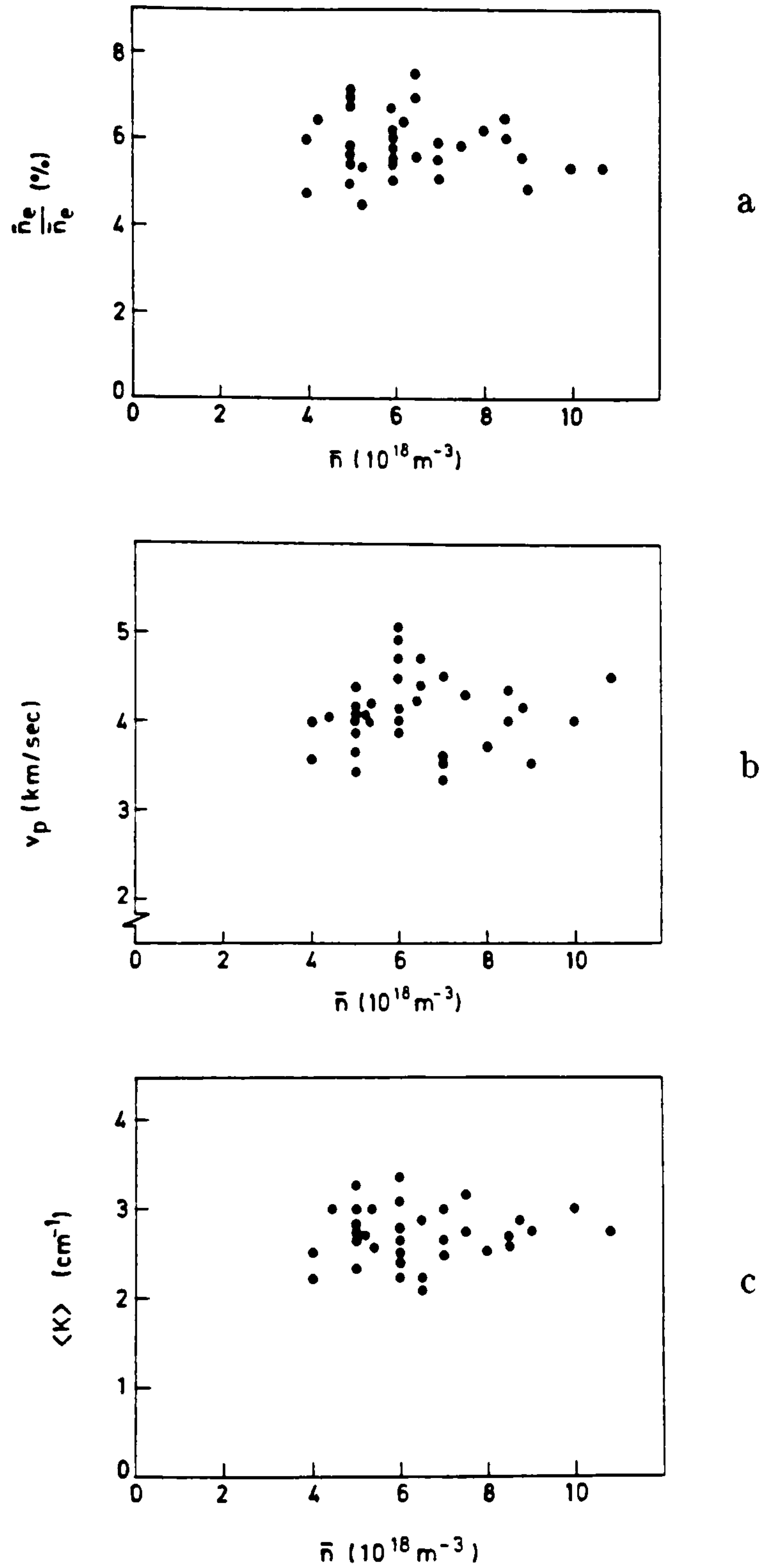

Figure 6.15: *Relative density fluctuation(a), average phase velocity(b) and mean power weighted wavenumber(c) as functions of the mean density.*

6.9 Discussion

Symmetric and asymmetric scattering profiles have been produced by plasma fluctuations and in the following we will concentrate the discussion on the former case. The wavelength structure of the turbulence has been deduced from these intensity profiles in terms of a model that assumes only a single wave. Fitting of the phase profile was problematic for hardware reasons and will accordingly be considered in qualitative terms only. Results from other models(2 wave, ΔK, Damping) corroborated those from the single wave model without adding more information. In particular, the ΔK model did not yield the expected result of $\Delta K/K \simeq 1$ as detected with collective Thomson scattering (Brower *et al.*, 1987,; Van Andel *et al.*, 1988; Mazzucato, 1982) and Langmuir probes(Levinson *et al.*, 1984; Hollenstein *et al.*, 1987) on other tokamaks. A possible reason for this may lies in the mistaken assumption that turbulence has a specific phase spectrum as assumed in the ΔK model, or in the insensivity of the profiles to the spectrum width(see section 4–7). Nevertheless, the interpretation placed upon the results from the analysis with a single wave model is that the wavelength inferred corresponds to the dominant fluctuation component for $0.2 < v < 1.3$.

Although in principle possible with FFS, the TOSCA configuration precluded accurate localisation of the plasma disturbance inside the vessel. For this discussion, the micro-instabilities are assumed to lie around $r/a \simeq 0.5$ which corresponds to the confinement or gradient region where the turbulence is supposed to be strongest. In comparison, Surko and Slusher(1980) measured on ALCATOR a relative fluctuation level of 5% at $r/a \simeq 0.5$ which is similar to the level on TOSCA(6%). We assume that the TOSCA density profile is well represented by $n_e = n_{eo}(1 - r^2/a^2)$ and its electron temperature profile by $T_e = T_{eo} \exp -(r/0.5a)^2$ with $T_{eo} \simeq 250$ eV. The rest of the parameters of TOSCA are listed in Table 5–1.

The plasma fluctuations were found to be approximately transverse to the toroidal direction which for a central chord corresponds to poloidal waves. For the array pointing vertically, the fluctuation propagates with an angle of 30° from its axis. If this angle remains in all experiments, the wavenumber (K_x) and the phase velocity($v_{p,x}$) measured are only components of the true poloidal value as discussed in Appendix B and are given by

$$v_{p,\theta} = \frac{v_{p,x}}{\cos 30^\circ} \qquad \text{and} \qquad K_\theta = K_x \cos 30^\circ.$$

These systematic changes are smaller than the uncertainties but have to be included in a complete interpretation(figures 6.12).

Dispersion relations deduced from the Langmuir probe data and from FFS signal are very similar in their phase velocity($v_\theta \simeq 4$ km/sec) and mean wavenumber ($< K_\theta > \simeq 2\text{cm}^{-1}$). This wavenumber correspond to $K_\theta\rho_s = 0.2$ for the edge plasma and $K_\theta\rho_s = 0.5$ for a = 4cm ($T_e \simeq 100$ eV). The difference in $K_\theta\rho_s$ can be due to the presence of various drift waves produced by changes in the collisionality between the edge(larger) and the centre. Also, the mean wavenumber is in agreement with the magnetic field scaling of Surko(1987).

Strong drift wave turbulence theory predicts a spectrum with $K_\theta\rho_s \simeq 0.1$–0.3 (Waltz,1983; Terry and Diamond,1985) in which energy cascades from higher K where the instability is strongest($K_\theta\rho_s \sim 1$) to smaller K. Even though the experimental results agree with these predictions, we can not say if the spectrum is due to inverse cascading or simply caused by instability peaking at these K. Bicoherence analysis which can detect three wave coupling and might have resolved this question, gave values around the noise level. This does not mean that non-linear coupling is non existent in these observations since the presence of many interacting modes could produce similar bispectra.

The average phase velocity measured with the FFS experiment is around 4.1 $\pm$ 0.4 km/sec which becomes 4.6 $\pm$ 0.5 km/sec by including the twisting angle of the 2–D map. Even though the disturbance seems to propagate in one direction, we have been unable to determine its poloidal direction(electron or ion drift). The phase velocity is slightly larger than the electron diamagnetic velocity calculated by using equation 5.4 and the results are displayed in figure 6.16. Such a disagreement has also been detected on TCA(Weisen, 1986) and TEXT(Ritz *et al.*, 1987) where phase velocity up to 3 times v_{de} have been measured. In the confinement region of TOSCA ($2\ cm\ < r < 7\ cm$) where $v_{de} \simeq 3$ km/sec, the ratio $v_{p,\theta}/v_{de}$ is 1.5 which might be explained by uncertainties in the density gradient scale length(L_{ne}) and (T_e).

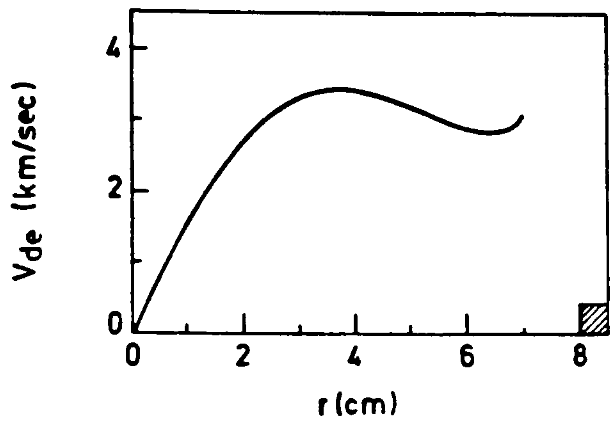

Figure 6.16: *Drift velocity calculated from TOSCA density and temperature profiles.*

Two physical explanations have also been put forward to account for this discrepancy. The first one concerns non-isothermal fluctuations which combine with the density fluctuations to flatten the pressure profile(n_e and T_e) and produce drift waves, due to trapped particles, having velocity

$$v_{pe} = \frac{kT_e}{qB}\frac{\nabla P_e}{n_e}.$$

On TOSCA the drift velocity is around 6–7 km/sec($r=$ 4 cm). The second explanation is simply that a doppler shift due to poloidal rotation is superimposed on the diamagnetic drift. Rechester and Rosenbluth(1978) showed that the poloidal rotation is damped while the toroidal rotation is not since it behaves as a rigid body. The presence of a radial electric field due to the plasma loss of electrons can combine with the magnetic field to produce an $\mathbf{E} \times \mathbf{B}$ drift with velocity of the order of that measured. Coherent signals from the $m = 2$ tearing mode are believed to be the result of such rotation(Scott *et al.*,1985). Unfortunately, the rotation velocity on TOSCA has not been measured with spectroscopy using the doppler shift of an impurity line radiation. Similarly, measurements of electron cyclotron emission(ECE) made in other tokamaks(Tait *et al.*, 1981) have given only a low level of temperature fluctuation.

The phase velocity inferred with the Langmuir probe is smaller than that from the FFS. Interpreted as a difference between the edge and the confinement region, this has also been observed on TCA(Weisen *et al.*, 1988) and TEXT(Ritz *et al.*, 1987). Howling(1985) showed that the velocity in the edge of TOSCA was of the same order as and propagating in the direction of an electron diamagnetic drift wave($L_{ne} = 1\ cm, T_e = 14$ eV).

Most of the power of the fluctuation measured by FFS lay around ω_{*e}(100 kHz) and the power decay index(p) at higher frequency is around -2. This is similar to that measured with the Langmuir probe and slightly smaller than the published values of $p = 2$(Lachambre,1983); 2.5(Semet,1980); $1.5 \leq p \leq 3.5$(van Andel,1987). The fluctuation level obtained can be compared to the mixing length level of Kadomtsev(equation 5.7). At $r = 4$ cm, the density scale length is 6 cm and $< K_\theta > \simeq 2.1 \pm 0.5$ cm^{-1}, which means $\tilde{n}_e/\overline{n_e} \simeq 8$ %(5.5 % rms) in agreement with the measured level of 6 %. At the mixing length level fluctuations are considered to be strong turbulence. The independence of the relative fluctuation level on the mean density is also in agreement with Kadomtsev. This indicates that the other driving forces(∇T_e, $\nabla \eta$) are not as important as ∇n_e in the final saturation level.

Howling concluded in his work(1985) that the turbulence at the edge was due to a strong drift wave like that modelled by Terry(1985). Even though the results from FFS are insufficient for a conclusive identification, the frequency range, the poloidal propagation, the mixing length level of fluctuation and mean wavenumber around $0.5/\rho_s$ are all at least consistent with the fluctuation being caused by electron drift mode.

The transport produced by micro-instability gives a diffusion coefficient ($D_\perp$)

for quasi-linear turbulence of

$$D_\perp = 4 \times 10^{-15} \gamma L_{ne}^2 \left\{ \frac{\tilde{n}_e}{\bar{n}_e} \right\}^2$$

where γ is the linear growth rate of the fluctuations. For TOSCA at r= 4 cm, the growth rate of a drift trapped electron mode(DTEM) is around $\gamma \simeq 0.2\omega_{*e} \simeq$ 130 kHz which leads to $D_\perp \simeq 2m^2/sec$. This diffusion coefficient is similar to that inferred with the Langmuir probe(2 m^2/sec) and also with the heat pulse propagation of sawteeth(Howling,1985). At this radius, the particle confinement time given by $\tau = r^2/(5.8D_\perp)$ is $\simeq$ 0.2 msec which is consistent with the lifetime obtained from other diagnostics. However, the edge probe measurement suggests that this expression is not valid, the Boltzmann relation does not hold, the phase angle is not $\pi/2$ and a substantial fraction of the power is not correlated.

Also the heat loss(Q_t) induced by turbulence can be calculated using equation 5.14 and assuming Boltzmann relation by

$$Q_t = \frac{nT_e^2}{B_t} \frac{\tilde{n}_e}{n_e} \frac{\tilde{P}_e}{P_e} \gamma_{\tilde{E}\tilde{P}} \sin(\theta_{\tilde{E}\tilde{P}})$$

where $\gamma_{\tilde{E}\tilde{P}} = < \tilde{E}\tilde{P} > / \sqrt{\tilde{E}^2 \tilde{P}^2}$ is a measure of the coherence, $\tilde{P}$ and $\tilde{E}$ are the pressure and electric field. By assuming no electronic temperature fluctuations($\tilde{T}_e = 0$) and perfect coherence($\gamma_{\tilde{E}\tilde{P}}$=1) and $\theta_{\tilde{E}\tilde{P}} = \pi/2$; we find Q_t = 60 kW/m^2. Integrating Q_t over all the torus surface at r/a =0.5 yields an upper limit to turbulence induced power loss of 30 kW which is the order of the ohmic power(25 kW). Considering that the Langmuir probe gave values of $\gamma_{\tilde{E}\tilde{P}} \simeq 0.2 - 0.5$(Howling *et al.*, 1985) and that 30% of the ohmic power is radiated, the contribution of this heat flux can go some way to explaining the measured transport.

Results from TOSCA(Ellis,1984) displayed the old ALCATOR scaling($\tau_E \propto \bar{n}_e$) which implies that Q_t is independent of $\bar{n}_e$. Since FFS measurement gives $\tilde{n}_e/\bar{n}_e$ = constant, it is not possible to account for the scaling unless changes in coherence and phase angle are involved. Direct measurement of these parameters are beyond the capacity of a FFS experiment, but new advances in diagnostics such as the heavy ion beam probe(Hallock, 1987) can yield the desired information and perhaps resolve the mystery of transport in the core of the machine.

Asymmetric profiles with $r_2 \leq 0.8$ and $|u_o| > 0.1$ occur quite regularly(40 %). Though the asymmetry could be the result of misalignment between the axis of the cylindrical lens and the array, we found that asymmetry is associated with high density. A possible explanation may be found in the fact that the optical path of the FFS shares a port with the neutral gas line reservoir. The influx of neutral gas can damp drift waves locally(Cap,1976) or produce new instabilities due to changes in the resistivity gradient ($\nabla\eta$ modes, Garcia *et al.*,1985) both of which will induce asymmetry. Absence of the plasma with the same influx of neutrals does not produce any signals because high pass filtering(30 kHz) eliminates all of the sonic frequency range. These are only speculative comments and suggest further study of the effect of gas puffing on the turbulence.

Chapter 7

Summary and conclusions

The basic purpose of this thesis has been to develop, test and implement on the TOSCA tokamak a far forward scattering(FFS) diagnostic using an array of detectors. The principle of the technique lies in the analysis of the oscillations induced on the profile of a Gaussian laser beam by transmission as it travels transversely to a disturbance. Intensity and phase profiles at the detector plane are then fitted to theoretical curves to yield various parameters of the density fluctuation(wavelength, amplitude, position...). Different models of fluctuations have been put forward to calculate these profiles and they were reviewed thoroughly in Chapter 2 of this thesis.

Various tests were performed to assess the predictions of FFS theory. From the scattered signal resulting from the interaction of an ultra-sonic wave and a laser beam, we were able to infer the wavenumber, position, amplitude and direction of propagation of the disturbance in accord with experimental values. The direction was determined using cross correlation analysis and did not require any separate frequency shifted local oscillator. Interaction with wide-band noise did not alter the measurement of the wavenumber and the phase velocity inferred from the ν–K diagram was consistent with the sound velocity. The amplitude spectra of the wave measured with the FFS system and a high frequency microphone agreed well with each other. Results from scattering by two ultra sonic waves were not as conclusive owing to the high sensitivity of the results to the phase difference between the two waves.Nevertheless, under these controlled conditions the phase fitting yielded the correct wavenumber.

To get an experimental test set up more closely resembling turbulent plasma conditions, an air jet was employed. The range of K measured was in the so called production region in which the size of the nozzle determines their value. For the scattering by an air jet flowing perpendicularly to the optical beam and parallel to the array axis, the phase velocity obtained from the ν–K diagram was similar to the expected bulk velocity of the jet. The power spectrum of the scattered signal from the jet directed perpendicular to the array indicated a spread in the velocity consistent with the theory.

Studies were made to assess the effect of wrong estimation of the beam waist at the detector plane(W_i) and the position of the disturbance(ζ) from the object waist. Changes in ζ will alter the phase velocity inferred from the phase and intensity fitting in different ways. This can be used to determine more precisely the position of the wave by fine tuning ζ to bring both phase velocities to the same value. The waist W_i affects the fitting through the dimensionless parameter u and a wrong measurement will yield saturation in the estimation of the fitted K for low values. This saturation can also occur when the disturbance has a large spectrum width. Determination of the saturation is impeded by the unknown instrumental function of the FFS system.

A model has been developed to calculate the effect on the scattering signal of fluctuations having a broad K-spectrum. Broadening of profiles is predicted but results from an artificially created spectrum did not yield the expected ΔK. This discrepancy may be caused by the underlying assumption of a specific phase spectrum which is not representative of the experimental condition.

A different approach in the analysis of the signal was attempted by reconstruction in real time of the density fluctuation from the scattered intensity(I_{ac}). The code written for this purpose gave the right result for theoretical signals but was found to be very sensitive to changes in the input signal(I_{ac}). Nevertheless, density fluctuations produced by ultrasonic waves were reconstructed successfully for positions around the axis($|u_o| < 2$). The complication and sensitivity to noise of this approach suggest that an optical reconstruction scheme(*e.g.* Weisen, 1985) is to be preferred to this numerical one.

The results from scattering by the plasma were similar to those from other machines. Statistically the signal resembles noise with its Gaussian voltage distribution, high dimensionality and low bicoherence. Analysis of the scattering signal with various FFS theory gave the closest agreement with the Langmuir probe data when the single wave model was used.

Fluctuations were found to propagate predominantly in the poloidal direction, but no information about their sense of direction(electron or ion drift) is obtainable with the single wave model. After correcting for the angle of propagation, the power weighted wavenumber and the average phase velocity were around 2 cm^{-1} and 4.5 km/sec respectively. The power spectrum of the fluctuation peaks around 50-100 kHz and decays as ν^{-2} towards higher frequency. The total relative fluctuation is around 6% and is consistent with the mixing length level of Kadomtsev.

The relative density fluctuation level, power weighted wavenumber and average phase velocity did not seem to vary with mean plasma density. Low frequency coherent modes associated with an m=2 tearing island were detected principally towards the end of the discharge. Wavelengths inferred from FFS at these frequencies were consistent with the expected radius for the magnetic island.

The frequency range, the phase velocity, the poloidal propagation and mean wavenumber, around $\sim 0.5/\rho_s$, are all at least consistent with the identification of the observed plasma fluctuations as the electron drift wave. The enhanced transport due to the turbulence is of the right order to account completely for the observed transport.

This thesis has assessed the limits of validity and practical applicability of a FFS system, but more work needs to be done for a complete understanding. On the theoretical side, the ΔK model should be extended to cater for random phase spectra. This might be done by using a renormalisation procedure common in fluid dynamics. Also, a better estimate of the instrumental function($\Im(K)$) should be found to evaluate the effect of broadband spectra.

An improved version of the scattering set up could easily be implemented on other machines by increasing ζ to 0.8 and synchronising the ADC to get a better phase profile. Also, a piezoelectric transducer should be introduced in the set up for checking the scattering system and insuring that all optical parts are correctly aligned. With these small modifications, the effect of gas puffing or plasma position on the asymmetric profile could be better investigated.

For studies of transport in the core of the plasma machine, a heavy ion beam probe(Hickok *et al.*,1985) would be a more relevant diagnostic since it can measure simultaneously the electric field and density fluctuation with their coherence. A laser scattering system could still be useful to corroborate results from the HIBP diagnostic. Also, measurement of magnetic field fluctuations in the hot core with a scattering scheme proposed by Lehner *et al.*(1986) might be able resolve the issue of the electrostatic or magnetic origin of the anomalous transport.

A critical appraisal of the far forward scattering technique is necessary to indicate its possible range of application. Among the weaknesses, the dependence of the analysis on the coherence of the signal is the most restrictive. All the theoretical models consider only waves with a $\sin(\Omega t)$ term which is not exactly the case for plasma turbulence. The choice of a simple model for the analysis limits the interpretation, but it would be pointless to obtain one expression of the scattered intensity($I_{ac,e}$) which contains all the special effects with tens of parameters when only few detectors are available. Even though the scattered signal depends on the axial position(ζ) of the disturbance, it represents a line integrated value of the fluctuations and renders their localisation difficult. The effect of spectral width has not been satisfactorily accounted for and cannot be inferred from the experimental signal.

Among the advantages of a FFS system, the optical assembly is rather simple and is insensitive to vibrations since the scattered and local oscillator beam propagate through the same path. A FFS system would be an ideal monitor of fluctuations for a large plasma machine where access is limited. Also, it is well suited to study quasi-coherent waves in a plasma produced by externally launched RF waves during auxiliary heating.Finally, the FFS technique could be used outside the realm of plasma physics to unveil small scale turbulence occurring in the atmosphere or in wind tunnels.

Appendix A

Gaussian optics

The basic building block of our analysis turns out to be spherical waves having a gaussian variation in amplitude across the wavefront. Their amplitude distribution at any plane can be written in the form(Siegman, 1971)

$$U(x,y,z) = \sqrt{P_o}\,\underbrace{\frac{1}{\sqrt{\pi}w(z)}}_{normalising}\,\underbrace{\exp\left(-j\frac{k}{2}\frac{x^2+y^2}{R}\right)}_{spherical\ wave}\,\underbrace{\exp\left(-\frac{x^2+y^2}{2w^2}\right)}_{gaussian} \tag{A.1}$$

where P_o is the total beam power, w is the spot size of the gaussian beam defined as e^{-1} in intensity and R is the radius of curvature of the spherical wave. Kogelnik and Li(1966) showed that the last expression satisfies the scalar wave equation.

If we define a complex radius of curvature q by

$$\frac{1}{q} = \frac{1}{R} - \frac{j}{kw^2} \tag{A.2}$$

which contains both the radius of curvature and the spot size of the gaussian spherical wave, equation A.1 can be rewritten in the compressed form

$$U(x,y) = \frac{P_o}{\sqrt{\pi}w(z)}\exp\left\{-j\frac{k}{2}\frac{x^2+y^2}{q(z)}\right\} \tag{A.3}$$

To calculate the propagation properties of gaussian beam, we can apply the diffraction integral(eqn. 2.2) to a gaussian plane wave of spot size W_o at an input plane $Z = 0(q_o = -j/kW_o^2)$.

After defining the Rayleigh range as $z_r = kW_o^2$, the amplitude distribution at any later plane z is

$$U(x,y,z) = \frac{1}{\sqrt{\pi}w(z)}\exp\{-j[kz - \psi(z)]\}\exp\left\{-j\frac{k}{2}\frac{x^2+y^2}{q(z)}\right\} \quad \text{(A.4)}$$

with the following identifications:

$$\begin{aligned} q(z) &= z + jz_r & \psi(z) &= \arctan\frac{z}{z_r} \\ w(z) &= W_o\sqrt{1+\left(\frac{z}{z_r}\right)^2} \end{aligned}$$

This shows that a beam starting as a gaussian plane wave will remain in the form of a gaussian spherical wave.

The input plane where the beam wavefront is planar is referred as the waist with a beam width of W_o. The Rayleigh range correspond to the distance from the waist to the point where the beam has doubled area. At large distance from the waist($z \gg z_r$), the beam diverges linearly with an half angle of $\theta \approx w(z)/z = W_o/z_r$.

The previous calculation could have been carried out from any input plane. In general, the basic law of propagation for the complex curvature $q(z)$ between two planes is given by

$$q(z_2) = q(z_1) + L \quad \text{(A.5)}$$

where $L = z_2 - z_1$. The effect of a thin lens with focal length f is to change the radius of curvature without affecting its spot size. This leads to the lens law for gaussian beam

$$\frac{1}{q_+} = \frac{1}{q_-} - \frac{1}{f} \quad \text{(A.6)}$$

where q_+ and q_- are the complex radius of curvature just after and before the lens. The last two equation are generalisation of similar laws for spherical waves. Complicated arrangements of lenses can be analysed by calculating successively the complex radius of curvature from plane to plane. In the simple but important case of a single lens, the waist(W_2) in front of the lens is related to the back one(W_1)

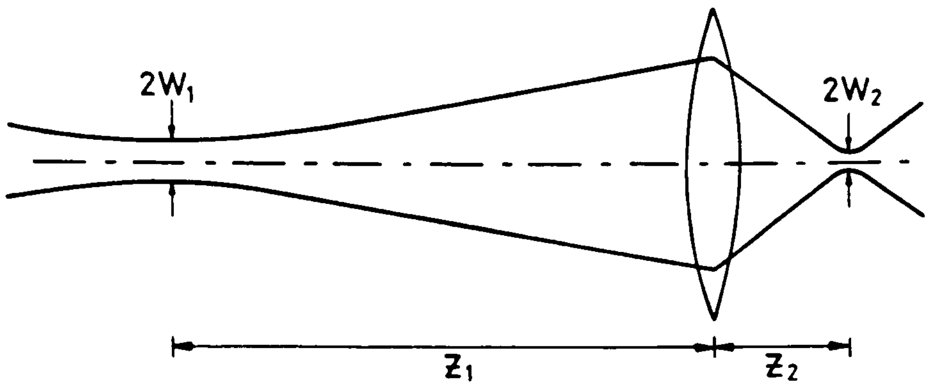

Figure A.1: *Geometry for calculation of lens effect on the complex radius of curvature.*

by

$$W_2 = W_1 \frac{f}{\sqrt{(f-z_1)^2 + z_{r,1}^2}}$$

and is situated at a distance

$$z_2 = \left(\frac{W_2}{W_1}\right)^2 (z_1 - f) + f$$

from the lens. For the special case of the waist being at the focal plane, the last two relations simplify to

$$kW_1W_2 = f \qquad \text{and} \qquad z_2 = z_1 = f. \tag{A.7}$$

Appendix B

Effect of cylindrical lens on FFS

The effect of misalignement of the fluctuation wavevector direction and the axis of the cylindrical lens is investigated in this appendix. Figure B–1 illustrates the arrangement at the detector plane in which the wavevector K is parallel to u_x and

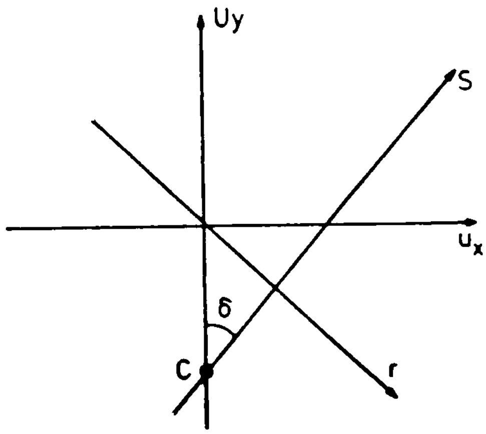

Figure B.1: *Frame of perturbation(u_x, u_y) and of cylindrical lens(r, s).*

at an angle of δ with the axis of the cylindrical lens. The effect of the latter is to perform the line integral

$$I(r,t) = \int_c I_{ac}(u_x, u_y, t) W_i \mathrm{d}s \tag{B.1}$$

where $ds = \sqrt{du_x^2 + du_y^2}$. The path of integration is defined as $u_y = mu + c$ where the slope $m = -\cot(\delta)$ and the abscissa at the origin is $c = r/sin(\delta)$. By including I_{ac} of equation 2.17 into B.1 and performing the integral, we obtain

$$I_{ac}(u_x) = \overbrace{\frac{P_o}{\sqrt{\pi} W_i} \frac{\Delta\phi}{2} e^{-r^2} e^{-(\zeta \frac{v}{2} \sin(\delta))^2} e^{-\frac{v^2(1+\cos(\delta)^2)}{4}}}^{C} \cdot$$

$$\left\{ \sin(\Omega t) \underbrace{\{e^p \cos(\theta_-) - e^{-p} \cos(\theta_+)\}}_{\alpha} + \cos(\Omega t) \underbrace{\{e^{-p} \sin(\theta_+) - e^p \sin(\theta_-)\}}_{\beta} \right\} \quad \text{(B.2)}$$

where

$$\begin{aligned} \theta_\pm &= \zeta_1 v \cos(\delta)(r \pm \frac{v}{2} \cos(\delta)) \\ p &= uv \cos(\delta). \end{aligned}$$

The intensity and phase profile can be determined as usual by calculating formula 2.24.

Apart from a $v \sin(\delta)$ term in the amplitude factor, this expression of I_{ac} has the same form as equation 2.17 if we substitute $v \cos(\delta)$ for v. This is to say that the result of a fitting will give the component of the wavevector along the axis of the cylindrical lens. Therefore, to interpret the result accurately a knowledge of the angle δ is necessary.

References

Allen C.W. (1973) 'Astrophysical quantities.' Athlone Press.

Barkley H.J. *et al.*(1988) *Plasma Physics* **30**, 217.

Beall J.M., Kim Y.C. and Powers E.J.(1982) *J. Appl. Phys.* **53**, 3933.

Bendat J.S. and Piersol A.G. (1971) 'Random data: Analysis and measurement procedures.' John Wiley and sons.

Bendat J.S. and Piersol A.G. (1980) 'Engineering applications of correlation and spectral analysis.' John Wiley and sons.

Bevington P.R. (1969) 'Data Reduction and error analysis for the physical sciences.' McGraw-Hill.

Born M. and Wolf E. (1980) 'Principles of Optics.' Pergamon Press, 6th. edition .

Bracewell R. (1986) 'The Fourier transform and its application.' McGraw-Hill.

Braginskii S.I and Shafranov V.D.(1959) 'Plasma Physics and the problems of Controlled Fusion.' Pergamon press, New York **2**, 39.

Brodeur P., Ratel G. and van Handel H.W.H. (1988) *Plasma Phys.* **30**, 805.

Brower D.L *et al.*(1985) *Phys. Rev. Lett.* **54**, 689.

Brower D.L, Peebles W.A. and Luhmann N.C. (1987) *Nuclear Fusion* **27**, 2055.

Cap F.F. (1976) 'Handbook on Plasmas Instabilities.' Vol. **1**, Academic Press.

Clemmow P.C. and Dougherty J.P (1969) 'Electrodynamics of particles and plasmas.' Addison–Wesley.

Cooley J.W. and Tukey J.W. (1967) *Mathematical Computational* **19**, 297.

Côté A. (1984) M.Sc. thesis, Univ. of Oxford.

Côté A., Haynes P., Howling A., Morris A.W. and Robinson D.C. (1985) *12 th European Conf. on Controlled Fusion and Plasma Physics*, Part 2, 450.

Côté A., Doyle E.J.,Evans D.E. and Sonoda Y. (1985) *Proc. of 2nd Int. Symp. on Laser-aided Diagnostics*, 85.

Côté A. and Evans D.E. (1986) 'Turbulence and Anomalous Transport.' Cargèse workshop , Ed. Grésillon D. and Dubois. M.A., 111.

Cummins H.Z. and Swinney H.L. (1970) 'Progress in Optics.' Vol. 8, Ed. E. Wolf, 133.

Davies J.T. (1972) 'Turbulence phenomena.' Academic Press, N.Y. .

Doyle E.J. (1982) M. Eng. Sc. Thesis, National University of Ireland.

Doyle E.J., Evans D.E. and von Hellermann M. (1984,a) *Proc. 3rd International Conference on Infrared Physics* , 635.

Doyle E.J. and Evans D.E. (1984,b) *Proc. 3rd International Conference on Infrared Physics* , 638.

Doyle E.J., Evans D.E. and von Hellermann M. (1984,c) *Proc. 3rd International Conference on Infrared Physics* , 641.

Ellis J.J *et al.*(1984) *Proc. of 10th Int. Conf. on Plasma Phys. and Cont. Nuclear Fus. Res.* IAEA London , Vol. **1**, 363.

Equipe TFR (1978) *Nuclear Fusion*, **18**, 647.

Equipe TFR (1983) *Plasma Physics*, **25**, 641.

Evans D.E. and Katzenstein J. (1969) *Rep. Prog. Phys.* **32**, Part 1, 207.

Evans D.E. (1974) in 'Plasma Physics.' B.E. Keen editor, The Institute of Physics, London, 145.

Evans D.E., von Hellermann M. and Holzhauer E. (1982) *Plasma Physics* **24**, 819.

Evans D.E. and Doyle E.J. (1983) *Proc. Kyushu Int. Symp. Laser-aided Diagnostics*, 71.

Evans D.E., Doyle E.J., Frigione D., von Hellermann M. and Murdoch A. (1983) *Plasma Physics* **25**, 617.

Furth H.P. (1975) *Nuclear fusion*, **15**, 487.

Garcia L. *et al.*(1985) *Phys. of Fluids* **28**, 2147.

Gaskill J.D. (1978) 'Linear Systems, Fourier Transforms and Optics.' J. Wiley.

Goldston R.J. (1984) *Plasma Phys. and Contr. Fus.* Vol. **26**, 87.

Golub G.H. and Van Loan C.F (1982) 'Matrix computation.' North Oxford Academic.

Goodman J.W. (1968) 'Introduction to Fourier Optics.' McGraw-Hill.

Goodman J.W. (1970) 'Progress in Optics.' Vol.8 Editor E. Wolf, 1.

Grassberger P. and Procaccia I. (1983) *Physica* **9D**, 189.

Guzdar P.N., Chen L., Tang W.M. and Rutherford P.H. (1983) *Phys. Fluids* **26**, 673.

Hasegawa A. and Mima K.(1978) *Phys.Fluids* **21**, 87.

Hasegawa A. and Wakatani M. (1983) *Phys. Rev. Lett.* **50**, 682.

Hallock G.A., Wooton A.J. and Hickok R.L. (1987) *Phys. Rev. Lett.* **59**, 1301.

Hickok R.L. *et al.*(1985) *Proc. of 2nd Int. Symp. on Laser-aided Diagnostics*, 145.

Hinze J.O. (1975) 'Turbulence.' McGraw-Hill, N.Y. .

Hollenstein Ch., Martin Y. and Simm W. (1987) *J. Nucl. Mat.* **145-147**, 260.

Holzhauer E. and Massig J.H. (1978) *Plasma Physics* **20**, 867.

Howling A. (1985) D.Phil. thesis, Univ. of Oxford.

Howling A., Côté A., Doyle E.J., Evans D.E. and Robinson D.C. (1985) *12 th European Conf. on Controlled Fusion and Plasma Physics*, Part 2, 311.

Howling A. and Robinson D.C. (1988) *Plasma Physics* **30**, 1863.

Hutchinson I.H. (1987) 'Principles of plasma diagnostics.' Cambrige University Press.

IEEE Digital Signal Processing Committee (1979) 'Programs for digital signal processing.', IEEE press, New York.

Jackson J.D. (1975) 'Classical Electrodynamics.' J. Wiley, 2nd. edition,.

Jacobson A.R., Rusbridge M.G. and Burkhardt L.C. (1984) *J. Appl. Phys.* **55**, 125.

James B.W. and Yu C.X. (1985) *Plasma Physics* **27**, 557.

Kadomtsev B.B. (1965) 'Plasma turbulence.' Academic Press.

Kadomtsev B.B. and Pogutse O.P. (1971) *Nuclear Fusion* **11**, 67.

Kim Y.C. and Powers E.J.(1979) *IEEE Trans. on Plasma Sci.* **PS-7**, 120.

King R.E.,Wooton A.J. and Robinson D.C. (1974) *8th SOFT conference*, 57.

Klein W.R. and Cook B.D. (1967) *IEEE Trans. on Sonics and Ultrasonics* **SU-14**, 123.

Kogelnik H. and Li T. (1966) *Applied optics*, **5**, 1550.

Korpel A. (1972) 'Applied Solid State Science.' R. Wolfe ed., Academic Press, Vol. **3**, 71.

Korpel A. (1981) *Proc. IEEE* **69**, 48.

Lachambre J.L., Decoste R., Robert A. and Noël P. (1983) *J. Appl. Phys.* **54**, 4722.

Lawson J.D. (1957) *Proc. Phys. Soc. B* **70**, 6.

Lehner T. (1986) 'Turbulence and Anomalous Transport.' Cargèse workshop , Ed. Grésillon D. and Dubois. M.A., 323.

Levinson S.J., Beall J.M., Powers E.J. and Bengtson R.D. (1984) *Nuclear Fusion* **24**, 527.

Liewer P.C. (1985) *Nuclear Fusion* **25**, 543.

Lukosz W. (1967) *Journal of the optical society of America* **57**, 932.

Luhmann Jr. N.C. (1979) *Infrared and Millimeter Waves* **Vol. 2** K.A. Button editor, Academic Press, Chapter 1 ,1.

Luhmann Jr. N.C. and Peebles W.A. (1984) *Rev. Sci. Instruments* **55**, 279.

Magyar G. (1981) in 'Plasma Physics and Nuclear Fusion Research.' R.D. Gill editor, Academic Press, 535.

Mazzucato E. (1976) *Phys. Rev. Lett.*, **36**, 792.

Mazzucato E. (1978) *Physics of fluids*, **21**, 1063.

Mazzucato E. (1982) *Phys. Rev. Lett.*, **48**, 1828.

McGuire K.M.(1979) D.Phil. thesis, Univ. of Oxford.

Morris A.W. (1985) D.Phil. thesis, Univ. of Oxford.

Olivain J. (1979) *Report No. EUR-CEA-FC-1024* Fontenay-aux-Roses, France.

Papoulis A. (1968) 'Systems and Transforms with Applications in Optics.' McGraw-Hill.

Peratt A.L., Watterson R.L. and Derfler H. (1977) *Phys. Fluids* **20**, 1900.

Philipona R. (1987) *Rev. Sci. Instrum.* **58**, 1572.

Rechester A.B. and Rosenbluth M.N. (1978) *Phys. Rev. Lett.* **40**, 38.

Ritz Ch.P., Bengtson R.D., Levinson S.J. and Powers E.J. (1985) *Phis. Fluids* **56**, 1055.

Ritz Ch.P. *et al.*(1987) *Nuclear Fusion* **27**, 1125.

Ritz Ch.P., Powers E.J. and Bengtson R.D. (1988) *report FRCR-311* , Texas University, Fusion Research Center.

Robinson D.C. and Rusbridge M.G. (1969) *Plasma Physics* **11**, 73.

Romanelli F., Tang W.M. and White R.B. (1986) *Nuclear Fusion* **26**, 1515.

Rosenbluth M.N. and Rostoker N. (1962) *Phys. Fluids* **5**, 776.

Rusbridge M.G. (1986) 'Turbulence and Anomalous Transport.' Cargèse workshop , Ed. Grésillon D. and Dubois. M.A., 223.

Sagdeev R.Z. and Galeev A.A (1969) 'Nonlinear plasma theory.', Benjamin, New York.

Salpeter E.E. (1960) *Phys. Rev.* **120**, 1528.

Scott B.D., Hassam A.B. and Drake J.F. (1985) *Phys. Fluids* **28**, 275.

Semet A., Mase A., Peebles W.A., Luhmann Jr. N.C. and Zweben S. (1980) *Phys. Rev. Lett.* **45**, 445.

Shafranov V.D. (1971) *Plasma Physics* **13**, 757.

Sharp L.E. (1983) *Plasma physics* **25**, 781.

Sheffield J. (1975) 'Plasma Scattering of Electromagnetic Radiation.' Academic Press.

Siegman A.E. (1971) 'An introduction to Lasers and Masers.' McGraw-Hill.

Slusher R.E. and Surko C.M. (1980) *Phys. Fluids* **23**, 472.

Smith D.E., Powers E.J. and Caldwell G.S. (1974) *IEEE Trans. on Plasma Science* **PS-2**, 261.

Sonoda Y. *et al.*(1984) *Jpn. J. Appl. Phys.* **23**, 1412.

Sonoda Y., Suetsugu Y., Muraoka K. and Akazaki M. (1983) *Plasma Phys.* **25**, 1132.

Spitzer L.,Jr. (1962) 'Physics of fully ionized gases.' Wiley-Interscience, New York.

Stangeby P. (1984) *Phys. Fluids* **27**, 682.

Stern C. and Grésillon D. (1983) *Journal de physique* **44**, 1325.

Strachan J.D. *et al.*(1982) *Nuclear fusion* **22**, 1145.

Surko C.M. and Slusher R.E. (1976) *Phys. Rev. Lett.*, **37**, 1747.

Surko C.M. and Slusher R.E. (1980) *Phys. Fluids.*, **23**, 2425.

Surko C.M. and Slusher R.E. (1983) *Science* **221**, 817.

Surko C.M. (1987) *Comments on Plasma Phys. Contr. Fusion* **10**, 265.

Swift J.D. and Schwar M.J.R. (1970) 'Electrical Probes for Plasma Diagnostics.' Iliffe books.

Tait G.D., Stauffer F.J. and Boyd D.A. (1981) *Phys. Fluids* **24**, 719.

Tang W.M. (1978) *Nuclear fusion*, **18**, 1089.

Tange T., Nishikawa K. and Sen A.K. (1982) *Phys. Fluids* **25**, 1592.

Terry P.W. and Diamond P.H. (1985) *Phys. Fluids* **28**, 1419.

Terry P.W. and Diamond P.H. (1984) in 'Statistical Physics and Chaos in Fusion Plasmas.' ed. Horton C.W. Jr. and Reichl L.E., Wiley, New York, 335.

Tsukishima T. (1979) in 'Diagnostics for Fusion Experiments.' E. Sindoni and C. Wharton editors, Pergamon Press, 255.

van Andel H.W.H., Boileau A. and von Hellermann M.(1987) *Plasma Phys.* **27**, 49.

von Hellermann M. and Holzhauer E.(1984)*IEEE Trans. on Plasma Sc.* **PS-12**,5.

von Hellermann (1985) , private communication.

Wakatani M. and Hasegawa A. (1984) *Phys. Fluids* **27**, 611.

Waltz R.E. (1983) *Phys. Fluids* **26**, 169.

Waltz R.E. and Dominguez R.R. (1983) *Phys. Fluids* **26**, 3338.

Waltz R.E. (1985) *Phys. Fluids* **28**, 577.

Watterson R.L., Peratt A.L. and Derfler H. (1979) *Phys. Fluids* **22**, 110.

Weisen H. (1985) *Infrared Phys.* **25**, 543.

Weisen H., Hollenstein Ch. and Behn R. (1988) *Plasma Physics* **30**, 293.

Wesson J.A. (1987) 'Tokamaks.' Clarendon press, Oxford.

Wootton A.J. *et al.*(1988) *Plasma Physics* **30**, 1479.

Yu C.X. *et al.*(1988) *Plasma Physics* **30**, 1821.

Zernike F. (1935) *Z. tech. Phys.* **16**, 454.

Zhukovskii V.G. and Rtishchev V.A. (1988) *Sov. J. Plasma Phys.* **14**, 276.